Bounds on Super-Directivity and Super-Gain

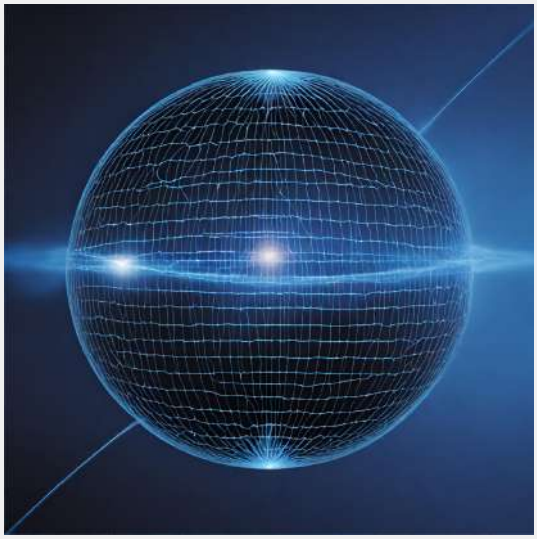

Laura Passalacqua

PhD in Information Engineering and Science

UNIVERSITÀ DEGLI STUDI DI SIENA

Dipartimento di Ingegneria dell'Informazione e Scienze Matematiche

UNIVERSITÀ
DI SIENA
1240

Bounds on Super-Directivity and Super-Gain

Laura Passalacqua

Ph.D Thesis in Information Engineering and Science

Supervisor
Prof. Stefano Maci
Prof. Enrica Martini
Dr. Cristina Yepes

Examination Commitee
Prof. Matteo Albani
Prof. Antonio Clemente
Prof. Simone Genovesi

Thesis reviewers
Prof. Antonio Clemente
Prof. Simone Genovesi

Siena, 05/03/2024

Contents

1 Introduction **3**
1.1 Organization of the thesis 4

2 State of the Art **5**
2.1 Historical notes about Super-Directivity 5
2.2 Bounded Super-Directivity 7

3 Bounds on Super-Directivity **11**
3.1 Introduction 11
3.2 Q-Bounded Super-Directivity for Self-Resonant Antennas 12
3.2.1 Analytical form for Q-bounded maximum directivity 12
3.2.2 SW coefficients for maximum directivity 16
3.3 Small Antennas: Dipolar and Quadrupolar Resonant Sources 18
3.3.1 Minimum Q for Dipolar and Quadrupolar contributions 19
3.3.2 long title splitted 21
3.3.3 Multipole contributions without and with Q-bounds 24
3.4 Closed-form formulas for larger antennas 24
3.5 Maximum Directivity and Equivalent Radius for constant Q 27
3.6 Conclusions 27

4 Bounds on Super-Gain **31**
4.1 Introduction 31
4.2 Antenna Gain 31
4.3 Maximum Super-Gain Without Q-Bounds 32
4.3.1 Maximum Gain for Externally Tuned Antennas 32
4.3.2 Maximum Gain for Self-Resonant Antennas 36
4.3.3 Comparison with Gustafson-Capek results 37
4.3.4 Distribution of the currents coefficients 38
4.3.5 Physical interpretation for Small Antennas 41
4.4 Value of Q on the maximum gain curve 43
4.5 Maximum Super-Gain With Q-Bounds 46

4.6 Maximum Gain calculated by the discretization of the radiation operator 49
4.6.1 Maximum Gain for Spherical Shape 49
4.6.2 Maximum Gain for Parallelepipal Box Shape 52
4.7 Conclusions 54

5 Degrees of Freedom and relationship with Super-Directivity 55
5.1 Introduction 55
5.2 Degrees of Freedom and Maximum Directivity of non-super-directive antennas . 55
5.2.1 Degrees of Freedom for a limited angular region 57
5.2.2 Approximate expression of DoF for convex minimum region 57
5.2.3 DoF calculation by means of SVD 58
5.2.4 Spherical surface case 60
5.3 DoF link with correlation parameter 62
5.3.1 DoF-compliant beams and minimum ECC 63
5.3.2 Universal ECC 66
5.4 Conclusions 68

6 Conclusions 69

A Spherical Wave Function 75

B Equivalent Currents using SWs 77
B.1 Equivalent Currents Derivation in presence of electric currents 77
B.2 Equivalent Currents derivation in presence of electric and magnetic currents . . . 79

C Quality Factor 83

D Discretization of the radiation operator 87
D.1 Discretization of the radiation operator in terms of Spherical Modes 89

E Singular Value Decomposition 91

Bibliography 95

List of Figures

3.1 Q-bounded maximum directivity in (3.15) (continuous lines) at different constant Q values ($Q = 10$, $Q = 100$, $Q = 1000$, and $Q = 5000$) and the Harrington directivity (black dash-dotted lines) in (3.2). These curves are limited up to the Chu-limit radius kr_1, where the maximum directivity $D_{max}(Q, kr_{min}) = 3$. . . . 15

3.2 Parameter $\bar{\xi}$ that minimizes the summation in (3.15) (continuous line) and its approximation in (3.16) (dashed line) truncated at $Q = Q_2$, for various values of Q ($Q = 10, 12, 15, 20, 30, 40, 50, 60, 70, 80$). 16

3.3 Envelope of the maximum directivity summation terms in (3.15) for three values of Q ($Q = 10$, $Q = 100$, and $Q = 1000$) and two values of kr_{min}. Continuous lines and dash-dotted lines correspond to $kr_{min} = 5$ and $kr_{min} = 5$, respectively. Dotted black line represent the envelope of the Harrington coefficient for maximum directivity in (3.6). 17

3.4 Envelope of the amplitude of the coefficients in (3.18) for various values of kr_{min} and two values of Q, namely $Q = 10$ (continuous line) and $Q = 100$ (dashed line). 17

3.5 Graphical representation of a (a) Huygens' dipole (HD), (b) Huygens' Quadrupole (HQ) and (c) Vertical Dual Quadrupole (DVQ). 18

3.6 (a) normalized polar patterns and (b) 2D radiation patters of HD, HQ and combination of HD, HQ and DVQ for maximum directivity as in (3.15). h_{max} provides a maximum directivity of 8 (9.03 dBi), while the isolated h_{HD} and h_{HQ} provide a directivity of 3 (4.77 dBi) and 7.5 (8.75 dBi), respectively. 20

3.7 Dotted lines represent the maximum directivity as a function of the Q. Dots connected by dashed lines are obtained by ($D_{max} = 8$) and by ($D_{max} = 3$). Continuous lines are obtained through (3.15). Dash-dotted lines are obtained by using (3.23), namely setting Q constant for dipolar and quadrupolar contributions. The solution minimally deviates around with respect to eq. (3.15) since the latter include contribution of order 3 (hexapoles). 22

3.8 Bound of frequency bandwidth constrained super-Directivity (log-log scale) for different values of Q, truncated at the corresponding Chu-limit radius kr_1, where $D_{max} = 3$. Comparison between the exact formula (3.15) (continuous lines) and the approximate formula for small antennas in (3.23) (dashed lines). The validity range of the approximation is $kr_1 \leq kr_{min} \leq kr^{(2)}$. 23
3.9 Percentage error between the approximation in (3.23) and the exact formula in (3.15) for $Q = 10, 20, 30, 50, 100, 300, 500, 1000$ in the range from $kr_1 \leq kr_{min} \leq 0.8kr_2$. 24
3.10 Maximum directivity of a finite number of multipoles as a function of Q (dots connected by dashed lines) and as a function of Q derived (dashed lines) for $kr_{min} = 0.2, 0.5, 1, 2, 3$. The results are compared with the results obtained from (3.15). The vertical dotted lines correspond to the Chu-limit $Q = Q_1$. 25
3.11 Maximum directivity (log-log scale) for constant Q. The curves are truncated at the corresponding Chu-limit radius, where $D_{max}(Q, kr_{min}) = 3$. Comparisons of the exact formula (3.15) (continuous line) and the combination between (3.23) and (3.28) (dotted lines) for $Q = 10, 100, 1000, 5000$. 26
3.12 Percentage error between the approximation in (3.28) and the exact formula in (3.15) for $Q = 10, 20, 30, 50, 100, 300, 500, 1000$ in the range from $0.8kr2 \leq kr_{min} \leq 20$. 26
3.13 Bound of Super-Directivity (log-log scale) truncated at the corresponding Chu-limit radius kr_1. Comparisons of the exact formula (3.15) (continuous lines) and the combination between (3.23) and (3.28) (dash-dotted lines) for $Q = 10, 100, 1000, 5000$. 27
3.14 Ratio between r_{eq} and r_{min} as a function of kr_{min} for different values of Q, the curves are truncated at radius corresponding to the Chu-limit. The equivalent radius is obtained from the exact formula in (3.15) (continuous lines) and the combination between the approximate ones in (3.23) and (3.28) (dotted lines). The back dash-dotted line is obtained with the Harrington formula, i.e., $(kr_{min})^2 + 2(kr_{min})$. 28

4.1 Radiation resistance of individual harmonics for $n = 1, 2, 3, 4$ as a function of the minimum surface normalized radius for TM (continuous lines) and TE (dashed lines) modes. 33
4.2 Efficiency of the super-gain calculated for different values of R_Ω as a function of kr_{min}. 35
4.3 Maximum gain of externally tuned antennas calculated for different values of R_Ω as function of kr_{min} (continuous lines) and corresponding directivity (dashed lines) obtained by G_{max}/η. 35
4.4 Maximum gain calculated for different values of R_Ω as a function of kr_{min} for tuned antennas (dashed lines) and self-resonant antennas (continuous lines). . . . 37
4.5 Comparison between the maximum gain for the externally tuned case of our formulation (continuous lines) and the formulation in [1] (dashed lines), also obtained by using (4.19) in (4.11). The dash-dotted black line represent the Harrington limit, i.e., $(kr_{min})^2 + 2(kr_{min})$. 38

4.6 Histograms of current coefficients for TE (inductive, right-hand side) and TM (capacitive, left-hand side) harmonics with $R_\Omega = 10^{-1}\Omega$. (a)-(b) for externally tuned case, and (c)-(d) for self-resonant case. 39

4.7 Histograms of current coefficients for TE (inductive, right-hand side) and TM (capacitive, left-hand side) harmonics with $R_\Omega = 1\Omega$. (a)-(b) for externally tuned case, and (c)-(d) for self-resonant case. 40

4.8 Envelope of the current coefficients and their amplitude for different values of the surface: (a) $R_\Omega = 10^{-3}\Omega$; (b) $R_\Omega = 10^{-2}\Omega$; (c) $R_\Omega = 10^{-1}\Omega$; (d) $R_\Omega = 1\Omega$. The amplitudes are normalized to have a unit radiated power ($P_r = 1W$). The dashed vertical line denotes N_{DoF} in absence of Q-bounds. The red line (right-hand side scale) represents the radiation resistance of the SW harmonics. The ohmic surface resistance is indicated by a horizontal red line; it crosses the curve of the radiation resistance of the harmonics approximately at the maximum of the envelope. 41

4.9 Elementary source associated with the far-field pattern of dipolar $\boldsymbol{h}_1^{(TM)}$ (a), $\boldsymbol{h}_1^{(TE)}$ (c) and quadrupolar $\boldsymbol{h}_2^{(TM)}$ (b), $\boldsymbol{h}_2^{(TE)}$ (d) contributions. Electric dipoles (TM) are denoted in blue with a single arrow and magnetic dipoles (TE) with a double arrow. The vertical doublet is aligned along x for electrical dipoles and along y for magnetic dipoles. 42

4.10 Maximum gain for externally tuned antennas calculated for different values of R_Ω as a function of kr_{min} using the full series in (4.11) (continuous lines) and the two terms approximation for small antennas in (4.24) (dash-dotted lines). Dotted lines are the corresponding directivities obtained by G_{max}/η with the full series. 43

4.11 Maximum gain of self-resonant antennas calculated for different values of R_Ω as a function of kr_{min} using the full series in (4.16) (continuous lines) and the first two terms of the series in (4.16) valid for small antennas (dash-dotted lines). . . 44

4.12 Quality factor of spherical wave expansion with coefficients associated to the maximum gain (4.13). The two dashed dotted lines represents Q'_1 and Q''_2. 45

4.13 Q-bounded maximum gain in (4.32) as a function of the antenna size calculated for $Q = 10$ (a), $Q = 100$ (b), and $Q = 1000$ (c) and different values of the ohmic losses resistance R_Ω; the curves tend smoothly to the Q-bounded maximum directivity (black dash-dotted lines) when the losses tend to zero, i.e., the curve $R_\Omega = 0\Omega$ corresponds to the maximum Q-bounded super-directivity in (3.15). 47

4.14 Percentage difference between maximum Q-bounded directivity in (3.15) and maximum Q-bounded gain in (4.32) for different values of the loss resistance. The green curves correspond to an efficiency larger than 93% in the overall range from the Chu-limit. (a) $Q = 10$; (b) $Q = 100$; (c) $Q = 1000$. The horizontal scale start form the corresponding Chu-limit for the different values of Q. 48

4.15 Region of validity of the various formulas for Q-bounded maximum gain with losses in (4.32) and Q-bounded maximum directivity without losses. For $Q < 9/R_\Omega^{0.8} + 3$, eq.(4.32) can be used with a maximum error less than 7% for all antenna sizes. 49

4.16 (a) Graphical representation of the source region sphere (small green sphere) and of the observation far-field sphere (big blue sphere); (b) Graphical representation of the source region sphere, the red dot are the location of the two orthogonal electric dipoles. 50
4.17 Graphical representation of the box shape, the pair of orthogonal dipoles are located on the six faces of the box and separated by a distance d to each other. . 52
4.18 Graphical representation of the study case of the box circumscribed to the sphere (a) and of the box inscribed within the sphere (b). 52
4.19 Maximum gain of the box circumscribed to the sphere (continuous lines) compared with the one of the sphere (dotted lines) for different values of R_Ω. 53
4.20 Maximum gain of the box inscribed within the sphere (continuous lines) compared with the one of the sphere (dotted lines) for different values of R_Ω 53

5.1 (a) graphical illustration of the solid beam angle for a highly directive antenna. This angle is approximately equal to the product of the 3dB angles in the two principal planes. (b) illustration of the DoF as the number of beam angles coming from the maximum area of the sphere in independent directions. 56
5.2 Graphical illustration of the independent beams of beam angles $\Omega_{r_{min}}$ contained in a finite solid angle Ω. The number of these independent beams gives the degrees of freedom of the field in the solid angle Ω. 58
5.3 Graphical illustration of eq. (5.8). The N_{DoF} of sources contained in a given surface is interpreted as the number of sub-surfaces of area $(\lambda/2)^2$ that can be distributed over the surface. (a) actual surface; (b) minimum spherical surface. . 58
5.4 Singular values of the radiation operator for $r_{min} = 2\lambda$ and $R = 7\lambda$, showing the analytical solution and the solutions with different number of dipole sources. . . 62
5.5 Graphical representation of the two beams rotated by an angle α. 63
5.6 ECC for non-super-directive case varying the angle α; the vertical dashed line correspond to the angle α corresponding to a $kr_{min} = 20$. 64
5.7 ECC for super-directive case varying the angle α for $kr_{min} = 20$ and for $Q = 10, 100, 1000$. 65
5.8 Radiation Pattern for non-super-directive case (a) and for Q-bounded case with $Q = 100$ (b), for $kr_{min} = 20$. The blue curves correspond to the radiation pattern for the broadside beams, the red curves correspond to the radiation pattern for the rotated beams, and the green one to the sum of the two beams. The blue and the red curves approaches the maximum directivity, while the green curve does not reach the maximum directivity value. 65
5.9 2D radiation patterns of the broadside beam (blue curves) and of the sum of the four rotated beams (red curves), both for non-super-reactive case (a) and Q-bounded case with $Q = 100$ (b). 66
5.10 ECC % for the non-super-reactive case. The corresponding ECC is equal for two different values of the source size, i.e., $kr_{min} = 20$ (blue curve) and $kr_{min} = 25$ (red curve). 67

5.11 ECC % for the Q-bounded case with $Q = 10$ (a), $Q = 100$ (b), and $Q = 1000$ (c). The corresponding ECC is equal for two different values of the source size, i.e., $kr_{min} = 20$ (blue curves) and $kr_{min} = 25$ (red curves). 67

B.1 Graphical representation of the Equivalent Theorem. The sources can be enclosed by a minimum surrounding sphere S of radius r_{min}. 77
B.2 Graphical representation of the Equivalent Theorem considering only a set of electric currents $\boldsymbol{J}$. 78
B.3 (a) Graphical representation of Love's formulation of the equivalent currents; (b) the magnetic currents radiating on a perfect conducting sphere; (c) the magnetic currents radiate in presence of lossy conductor material with resistivity R_Ω. . . . 80

C.1 Fante's Q_n coefficients. The used log-log scale emphasizes the different behaviour of Q_n with corner at $kr_{min} \approx n$. 84

D.1 (a) Original problem, (b) Love's equivalent problem, and (c) the equivalent problem with only electric currents. 88
D.2 Equivalent currents radiating in presence of an object and different Green's function contributions (incident and scattered contributions) in both near (a) and far (b) zone. 89
D.3 Spectral lattice of directions $\hat{\boldsymbol{r}}_m$; $m = 1, ..., M$ for the definition of the far field. For simplicity, the figure is referred to free-space Greens function. 90

E.1 Visualization of the matrix multiplication in singular value decomposition. 91
E.2 Visualization of the matrixes $[V]$ (a) and $[I]$ (b) showing their orthogonality. . . 92
E.3 Mapping of the vector columns of $[I]$ onto the vector columns of $[V]$ through the $[F]$ matrix. 93

Abstract

The thesis focuses on the definition of bounds for maximum directivity and gain of antennas. The main goal is to establish an analytical formula for maximum super-directivity considering specific parameters like bandwidth and antenna size. The upper limit on directivity for self-resonant antennas within a minimum sphere is determined based on a given quality factor. The formulation, obtained through rigorous convex problem-solving, is expressed as a rapidly converging analytical series. Approximate closed-form formulas are derived, showing high accuracy in various ranges of the minimum circumscribed sphere's radius, including small and intermediate to large antennas. Special attention is given to small antennas, interpreting the solution as a combination of dipolar and quadrupolar Huygens' source contributions with closed-form coefficients. The solution maintains continuity to the maximum directivity between 3 and 8 while holding a constant Q. The challenge of achieving super-gain is addressed by assuming small losses in terms of surface resistance over the metalized surface of the minimum sphere circumscribing the antenna. The final closed-form formula indicates that maximum gain results from a summation similar to Harrington's sum for maximum directivity, with coefficients weighted by the radiation efficiency of each spherical harmonic. The formulation is extended to self-resonant antennas, providing a tighter bound for any losses. The thesis further explores the relationship between maximum directivity and the Degrees of Freedom (DoF) of the fields.

Chapter 1

Introduction

This research initiative originated with the aim of improving the performance of low-band base station antennas in 5G networks by creating a broad-band, high-gain radiator. 5G antennas represent a paradigm shift in wireless communications, introducing distinct features and presenting significant challenges. The crucial aspect of the directional operation of 5G antennas involves dynamic responses to connected devices' requests, contrasting with the continuous emission of radio waves within a specific cell, as seen in traditional antennas. This dynamic mode optimizes resource usage, minimizing radio wave emissions when not strictly necessary to avoid additional interference. Further benefit is the energy-saving capacity of these antennas, reducing environmental impact and contributing to the overall energy efficiency of network infrastructures. Despite these advantages, 5G antennas face various challenges, including limited coverage. This issue raises concerns about inclusivity and accessibility, emphasizing the need to extend coverage for uniform connectivity across the entire territory. The design of antennas for 5G communication systems presents challenges due to constrained dimensions, particularly in lower frequency bands where antennas are larger. Addressing user interference in the emerging MIMO system is crucial, with key parameters including gain, bandwidth, and isolation between ports. The main objective is to increase antenna gain, reducing the number of base stations, mitigating interference, and lowering overall power consumption. Recent demands for highly directive electrically small radiators and scatterers in communication and sensor applications have revived interest in the concept of super-directivity. This interest arises from the necessity for improved performance in terms of range, resolution, and sensitivity in communication and sensing systems. In conclusion, 5G antennas, with their innovative features, present a multitude of complex challenges. The ongoing evolution of technology is likely to reveal additional issues in implementing this revolutionary communication infrastructure. It is crucial to address these challenges thoughtfully, considering both positive and negative impacts, to ensure a smooth transition towards an increasingly connected society. The purpose of this project is to conduct a study to enhance the directivity and gain of radiating elements, highlighting the theoretical limits that exist for such a goal. Super-directivity can be exploited to increase the reactive area, this means that the super-reactive effect produces an effective area that becomes larger than the physical area of the antennas itself. A larger reactive effective area generally indicates that the antenna can capture larger amount of power from the incoming signal, resulting in a stronger received signal and a higher antenna efficiency. This is crucial in wireless communications, where signal strength can significantly influence the quality of the communication. However, this implies a strong reactive field that reduces the bandwidth. It is well known that the gain, as well as the directivity, is not mathematically limited, but a small sized antenna with extremely high gain produces a high reactive field intensity in the proximity of the an-

tenna, resulting in high losses and high stored energy, and consequently, a narrow bandwidth. Therefore, the quality factor is pivotal to evaluate the performance of an antenna system due to its primary relationship with the stored energy and bandwidth. One of the first points of this project is to study the limitation of the product bandwidth-gain. Despite the fact the limitation in bandwidth and in gain of an antenna has been a field of interest, an expression connecting both bandwidth and gain has not founded so far. The main objective of this thesis is to obtain the maximum super-directivity for a given bandwidth and given size of the antennas and derive analytical closed form for it. The analytical formula permits to have an immediate feedback and idea of the possible main characteristics and antenna design parameters of the antenna under design, dealing with both small and large antennas. This part will be the most extensive one and will also include physical insight about possible antenna designs to incorporate additional information about the limitation of the product bandwidth-gain. In the second stage of this project the maximum antenna super-directivity is investigated in relationship with the number of Degrees of Freedom (DoF) of the electromagnetic field. The numbers of Degrees of Freedom are the minimum number of parameters necessary to describe the electromagnetic field at a certain distance from a minimum surface enclosing the sources, so that the reactive field is negligible. This number is determined by the limited spatial bandwidth of the electromagnetic fields and has a direct proportionality to the square of the radius of the smallest sphere that can enclose the sources, with the radius being measured in wavelength units. In this context, the investigation of maximum antenna super-directivity in relation to the number of DoF becomes a crucial aspect of this project. By understanding this relationship, we can potentially optimize the design of super-directive antennas, balancing the trade-offs and pushing the boundaries of what is currently achievable in antenna technology. This could open new possibilities in various fields, from telecommunications to space exploration, enhancing the efficiency and effectiveness of wireless communication systems.

1.1 Organization of the thesis

The thesis provides a succinct overview that attempts to encapsulate the author's investigation into super-directivity and super-gain analysis and synthesis, placing this research in the context of the existing body of knowledge. The primary insights shared here are derived from two papers written during the course of the Ph.D. studies [2] [3], presented in a more detailed format than their original versions. Chapter 2 explores the historical evolution and current advancements in super-directive antennas and related topics, merging historical advancements with the most recent discoveries. Chapter 3 elaborates on the boundary of super-directivity, followed by an examination of the boundary on super-gain in Chapter 4. Chapter 5 investigates the Degrees of Freedom (DoF) theory in relation to super-directivity. Chapter 6 marks the principal results of the dissertation, providing also a possible future plans.

Chapter 2

State of the Art

This chapter offers a thorough review of the current state-of-the-art topics discussed in this thesis. The concepts of super-directivity and super-gain have brought about a revolution in antenna design, allowing for exceptional levels of signal strength and directionality. This Chapter also underscores significant research studies and technological advancements that have contributed to our comprehension of these subjects. It lays the groundwork for the following Chapters, where we will further investigate these concepts and examine their practical implications in contemporary antenna systems.

2.1 Historical notes about Super-Directivity

Super-directivity refers to the ability to achieve exceptionally high levels of directivity, beyond what is traditionally achievable with conventional antenna designs. This advanced characteristic allows super-directive antennas to precisely focus and concentrate electromagnetic signals in a specific direction, enhancing the general performance of the communication systems.
The challenge of super-directivity can be traced back to 1922 when Oseen, in his seminal work on "Einsteinian needle radiation" dealt with the application of Maxwell's equations to clarify the phenomenon wherein the radiation emanating from a large point source disperses infinitely. In his publication [4], Oseen wanted to solve the problem of how a minute atom, alike to a photon, absorbs energy from an incident wave. Oseen postulated that an atom could only absorb energy by emitting its own wave, which, in part, cancel out the incident wave. Without such partial cancellation, the incident wave would carry the same energy to infinity, regardless of whether there is absorption or not, which is physically impossible. The concept of "needle radiation" introduced by Oseen is intricately linked to the fascinating question of how a very small atom can effectively absorb energy from a substantial electromagnetic wave. It is noteworthy that Oseen's exploration not only sheds light on the absorption process but also extends to the converse challenge—transmitting a radiation pattern akin to a needle from a compact source. In essence, this reciprocal problem highlights the pursue for achieving super-directivity in radiation patterns, mirroring the needle-like characteristics encountered in absorption scenarios.
The concept of super-directivity is indeed fascinating. Super-directivity is a concept related to antenna arrays, where the focus is on creating more compact antenna arrays to achieve higher directivity. It is based on the principle of destructive interference, which can occur in all directions, including the direction of the main lobe. In the context of antenna design, destructive interference is used to suppress radiation in unwanted directions, thereby enhancing the directivity of the antenna. This is achieved by carefully designing the antenna elements and their relative phases such that the electromagnetic waves they emit interfere destructively in undesired

directions. This principle allows super-directive antennas to focus their radiation pattern more narrowly, resulting in a higher gain in the desired direction. However, it is worth noting that super-directive antennas often require more complex designs and can be more sensitive to manufacturing errors and signal noise. They also tend to have a higher Q-factor, which can limit their bandwidth. In summary, super-directivity is a powerful concept in antenna design that leverages the principle of destructive interference to achieve higher levels of directivity than conventional antennas. This makes them particularly valuable in applications where precise control of the radiation pattern is crucial. However, these benefits come with trade-offs in terms of design complexity, sensitivity to errors and noise, and potentially limited bandwidth. However, the direction of the main lobe corresponds to the direction on which the interference is minimum; this implies that arbitrarily high directivity could be achieved with an array of finite size [5].
In [6] the authors demonstrate that in certain types of directional antenna arrays, the gain can be increased by arranging the waves so that they do not strictly fade at large distances as they go from the array elements in the direction of maximum transmission, proposing an end-fire array solution. [7] presents a mathematical theory to evaluate and control the directive properties of linear array, in the paper broadside pattern enhancements from different array configurations were considered. The mathematical theory developed by Schelkunoff provides a framework for calculating and controlling the directional properties of the antenna arrays. In other words, it allows to understand how electromagnetic waves propagate from linear antenna arrays and how one can manipulate it to achieve a desired radiation pattern. La Paz and Miller in [8] defined the theoretical optimum current distribution on a vertical antenna of a given length as the current distribution that provides the maximum possible field strength on the horizon for a given power output. This concept was introduced to improve the overall performance in directional antenna applications. However, later on, Bouwkamp and De Bruijn in [9] individuate an error in their theory and demonstrated that there was no theoretical limit on the directivity from an aperture of any size. Bouwkamp and De Bruijn demonstrate that the problem of the optimal current distribution does not have an exact solution. Instead, they develop a method to realize any given vertical radiation patter through an appropriate choice of the current distribution. In this way, it is feasible to construct theoretical current distributions that are much better then the one proposed by La Paz and Miller. In 1946 Dolph [10] presented a method to design arrays with a desired side-lobe level. This method is based on family of current distribution using the Chebyshev polynomial to produce an array pattern that satisfy the requirement on the level side-lobes. This kind of array are well known as Dolph-Chebyshev arrays. Riblet in [11] [12] developed a super-directive Dolph-Chebyshev arrays for spacing below $\lambda/2$, he also illustrate that this influence the main lobe.
The aforementioned papers, along with their respective historical references, are, of course, only a portion that constitutes references for an initial approach to super-directive antennas and their potential implementations. These sources serve as a foundation for further exploration into the subject, providing valuable insights into the historical context and practical applications of super-directive antenna technology.

2.2 Bounded Super-Directivity

Numerous authors have demonstrated that super-directive antennas necessitate to a constraints. The issue of the maximum limit of directivity has been extensively researched by many esteemed scientists [13–24].

Chu [25] is likely the first to have undertaken an analysis of the fundamental limitations of antennas in the context of the radiansphere. The concept of the radiansphere was initially introduced by Wheeler in [26], and further expanded upon in the same work to include non-spherical radiators [27]. Chu established the lowest Q-factor and the highest gain of a linearly polarized omni-directional antenna, utilizing the spherical wave functions expansion outside the smallest sphere enclosing the antenna. In [18], Hansen analyzes the fundamental limitation for electrically small antennas, super-directive antennas, super-resolution antennas, and high-gain antennas. Assuming sources fitting inside a minimum sphere of radius r_{min}, the maximum directivity can be found as suggested by Harrington [28] [29] [30]. His method, that will be analysed in next Chapter, is based on the expansion of the radiated field in a finite number of spherical waves (SWs), and on the maximization of the directivity with respect to the coefficients of the expansion. It was suggested by Harrington to excite a finite number of SWs; this number of maximum SWs that can be excited is the largest integer smaller than kr_{min}, where k is the free-space impedance. This procedure invokes the difficulty to excite higher order of SW harmonics with sufficiently high intensity over the minimum sphere to significantly contribute to the far field; namely, as underlined in [31], it relies on the finiteness of the number of Degrees of Freedom of the field in the far zone. To put it differently, Harrington's procedure is grounded in the understanding that the SWs are below cut-off as long as the order of the spherical Hankel function is larger than its argument. This is actually the same concept invoked to establish the number of DoF of the field radiated by sources inside a minimum sphere. It is well-known that there exist super-directive antennas, with directivity larger than the limit proposed by Harrington even if with a small bandwidth. The possibility to exceeded the Harrington limit derives from the fact that its derivation does not consider the change to excite, with a sufficiently large intensity over the minimum sphere, SWs with polar index larger than kr_{min}. As a matter of fact, increasing the number of super reactive harmonics over the minim sphere leads a diverging Q-factor, which is eventually useless for practical antenna applications, since the bandwidth goes to zero. Vice-versa, allowing for a certain desired maximum Q may imply a bound of directivity larger than the one derived by Harrington. In [32] the relationship between antenna directivity and size is discussed, proposing a normalization of the Harrington limit to fulfill both directivity definition and physical behaviour, this has been done considering a new effective radiansphere $k(R + \frac{1}{2\pi})$. Reference [33] presents a formula for accurately estimating the total radiated power from a transmitting antenna, the derivation is conducted using the theory of spherical wave expansion of electromagnetic fields. The paper also establishes a simple criterion for the required number of samples of the power density. [34] discusses the constraint on the maximum available directivity measured on a single port and multiple ports of both small and large antennas. The effect of the coupling is also mentioned since a reduction in gain can be characterized in terms of coupling efficiency and in consequent reduction of the total radiated power.

The paper [35] addresses the problem of minimizing the signals received from interfering or

undesirable signal sources by appropriately modifying the antenna radiation pattern, exploring the physical limitations that exist when trying to reduce interference through antenna pattern shaping. It is also shown that the field components with spatial variation of a period smaller than a wavelength contribute essentially reactive power. They increase the Q-factor of the aperture and impose a limitation on the pattern.

Other studies have concentrated on finding the optimal balance between antenna directivity and bandwidth [1,14,36–41]. Indeed, the definition of the maximum directivity for a given electrical size of the minimum sphere circumscribing the antenna requires a constraint to ensure a finite bound, as without it the directivity could be in principle infinite. This constraint can take the form of upper-limit on the Q-factor, i.e., minimum relative frequency bandwidth, among other possibilities [14]. Fante [36] proposed a maximization of the product directivity-bandwidth; he used the term gain, even if the treatment is relevant to directivity. The coefficients of the SWs found by Fante are different from the ones found by Harrington, and the series is not truncated. However, the D/Q bound obtained in this way is always relevant to small Q (large bandwidth) and moderate D, which is of practical interest only for ultra-wideband antennas. In [42], the minimum Q-factor for a given directivity of small antenna of arbitrary shape is obtained by setting a convex problem and solving it by a semidefinite relaxation technique. Geyi, in [38], carried out a comprehensive analysis on minimizing the Q-factor and its trade-off with the maximum value of G/Q, exploring the physical limitation of omni-directional antennas and using the spherical wave expansion to describe the field.

Gustafsson gives an extensive contribution to the exploration of the physical constraints of antennas, particularly in the assessment of bandwidth limits associated with super-directivity. In [43], a paper of which he is a co-author, he generalizes the Chu results for arbitrary antennas shape, i.e., non-spherical geometries. The theory is verified against the classical Chu limitations for spherical geometries and shown to yield sharper bounds for the ratio of the directivity and the Q-factor for non-spherical geometries. The product of bandwidth and realizable gain is shown to be bounded by the eigenvalues of the long-wavelength, high-contrast polarizability dyadics. These dyadics are proportional to the antenna volume and can be easily determined for an arbitrary geometry. In [1] Gustafsson-Capek presented a results based on a Methods of Moments (MoM) applied to the surface of an arbitrary metallic body and by a convex optimization procedure. They found the maximum super-gain by imposing a maximization of the power intensity with constant radiated power for any coefficient of the MoM basis functions, assuming small losses on the metallic shape. This procedure is quite general and can be applied to arbitrary shape. In [44] he discusses the challenges in designing small antennas due to their hight Q-factor (low bandwidth) and efficiency. The procedure is again conducted by means of the convex optimization of the current that provide upper bounds on the antenna. The paper also presents an optimized maximum gain Q factor quotient. In [45] the problem about the fundamental lower bound on the radiation of Q has been addresses for small electrical antenna, resulting of importance in relationship with the antenna bandwidth. [45] also discusses on the relationships between the losses in the antenna and the losses in the matching network, and their possible effect on the system bandwidth, the system efficiency. The investigation of super-directivity in MIMO antenna system is also examined in [46], where the analysis also involves the antenna loss. Reference [47] provides a framework for illustrating the achievable super-directivity achievable by a MIMO system. [48] presents a new approach to antenna directivity,

leading on massive MIMO application scenario. This theory is used for the analysis and synthesis of antenna systems, and it integrates with global optimization algorithms. The authors combine the infinitesimal dipole model (IDM) and the cross-correlation Green's function (CGF) in a new formulation, referred to as the IDM-CGF method. The realization of practical small and high directive antenna is one of the focus research of Richard W. Ziolkowski, who gives different contributions in these field. In [49] [50–55] presents a significant advancement in the field of electrically small antennas, tying to design small antenna capable to achieve simultaneously high radiation efficiencies, directivities, and front-to-back-ratios over a broad bandwidth.
Several contributions [2, 3, 56–58] provide fresh and intriguing insights into the boundaries and limitations of super-directive antennas. These studies delve into the exploration of achieving high levels of directivity in antenna system performance. As a result, it becomes evident that this research field is a hot topic in antenna theory, gaining significant attention, particularly in light of the expanding landscape of wireless and 5G antenna environments. The investigation of super-directive antennas not only contributes to advancing the theoretical understanding but also holds practical implications for the evolving technologies in the wireless communication scenario.

Chapter 3

Bounds on Super-Directivity

3.1 Introduction

In absence of super-reactive source, the maximum available directivity is the one of a large illuminated circular aperture of area A and the same radius of the sphere surrounding the source kr_{min}, namely

$$D_{max} = 4\pi \frac{A^{(circular)}}{\lambda^2} = (kr_{min})^2 \tag{3.1}$$

One of the simplest ways to obtain this number is counting the number of spherical waves that have experienced the cut-off transition on the minimum-sphere surface [59]. Expression in (3.1) is also related to the maximum directivity of non-super-reactive sources inside a sphere whose radius is large is terms of wavelength [19]. Assuming non-super-reactive sources that fit within a minimum sphere of radius r_{min}, the maximum directivity can be found as suggested by Harrington [28] [60] [29]. His method is based on the expansion of the radiated field in a finite number of spherical waves (SWs) and the maximization of directivity with respect to the coefficients of the expansion. This procedure leads to

$$D_{max} = \sum_{n=1}^{N_{max}} (2n+1) = (N_{max})^2 + 2N_{max} \tag{3.2}$$

Consequently, the maximum directivity depends on the value set for the maximum polar index N_{max} of the spherical waves (SWs) contributing to the far-field for the given minimum sphere ($N_{max} \geq 1$). Harrington suggested that, for the case of non-super-reactive antennas, the maximum polar index should be set as the largest integer smaller than the electrical radius, namely $N_{max} = \lceil kr_{min} \rceil$. This results in the continuous formula for maximum directivity

$$D_{max} = (kr_{min})^2 + 2kr_{min} \tag{3.3}$$

This assumption presents the challenge of exciting SWs with polar indices $n > kr_{min}$ with sufficient intensity over the minimum sphere to significantly contribute to the far field. In essence, this approach is grounded in the understanding that the SWs are below the cut-off as long as the order of the spherical Hankel function is larger than its argument. To ensure continuity in the maximum directivity formula around this value, it was proposed in [31] that the maximum directivity for non-super-reactive antennas (without bandwidth limitation) can be defined as

$$D_{max} = \begin{cases} (kr_{min})^2 + 2(kr_{min}) & \text{for } kr_{min} \geq 1.5 \\ (kr_{min})^2 + 3 & \text{for } kr_{min} < 1.5 \end{cases} \tag{3.4}$$

The heuristic expression (3.4) serves as a practical reference for antenna designers, indicating a directivity limit. Although certain antennas exceed this limit, known as *super-directive*, our analysis ignores the possibility to excite with enough intensity spherical waves (SWs) with polar indices greater than $N_{max} = \lfloor kr_{\min} \rfloor$ with adequate intensity over the minimum sphere. Mathematically, an infinite number of super-reactive harmonics can be excited over this sphere, leading to unbounded super-directivity. To calculate the maximum directivity of an antenna, it is necessary to apply certain limitations to avoid infinite results. These constraints might involve setting lower efficiency limits, bandwidth limits, or restricting the number of harmonics based on the field's degrees of freedom. This study primarily focuses on achieving a bandwidth limit on maximum directivity.
The concept of bandwidth is closely connected to the quality factor (Q-factor); actually, it can be expressed as the reciprocal of the fractional bandwidth, $BW = 1/Q$, for sufficiently large values of Q ($Q > 10$) [21]. A higher Q-factor generally results in a narrower bandwidth because antennas with higher Q-factors are more selective in terms of the frequencies they can efficiently radiate or capture. Conversely, antennas with lower Q-factors tend to have broader bandwidths, enabling them to cover a wider range of frequencies. Therefore, the Q-factor of an antenna is a crucial parameter that characterizes its efficiency and performance. It quantifies the antenna's ability to store and radiate energy with minimal losses, indicating low resistive losses and efficient conversion of electrical power into electromagnetic radiation.
In the following the investigation about the maximum super-directivity with Q-bound is conducted. However, it is important to remember that choosing the right Q-factor and bandwidth for an antenna is dependent on the specific needs of the application.

3.2 Q-Bounded Super-Directivity for Self-Resonant Antennas

In deriving the Q-bounded maximum directivity, we will refer to the equivalent problem presented in Appendix B and depicted in Figure B.3(a). In this formulation, the currents are expanded in terms of spherical wave harmonics with coefficients denoted as C_i, following the normalization specified in Hansen's book [61]. Since Love's formulation of the equivalence theorem is applied, it is assumed that the field inside the minimum sphere is zero, making it non-equivalent in terms of stored energy to the initial problem. However, because the energy of the equivalent problem is zero inside the sphere, any other source generating the same external fields will result in a higher Q. Consequently, the bounds obtained here are more optimistic than those obtained using electric currents only over a sphere, where energy can be stored even inside the sphere. Furthermore, since the energy stored is zero, a bound for self-resonant antennas is addressed.

3.2.1 Analytical form for Q-bounded maximum directivity

From the general definition of directivity, given by the ratio between the radiation intensity U and the total power radiated P_r [62], i.e.,

$$D = 4\pi \frac{U}{P_r} \tag{3.5}$$

where the U is the radiation intensity and P_r is the power radiated that in terms of SW expansion can be written as $U = \frac{1}{4\pi}|\sum_i C_i \boldsymbol{K}_i|^2$ and $P_r = \frac{1}{2}\sum_i |C_i|^2$, respectively. In maximizing the directivity, and exploiting the symmetry of the spherical source region, it is sufficient to consider only the broadside direction $(\theta, \phi) = (0, 0)$; this implies that only azimuthal wavenumbers $m = \pm 1$ will contribute to the radiated field. Hence, the far-field pattern are

$$K_i = \sqrt{2n+1}\begin{cases} 0 & \text{if } |m| \neq 1 \\ -(-j)^n & \text{if } s = 1, m = \pm 1 \\ -m(-j)^n & \text{if } s = 2, m = \pm 1 \end{cases} \tag{3.6}$$

Note that (3.6) is congruent with the normalization of Hansen's book [61], for which the power transported by an individual harmonic is $P_r = \frac{1}{2}|C_i|^2$. Since the maximum directivity is a convex function, the maximum directivity with Q-bound can be formulated in terms of a convex optimization problem, namely

$$\begin{aligned} \max_{C_n} \quad & \frac{\left|\sum_n C_n K_n\right|^2}{\sum_n |C_n|^2} \\ \text{s.t.} \quad & \frac{\sum_n Q_n |C_n|^2}{\sum_n |C_n|^2} \leq Q \end{aligned} \tag{3.7}$$

where Q_n are the Fante's quality factors of the polar harmonics defined in Appendix C and Q is the maximum accepted Q-factor (minimum relative bandwidth). It is important to observe that the inequality in (3.7) is actually equivalent to an equality, since any increase in the amplitude of the higher-order coefficients that provides larger directivity also implies an increase in Q. Therefore, finding the maximum directivity for a given maximum Q means, in practice, finding it for a constant Q.

Because the constraints are solely based on the magnitude of the coefficients, the maximum value in (3.7) is attained when $\angle C_i = -\angle K_i$, resulting in $C_i K_i = |C_i||K_i| = |C_n|\sqrt{2n+1}$. Consequently, we can exclusively utilize the polar index n, as the magnitude of K_i remains unaffected by the indices m and s. When setting the radiated power to unity, ensuring that $\sum_n |C_n|^2 = 1$, the problem in (3.7) becomes equivalent to

$$\begin{aligned} \max_{|C_n|} \quad & \left(\sum_n |C_n|\sqrt{2n+1}\right)^2 \\ \text{s.t.} \quad & \sum_n |C_n|^2 = 1 \\ & \sum_n Q_n |C_n|^2 = Q \end{aligned} \tag{3.8}$$

We can reformulate (3.8) by using its dual problem [63] obtained by multiplication with a scalar parameter ξ, namely

$$\begin{aligned} \min_{\xi} \max_{|C_n|} \quad & \left(\sum_n |C_n|\sqrt{2n+1}\right)^2 \\ \text{s.t.} \quad & \sum_n \Big[\xi(Q_n - Q) + 1\Big]|C_n|^2 = 1 \end{aligned} \tag{3.9}$$

Solution of the convex optimization problem

The solution of the problem in (3.9)for $Q \geq Q_1$ is provided by the Lagrange multiplier method [63]. To achieve this, we define the Lagrangian function for the problem in (3.9) as follows:

$$\Lambda(C_n, \lambda) = \Big(\sum_n C_n K_n \Big)^2 - \lambda \Big(\sum_n \big[\xi(Q_n - Q) + 1 \big] C_n^2 - 1 \Big) \tag{3.10}$$

where $C_n = |C_n|$ and $K_n = |K_n| = \sqrt{2n+1}$. The problem is structured such that the minimum with respect to ξ of the value λ, which maximizes the Lagrangian, represents the maximum directivity with Q-bound. To find this value, we differentiate the Lagrangian function in (3.10) with respect to λ and C_m and set the partial derivatives to zero:

$$\frac{\partial \Lambda(C_n, \lambda)}{\partial C_m} = 2|K_m| \sum_n C_n |K_n| - 2\lambda \Big[\xi(Q_n - Q) + 1 \Big] C_m = 0 \tag{3.11a}$$

$$\frac{\partial \Lambda(C_n, \lambda)}{\partial \lambda} = \sum_n \Big[\xi(Q_n - Q) + 1 \Big] C_n^2 - 1 = 0 \tag{3.11b}$$

Equation (3.11b) ensures compliance with the Q-bound after minimization, while eq.(3.11a) is satisfied if and only if

$$\sum_n C_n |K_n| = \lambda \tag{3.12a}$$

$$|K_m| = \big[\xi(Q_n - Q) + 1 \big] C_m \tag{3.12b}$$

Substituting the equality in (3.12b) into 3.12a) and using $|K_n| = \sqrt{2n+1}$ results in:

$$\lambda = \sum_n \frac{2n+1}{\big[\xi(Q_n - Q) + 1 \big]} \tag{3.13}$$

from which the maximum directivity is obtained by minimizing with respect to ξ. The range of variation of ξ is determined by imposing that the constraint terms are non-negative, $\xi(Q_n - Q) + 1 \geq 0$ for all n; i.e.,

$$Q_n > Q : \xi \geq \max \left\{ \frac{1}{Q - Q_n} \right\} = 0 \tag{3.14a}$$

$$Q_n < Q : \xi \leq \min \left\{ \frac{1}{Q - Q_n} \right\} = \frac{1}{Q - Q_1} \tag{3.14b}$$

Finally, we obtain the result

$$D_{max}(Q, kr_{min}) = \min_{\xi \in [0, \xi_{max}]} \sum_{n=1}^{\infty} \frac{2n+1}{\bar{\xi}(Q_n - Q) + 1} \tag{3.15}$$

In (3.15), $\xi_{max} = 1/(Q - Q_1)$ and $\bar{\xi} = \bar{\xi}(Q, kr_{min})$ represents the value of ξ that minimizes the infinite summation in (3.15). Equation (3.15) relates the maximum directivity to the antenna size's bandwidth. In Figure 3.1 the maximum directivity for different values of the Q-bound has been plotted and compared with the Harrington maximum directivity in (3.2); note that the Harrington directivity (black dash-dotted line) is lower wrt the Q-bounded maximum directivity

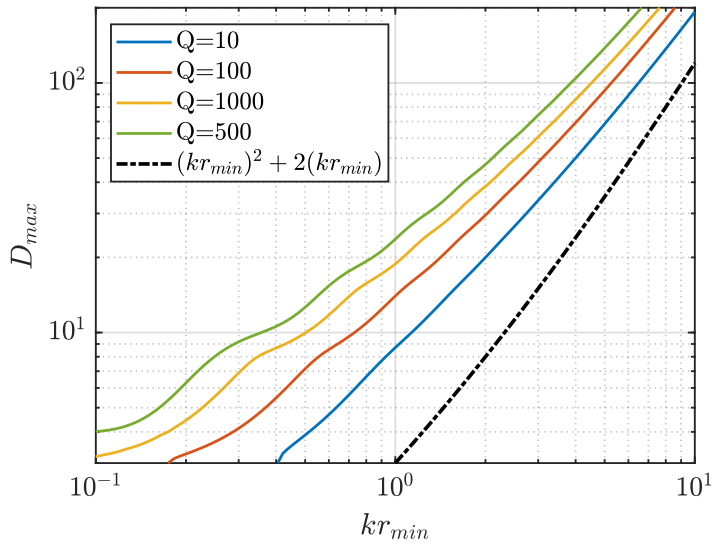

Figure 3.1: Q-bounded maximum directivity in (3.15) (continuous lines) at different constant Q values ($Q = 10$, $Q = 100$, $Q = 1000$, and $Q = 5000$) and the Harrington directivity (black dash-dotted lines) in (3.2). These curves are limited up to the Chu-limit radius kr_1, where the maximum directivity $D_{max}(Q, kr_{min}) = 3$.

derived in (3.15) supporting the fact that a higher directivity exists. The value of $\bar{\xi}$ that minimizes the series in (3.15) in the given range is illustrated in Figure 3.2 as a function of kr_{min} for fixed Q values. An excellent approximation of $\bar{\xi}$, valid for $Q_1 \leq Q \leq Q_2$, is given by

$$\bar{\xi} \approx \frac{8}{3(Q_2 - Q)} \left(-1 + \sqrt{1 - \frac{60(Q_2 - Q)}{256(Q_1 - Q)}} \right) \tag{3.16}$$

Figure 3.2 depicts the parameter $\bar{\xi}$ that minimizes the summation in (3.15) (continuous lines) and its approximation in (3.16) (dashed lines) truncated at $Q = Q_2$ for various Q values ($Q = 10, 12, 15, 20, 30, 40, 50, 60, 70, 80$). We observe that $\bar{\xi}$ tends to diverge for $Q = Q_1$. However, it can be easily seen that $\bar{\xi}(Q_1 - Q)$ in the denominator of (3.15) approaches zero, while all other terms in the series are negligible, given the high values of $\bar{\xi}(Q_1 - Q)$ for $n \neq 1$. Therefore, $D_{max}(Q, kr_{\min})$ approaches 3 for any Q when $Q_1 \approx Q$. This is expected since in the quasi-static limit, a sphere can only contain a self-resonant source, which is the Huygens' dipole.
The envelope of the terms inside the summation in (3.15) is plotted in Figure 3.3 for three Q values ($Q = 10, 100, 1000$), and two values of kr_{min} ($kr_{min} = 5, 10$). The dotted black line represents the envelope of the Harrington coefficient for maximum directivity in (3.6). For a low Q value, the envelope of the coefficients reaches the maximum close to $n = kr_{min}$. However, as Q increases, this maximum shifts towards higher values, which are defined by $Q = Q_n$ and correspond to specific antenna sizes denoted by kr_n. For $n > kr_n$, the coefficients for both field and directivity expansions exhibit rapid decay, the rate of which depends on kr_{min} and Q. This behavior arises from the change in the decay rate of Q_n when crossing kr_n (see Figure C.1 in

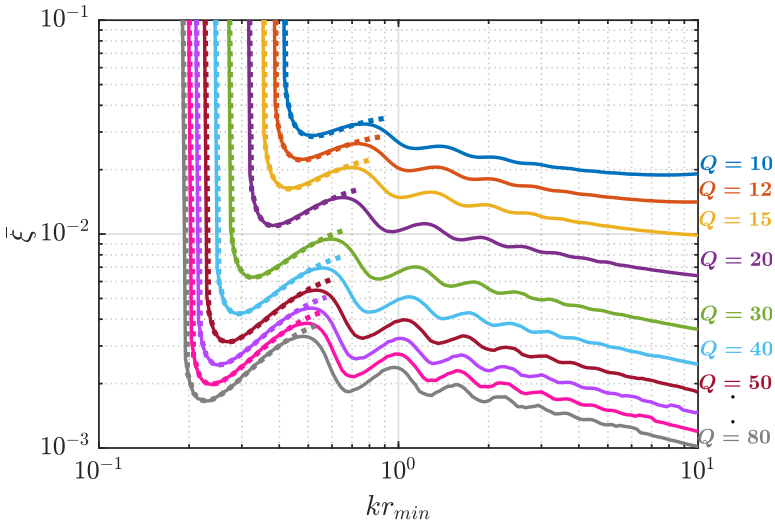

Figure 3.2: Parameter $\bar{\xi}$ that minimizes the summation in (3.15) (continuous line) and its approximation in (3.16) (dashed line) truncated at $Q = Q_2$, for various values of Q ($Q = 10, 12, 15, 20, 30, 40, 50, 60, 70, 80$).

Appendix C). An approximation for values of Q larger than 100, $kr_{min} < 2$, and $n < 12$ is given by:

$$kr_n \approx \frac{n}{1.356Q^{1/(2n+1)}} \tag{3.17}$$

3.2.2 SW coefficients for maximum directivity

The coefficients that yield the maximum directivity can be derived from the equation in (3.15); they are defined as

$$C_{i,max}^{(Q)} = \frac{C_0\sqrt{2n+1}}{\bar{\xi}(Q_n - Q) + 1} \begin{cases} 0 & \text{if } |m| \neq 1 \\ -(j)^n & \text{if } s = 1, m = \pm 1 \\ -m(j)^n & \text{if } s = 2, m = \pm 1 \end{cases} \tag{3.18}$$

where C_0 is an arbitrary constant. When $\bar{\xi}(Q_n - Q) \ll 1$, the coefficients $C_{i,max}^{(Q)}$ return the coefficients derived by Harrington in (3.6) without enforcing the Q-bound and simply truncating the series. It is important to emphasize that the selection of SW coefficients in (3.18) also ensures equality between electric and magnetic energy for $r > r_{min}$ across all polar indices n. This condition signifies that the maximization is specifically relevant to self-resonant antennas. The amplitude envelope of the coefficients in (3.18) in dB scale is depicted in Figure 3.4 for two Q values ($Q = 10$ and $Q = 100$) and various kr_{min} values. Note that the arbitrary constant C_0 is set to unity in the calculations.

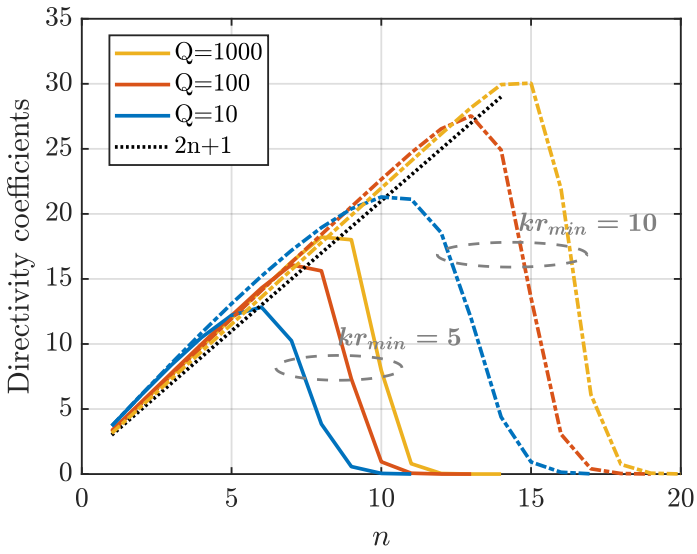

Figure 3.3: Envelope of the maximum directivity summation terms in (3.15) for three values of Q ($Q = 10$, $Q = 100$, and $Q = 1000$) and two values of kr_{min}. Continuous lines and dash-dotted lines correspond to $kr_{min} = 5$ and $kr_{min} = 5$, respectively. Dotted black line represent the envelope of the Harrington coefficient for maximum directivity in (3.6).

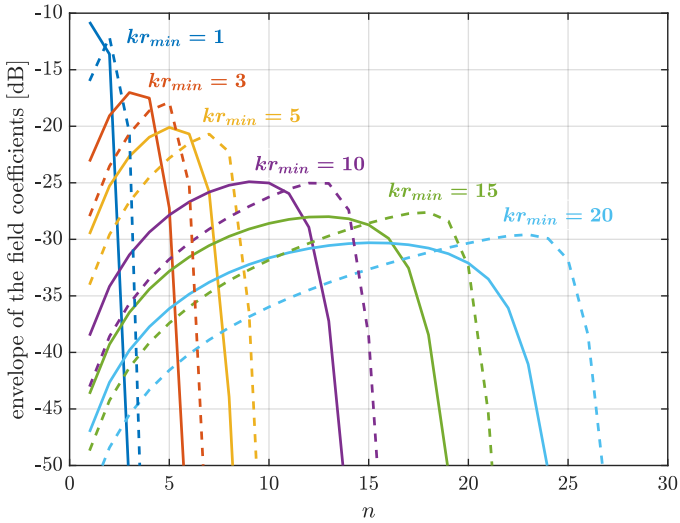

Figure 3.4: Envelope of the amplitude of the coefficients in (3.18) for various values of kr_{min} and two values of Q, namely $Q = 10$ (continuous line) and $Q = 100$ (dashed line).

3.3 Small Antennas: Dipolar and Quadrupolar Resonant Sources

The analysis presented above reveals a fundamental insight: spherical n-th harmonics, encompassing both TE and TM modes with azimuthal index $m = \pm 1$, share identical Q_n values and coefficients essential for achieving maximum directivity. This observation holds true for both Harrington's coefficients in (3.6) and the Q-bounded coefficients in (3.18).
Specifically, when $n = 1$, their fields, obtained with the same coefficients, can be considered as the ones produced from an elementary Huygens' dipole (HD) located at the origin, outside the minimum sphere (refer to Figure 3.5(a)). This HD configuration consists of horizontally aligned electric and magnetic dipoles, their momenta related by the free space impedance ζ, i.e., $I\Delta l = M\Delta l/\zeta$. Huygens' source antennas have found versatile applications, ranging from compact, electrically small packages [49–52, 54] to large ones [64] [65]. Their importance in research is underscored, especially for of Internet of Things (IoT) applications [66]. Furthermore, Huygens' metasurfaces have proven their efficacy in a variety of antenna and scattering problems [67] [68] [69].

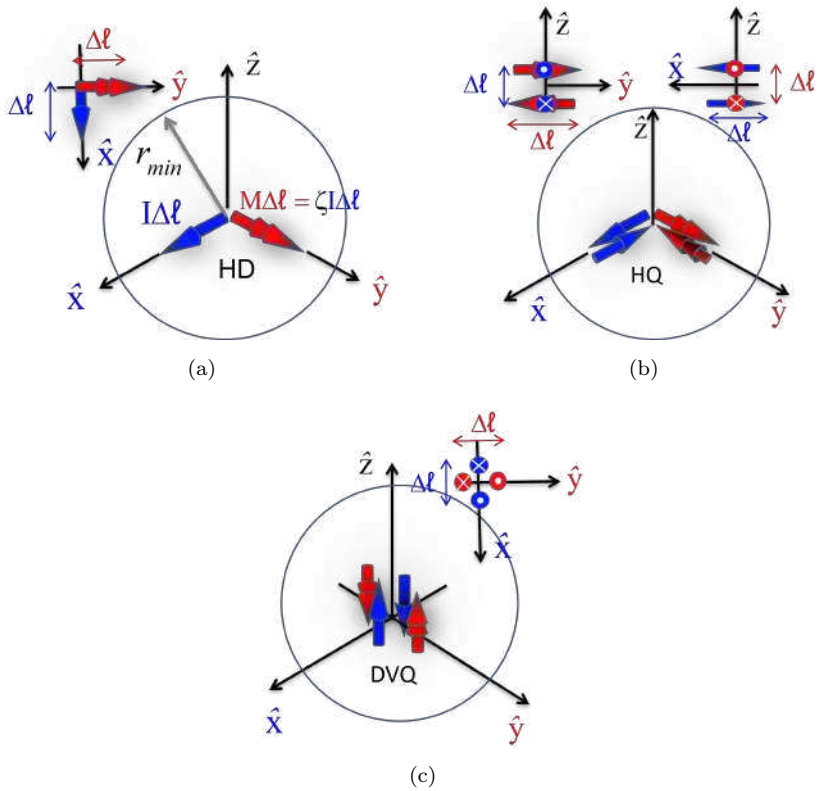

Figure 3.5: Graphical representation of a (a) Huygens' dipole (HD), (b) Huygens' Quadrupole (HQ) and (c) Vertical Dual Quadrupole (DVQ).

For $n = 2$, the combination of the second spherical wave harmonics gives rise to the field characteristics of a Huygens' Quadrupole (HQ) and a Dual Vertical Quadrupole (DVQ). These structures are illustrated in Figures 3.5(b) and (c), respectively. HQs have garnered recent attention, particularly in studies involving needle radiation from arrays [53]. The HQ configuration consists of pairs of counter-directed HDs, with their separation distances converging to infinitesimal values in terms of wavelengths. On the other hand, the DVQ configuration involves closely positioned counter-directed vertical magnetic and electric dipoles. The electric dipoles are displaced along the x-axis, while the magnetic dipoles are oriented along the y-axis. It is worth noting that the HD configuration maintains a balanced energy distribution outside the minimum sphere, precisely in line with the self-resonant approach. This balance is also observed in both HQ and DVQ configurations, a direct outcome of their duality.
The far-field radiation patterns of HD, HQ, and DVQ are given by

$$\boldsymbol{h}_{HD} = \frac{1}{2}(\cos\theta + 1)\hat{\boldsymbol{p}} \tag{3.19a}$$

$$\boldsymbol{h}_{HQ} = \frac{1}{2}(\cos\theta + 1)\cos\theta\hat{\boldsymbol{p}} \tag{3.19b}$$

$$\boldsymbol{h}_{DVQ} = \sin^2\theta\hat{\boldsymbol{p}} \tag{3.19c}$$

where $\hat{\boldsymbol{p}} = [\cos\phi - \sin\phi]\hat{\phi}$ is a unit polarization vector. We note that the coefficients associated with the maximum directivity to the spherical wave for $n = 2$ are linked the coefficients of HQ and DVQ each other, therefore combining it in

$$\boldsymbol{h}'_{HQ} = \boldsymbol{h}_{HQ} - \frac{1}{2}\boldsymbol{h}_{DVQ} = \frac{1}{2}(\cos\theta + \cos 2\theta)\hat{\boldsymbol{p}} \tag{3.20}$$

Hence, the far-field pattern $\boldsymbol{h}_{max}$ which provides the maximum directivity is provided by the combinations between $\boldsymbol{h}_{HD}$ and $\boldsymbol{h}'_{HQ}$ weighted by the corresponding coefficients. This provides the maximum directivity of 8, while the individual directivity of isolated $\boldsymbol{h}_{HD}$ and $\boldsymbol{h}_{HQ}$ are 3 and 7.5, respectively, as can be observed from Figure 3.6(a). The far-field polar pattern are depicted in Figure 3.6(b) for $\boldsymbol{h}_{HD}$, $\boldsymbol{h}_{HQ}$ and $\boldsymbol{h}_{max}$.

3.3.1 Minimum Q for Dipolar and Quadrupolar contributions

A lower limit can be determined for the minimum Q value, considering both the isolated effects of the Huygens' dipole and quadrupole, as well as the multipolar contribution.

Minimum Q for Isolated Huygens' dipole

The Q_1 in eq. (C.11) of Appendix C can be interpreted as the quality factors of *isolated* Huygens' Dipole, hence $Q \leq Q_1$ establishes a lower limit for the Q-factor, signifying an upper threshold for the maximum bandwidth of small antennas. This limitation corresponds to the well-known Chu-limit. However, in [25] Chu defined the limit for omni-directional antennas, focusing solely on the TM modes. This formulation yielded $Q \geq Q_{Chu}^{(TM)} \approx 1/(kr_{min})^3 + 1/(kr_{min})$. McLean [37] emphasized that the limit shifts when both TE and TM modes, especially in circular polarization, are taken into account. In such scenarios, the dominant quasi-static term is weighted by a factor of 2 in the denominator, leading to a revised expression. This modified limit corresponds to

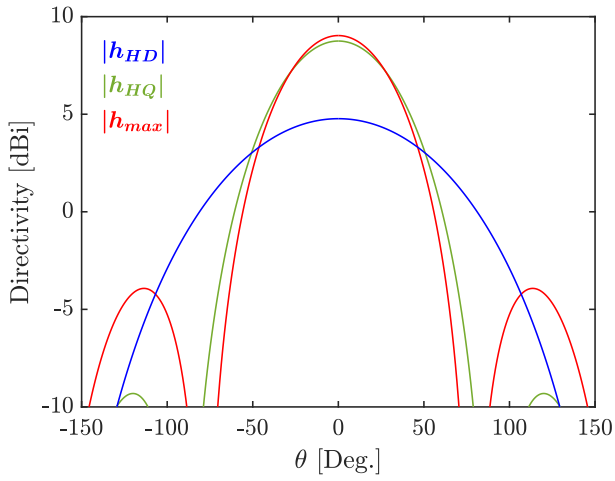

(a)

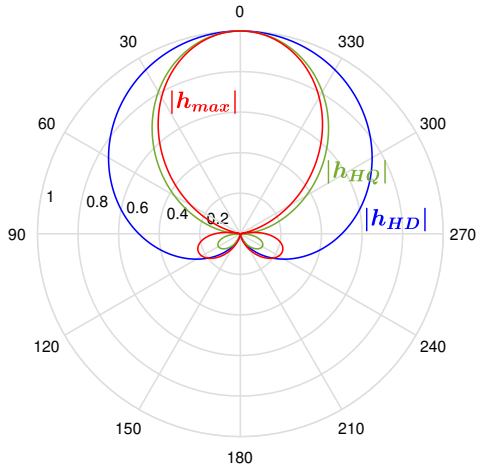

(b)

Figure 3.6: (a) normalized polar patterns and (b) 2D radiation patters of HD, HQ and combination of HD, HQ and DVQ for maximum directivity as in (3.15). h_{max} provides a maximum directivity of 8 (9.03 dBi), while the isolated h_{HD} and h_{HQ} provide a directivity of 3 (4.77 dBi) and 7.5 (8.75 dBi), respectively.

configurations featuring two vertical electric and magnetic dipoles, ensuring energy balance. It is worth noting that both authors, Chu and McLean, focused on antennas isotropic in the azimuthal plane rather than considering the scenario of maximum directivity. However, in cases of maximum directivity and self-resonant antennas, the current formulation naturally converges towards a configuration involving more than two vertical dipoles, specifically the Huygens' dipole, as it offers the highest directivity. Despite these considerations, we will continue

to refer to this scenario as the Chu-limit for clarity.

Minimum Q for Isolated Huygens' quadrupole

The Q_2 factor defined in eq. (C.12) of Appendix C can be understood as the quality factor of an *isolated* Huygens' Quadrupole. Upon examining (C.12), it becomes evident that the generalization to this concept in Appendix C implies that isolated Huygens' Quadrupoles adhere to $Q \geq Q_2$. This condition is considerably more restrictive than $Q \leq Q_1$, yielding a relative bandwidth of $0.11(kr_{\min})^5$ at low frequencies. However, it offers superior directivity (7.5 compared to 3). Optimal maximum directivity is achieved through a judicious combination of dipolar and quadrupolar contributions.

Minimum Q for the combination of Dipolar and Quadrupolar contributions for Maximum Directivity

The maximum directivity can be achieved through the combination of the contribution of both dipolar and quadrupolar. Hencem, let us combined the dipolar $\boldsymbol{h}_{HD}$ and quadrupolar $\boldsymbol{h}'_{HQ}$ contributions with arbitrary coefficients, i.e., $\boldsymbol{h} = \boldsymbol{h}_{HD} + \gamma \boldsymbol{h}'_{HQ}$ where the parameter γ is a real number. Applying the definition of directivity in (3.5), the directivity can be written as, $D = 2/\int_0^\pi |\boldsymbol{h}|^2/|\boldsymbol{h}_{max}|^2 \sin\theta \, d\theta$, which leads to

$$D = 3\frac{(1+\gamma)^2}{1+\frac{3}{5}\gamma^2} \tag{3.21}$$

To reach a maximum directivity of 8 the coefficient γ need to assume $\gamma = 5/3$. Hence, the associated minimum Q for the maximum directivity can be calculated using the expression in (C.8) of Appendix C truncating the series at the second terms and using the associated Harrington' coefficients for the maximum directivity in (3.6) leads to a

$$Q^{(2)} = \frac{3Q_1 + 5Q_2}{8} = \frac{45}{8(kr_{min})^5} + \frac{3}{(kr_{min})^3} + \frac{2}{(kr_{min})} \tag{3.22}$$

Therefore, $Q^{(2)}$ is the is the minimum quality factor that can be obtained with dipolar and quadrupolar contributions combined for maximum directivity. These findings lead to a higher maximum relative bandwidth at low frequencies compared to that of HQ alone. The data points corresponding to ($D_{max} = 8$) and ($D_{max} = 3$) are depicted in Figure 3.7 for various values of kr_{min}. These points are connected by straight dashed lines. Our solution in (3.15) is represented in the same Figure 3.7. The latter spans the range of directivity from 3 to 8 for any fixed Q, shown as continuous lines for comparison.

3.3.2 Combination of dipolar and quadrupolar contributions with Q-bound: closed-form approximation for small antennas

In the previous section, we explored the minimum Q problem without imposing any a-priori Q-bound. In the following discussion, we delve into this limit by examining scenarios involving only the contributions from dipolar and quadrupolar Huygens' sources, as well as considering the multipole contributions.

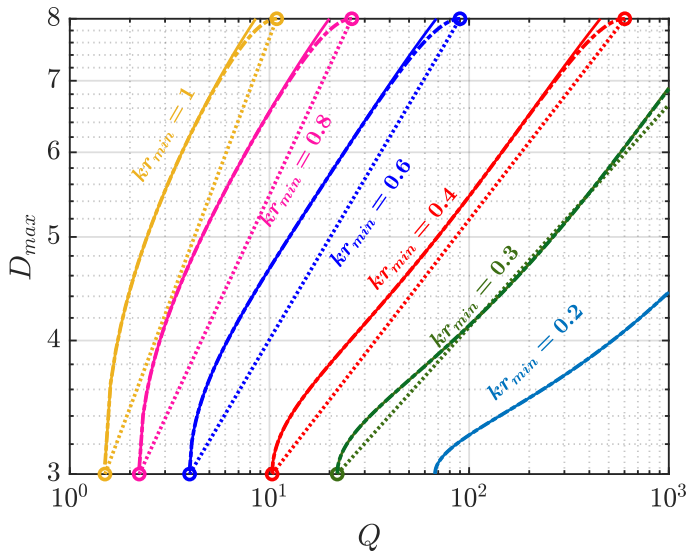

Figure 3.7: Dotted lines represent the maximum directivity as a function of the Q. Dots connected by dashed lines are obtained by ($D_{max} = 8$) and by ($D_{max} = 3$). Continuous lines are obtained through (3.15). Dash-dotted lines are obtained by using (3.23), namely setting Q constant for dipolar and quadrupolar contributions. The solution minimally deviates around with respect to eq. (3.15) since the latter include contribution of order 3 (hexapoles).

Referring to the maximum directivity with Q-bound and truncate the series in (3.15) at the first two terms leads to the combination $\boldsymbol{h}_{max} = \boldsymbol{h}_{HD} + \gamma \boldsymbol{h}'_{HQ}$, as well as the case without any Q-bound but with a different γ parameter. The resulting total Q in (C.8) of Appendix C, obtained with the corresponding Q-bounded maximum directivity coefficients in (3.18) is $Q = (Q_1 + \frac{3}{5}\gamma^2 Q_2)/(1 + \frac{3}{5}\gamma^2)$. Deriving γ from the latter leads to $\gamma = \sqrt{\frac{5(Q-Q_1)}{3(Q_2-Q)}}$ which substituted in (3.21) yields

$$D_{max} = 3\frac{\left(\sqrt{Q_2 - Q} + \sqrt{\frac{5}{3}(Q - Q_1)}\right)^2}{Q_2 - Q} \tag{3.23}$$

Consequently, the combination of dipolar and quadrupolar contributions that minimizes Q and maximizes directivity for any antenna size can be obtained substituting the $\gamma = \sqrt{\frac{5(Q-Q_1)}{3(Q_2-Q)}}$ into $\boldsymbol{h} = \boldsymbol{h}_{HD} + \gamma \boldsymbol{h}'_{HQ}$, whcih leads to

$$\boldsymbol{h}_{max} \approx \boldsymbol{h}_{HD} + \sqrt{\frac{5(Q - Q_1)}{3(Q_2 - Q)}}\boldsymbol{h}'_{HQ} \text{ for } Q_1 \leq Q \leq Q^{(2)} \tag{3.24}$$

From Figure 3.7 the excellent accuracy of (3.23) in the range $3 \leq D_{max} \leq 8$ is evident; the continuous lines are referred to the exact solution in (3.15) while the dash-dotted are referred to (3.23).
The equation in (3.23) holds for $Q_1 \leq Q \leq Q_2$, ensuring the existence of a real square root.

However, this result signifies the maximum achievable directivity within the Q-bound range of $Q_1 \leq Q \leq Q^{(2)}$, where at $Q^{(2)}$ the directivity reaches its peak value of 8, intersecting the Harrington point before decreasing (refer to Figure 3.7). This range of validity can be also expressed in terms of antenna size, inverting the relation in (C.11) and (C.12), namely

$$kr_1 \leq k_{min} \leq kr^{(2)} \approx 0.9kr_2 \tag{3.25}$$

where kr_1, kr_2, and $kr^{(2)}$ are the values for which $Q = Q_1$, $Q = Q_2$, and $Q = Q^{(2)}$, respectively. These values as a function of Q are obtained by inverting the expression of Q_1, Q_2, and $Q^{(2)}$, from (C.11), (C.12), and (3.22), respectively.

$$kr_1 \approx 0.4\left(\frac{1}{Q} + \frac{2}{Q^{1/3}}\right) \tag{3.26a}$$

$$kr_2 \approx 1.42\left(\frac{1}{Q} + \frac{1}{Q^{1/5}}\right) \tag{3.26b}$$

Comparison of the exact formula in (3.15) (continuous lines) with the two terms approximation

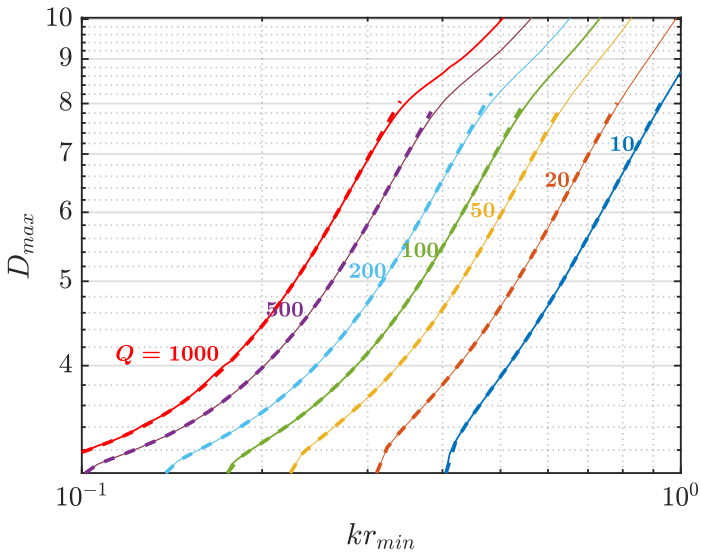

Figure 3.8: Bound of frequency bandwidth constrained super-Directivity (log-log scale) for different values of Q, truncated at the corresponding Chu-limit radius kr_1, where $D_{max} = 3$. Comparison between the exact formula (3.15) (continuous lines) and the approximate formula for small antennas in (3.23) (dashed lines). The validity range of the approximation is $kr_1 \leq kr_{min} \leq kr^{(2)}$.

in (3.23) (dashed lines) is shown in Figure 3.8 for several values of Q. The percentage relative error of (3.23) with respect to the full expansion, namely $\epsilon = (D_{max}^{(approx)} - D_{max})/D_{max}$, in the range $kr_1 \leq kr_{min} \leq 0.8kr_2$ is less than 1% for $100 \leq Q \leq 1000$ and less than 4% for $10 \leq Q \leq 100$, with maximum error always obtained close to $0.8kr_2$ (see Figure 3.9).

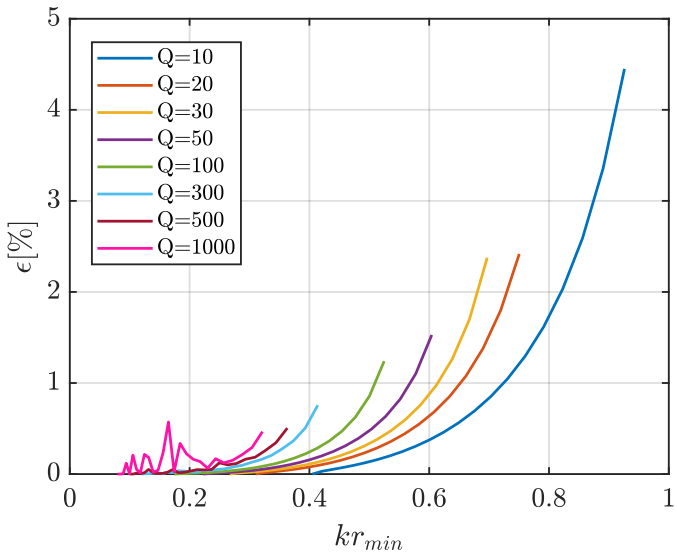

Figure 3.9: Percentage error between the approximation in (3.23) and the exact formula in (3.15) for $Q = 10, 20, 30, 50, 100, 300, 500, 1000$ in the range from $kr_1 \leq kr_{min} \leq 0.8kr_2$.

It is worth noting that the same outcome can be attained by truncating the series in (3.15), setting its derivative to zero, and solving the resulting second-order equation with the approximate ξ in (3.16), i.e.,

$$D_{max}(Q, kr_{max}) \approx \frac{3}{\bar{\xi}(Q_1 - Q) + 1} + \frac{5}{\bar{\xi}(Q_2 - Q) + 1} \tag{3.27}$$

3.3.3 Multipole contributions without and with Q-bounds

Figure 3.10 shows the maximum directivity as a function of Q for various values of kr_{min} associated to a finite numbers N_{max} of multipoles. To this end the expression $D_{max} = N_{max}^2 + 2N_{max}$ is evaluated as a function of the total quality factor in (C.8) in Appendix C, using the Harrington coefficients in (3.6), i.e., $Q = \sum_{n=1}^{N_{max}} Q_n(2n+1)/(N_{max}^2 + 2N_{max})$. The Fante's Q_n has been used in the calculation in Appendix (C). This plots can be obtained only by a discrete points since N_{max} can assume only integer values. These points are connected by straight line in Figure 3.10. The continuous curve is obtained by the exact formula (3.15). It is seen that the discrete points are reasonably close to the continuous curve obtained by (3.15), and always below the continuous curve.

3.4 Closed-form formulas for larger antennas

From Figure 3.2, it can be observed that the value of $\bar{\xi}$ exhibits smooth variation for $kr_{min} \leq kr_2$; for this reason by adopting the value of $\bar{\xi}$ at $0.6kr_2$ and maintaining it throughout the range $0.6kr_2 \leq kr_{min} \leq 10$, an accurate solution for directivity is obtained. This value of $\bar{\xi}$ is directly

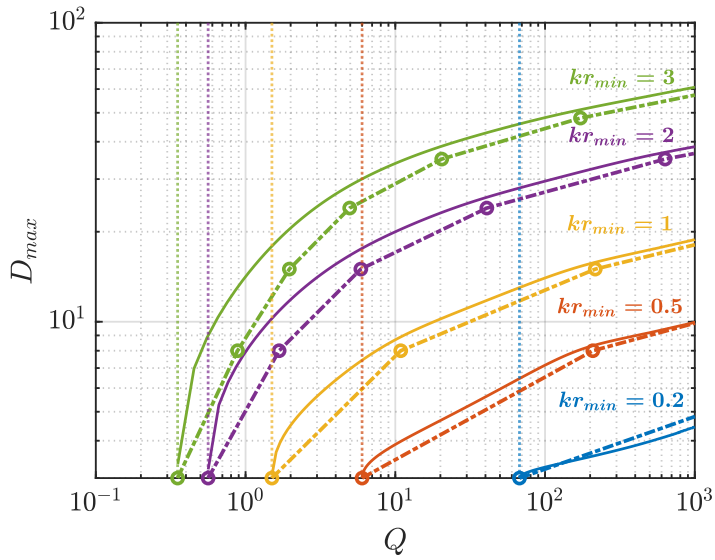

Figure 3.10: Maximum directivity of a finite number of multipoles as a function of Q (dots connected by dashed lines) and as a function of Q derived (dashed lines) for $kr_{min} = 0.2, 0.5, 1, 2, 3$. The results are compared with the results obtained from (3.15). The vertical dotted lines correspond to the Chu-limit $Q = Q_1$.

derived from (3.26b) and yields $\bar{\xi} \approx 0.16/Q$. Utilizing this value of $\bar{\xi}$ leads to the following concise closed form

$$D_{max}(Q, kr_{min}) \approx \sum_{n=1}^{\infty} \frac{2n+1}{0.16\left(\frac{Q_n}{Q} - 1\right) + 1} \tag{3.28}$$

We observe that the summation can be truncated at $[kr_{min}] + 10$ without compromising the accuracy. Comparison between the exact form in (3.15), and the combination between (3.23) and (3.28) is given in Figure 3.11. It is seen that this formula is accurate for $kr^{(2)} \leq kr_{min} \leq 20$ and $10 < Q < 5000$.

It is seen that this formula is accurate for $0.8kr2 \leq kr_{min} \leq 20$ and $10 < Q < 5000$. In particular, the percentage error $\epsilon[\%] = (D_{max}^{(approx)} - D_{max})/D_{max}$ in the above range for various values of Q is presented in Figure 3.12. It can be seen that the percentage error is less than 5% for $Q < 100$ and less than 7% for $Q < 1000$.

A less accurate, but simpler formula (since it does not require the calculation of Q_n) is obtained on the basis of an approximation (3.17) and is given by

$$D_{max}(Q, kr_{min}) \approx \sum_{n=1}^{\infty} \frac{2n+1}{0.16\left[\frac{1}{Q}\left(\frac{n}{1.2(kr_{min})}\right)^{(2n+1)} - 1\right] + 1} \tag{3.29}$$

This formula is accurate enough for $kr^{(2)} \leq kr_{min} \leq 3$ as can be observed from Figure 3.13.

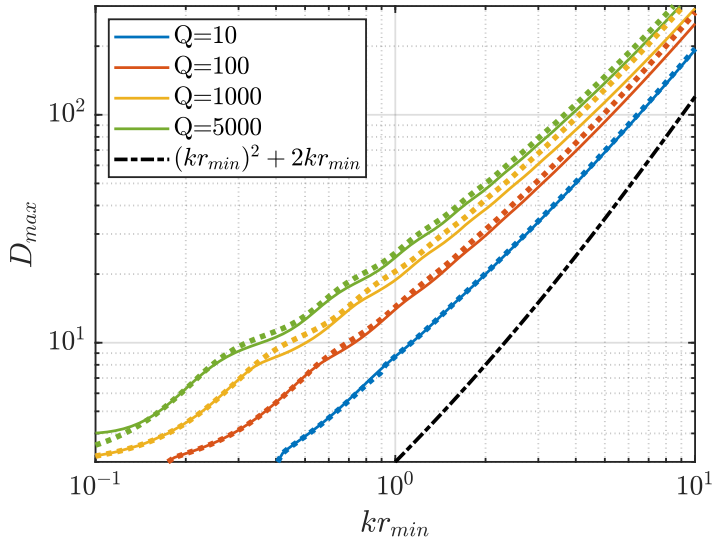

Figure 3.11: Maximum directivity (log-log scale) for constant Q. The curves are truncated at the corresponding Chu-limit radius, where $D_{max}(Q, kr_{min}) = 3$. Comparisons of the exact formula (3.15) (continuous line) and the combination between (3.23) and (3.28) (dotted lines) for $Q = 10, 100, 1000, 5000$.

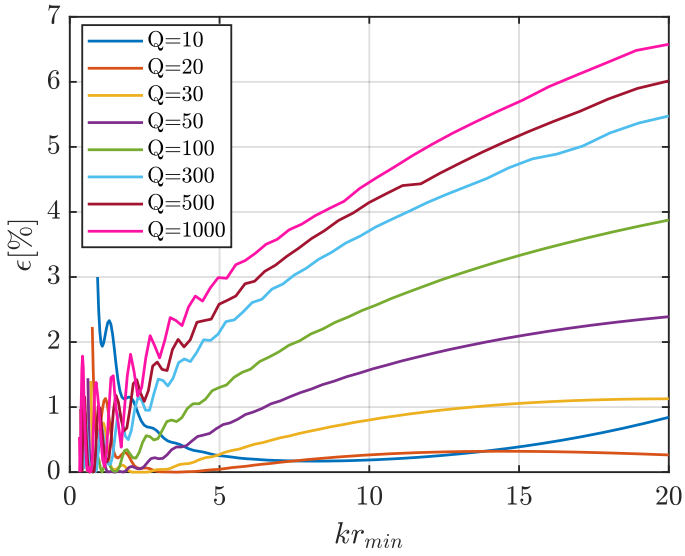

Figure 3.12: Percentage error between the approximation in (3.28) and the exact formula in (3.15) for $Q = 10, 20, 30, 50, 100, 300, 500, 1000$ in the range from $0.8kr2 \leq kr_{min} \leq 20$.

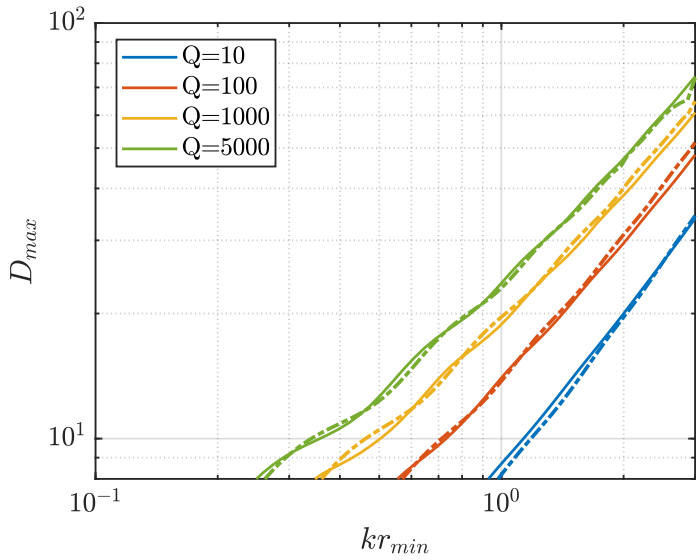

Figure 3.13: Bound of Super-Directivity (log-log scale) truncated at the corresponding Chu-limit radius kr_1. Comparisons of the exact formula (3.15) (continuous lines) and the combination between (3.23) and (3.28) (dash-dotted lines) for $Q = 10, 100, 1000, 5000$.

3.5 Maximum Directivity and Equivalent Radius for constant Q

The effectiveness of the presented formulation is more clear when the results are presented in terms of equivalent area. This is because the equivalent area provides a more tangible measure for understanding the impact of the bandwidth bound in the maximum directivity. Hence, this formulation provide also an optimization in terms of area. Yaghjian [70] presented simplified formulas for sampling the minimum sphere. He distinguished non-resonant antennas from resonant antennas and provided a link between the equivalent radius associated with the storage of reactive energy and maximum equivalent area of the antenna, therefore establishing a link with the maximum directivity. The maximum directivity can be described in terms of equivalent radius, i.e., by $D_{max} = (kr_{eq})^2$. The r_{eq} may be interpreted as the equivalent radius at which the reactive field becomes negligible [70]. Figure 3.14 compares the results for different values of Q with the ones obtained from the directivity estimated by Harrington.

3.6 Conclusions

In the previous section, we established an analytical closed-form formula for the Q-bounded maximum directivity (3.15). The expression has been obtained by solving a convex optimization problem formulated in terms of an SW expansion of the radiated field, and it is expressed in the form of a series that converges rapidly in a large range of the parameters' variation. The main achievements connected with this expression are summarized here.

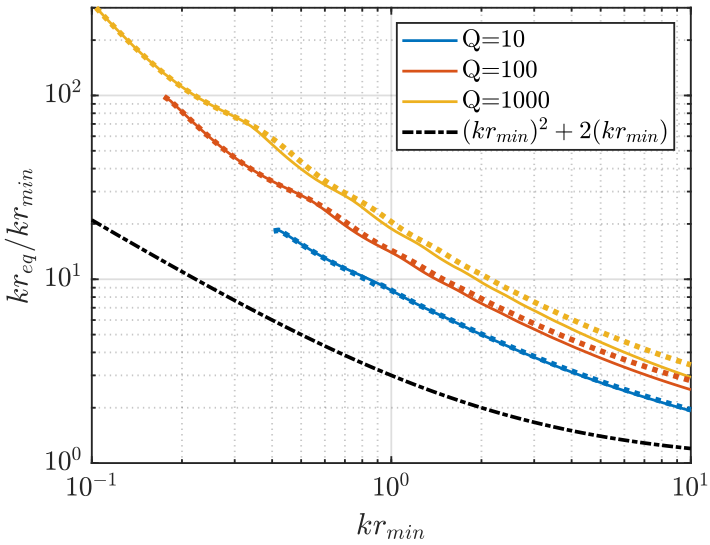

Figure 3.14: Ratio between r_{eq} and r_{min} as a function of kr_{min} for different values of Q, the curves are truncated at radius corresponding to the Chu-limit. The equivalent radius is obtained from the exact formula in (3.15) (continuous lines) and the combination between the approximate ones in (3.23) and (3.28) (dotted lines). The back dash-dotted line is obtained with the Harrington formula, i.e., $(kr_{min})^2 + 2(kr_{min})$.

1. The coefficients of the SW expansion providing the maximum directivity are given in analytical form, thus allowing for the derivation of the optimal radiation pattern for any radius of the minimum sphere;

2. The maximum directivity limit goes to 3 for the values of kr_{min} that respect the Chu-limit for dipolar Huygens' sources. In this case, the exact formula predicts maximum directivity equal to 3 independently of the value of Q

3. For small antennas, the results are interpreted in terms of a combination of the field radiated by dipolar and quadrupolar Huygens' sources outside the minimum sphere. This interpretation leads to the simple formula (3.23) which provides an accurate continuous description of directivity in the range $3 \leq D_{max} \leq 8$ as a function of the minimum Q for any fixed antenna size as an intermediate step of the solution for small-size antennas, we have also found the relation $Q > Q_2$ that established the limit of bandwidth for HQs alone, which is an extension of the Chu-limit to isolated resonant quadrupoles;

4. By using the exact formula, a simple analytical closed-form expression has been derived, which complements the expression in the quadrupole range for electrical size till $kr_{min} = 20$ and $Q < 5000$.

It is important to stress that being the limit obtained with zero field inside the minimum sphere, this limit could be very difficult to approach for large antenna sizes. For small- to-intermediate

size antennas, the simplicity of the final formulas together with their interpretation renders this work useful for antenna engineers. The extension of this work to account for losses will be carried out in a dedicated article.

Chapter 4

Bounds on Super-Gain

4.1 Introduction

In the previous chapter (Chapter 3), the study focused on determining the upper limit of super-directivity for self-resonant antennas with a minimum Q. It's important to note that super-directivity and super-gain are not the same; the latter takes losses into account. In this Chapter, we establish an upper bound on the maximum gain achievable for any type of antenna. To achieve this, a numerical approach has been implemented considering a pair of electric orthogonal dipole located over a spherical surface. By expanding the fields using spherical waves and applying the equivalence theorem, analytical formulas for the maximum gain has been calculated with and without of bandwidth constraint.

4.2 Antenna Gain

Antenna gain refers to the ability of an antenna to concentrate its radiated energy in a specific direction. It's used in both transmitting and receiving contexts, means that in a transmitting antenna, the gain describes how well the antenna converts the input power into waves oriented in a specified direction, reversely in a receiving antenna, it characterizes how well the antenna converts the waves coming from a specified direction into electrical power. The antenna gain is defined by the product between the radiation efficiency η and the directivity D

$$G = \eta D \tag{4.1}$$

Knowing that the directivity is the ratio between the radiation intensity in the direction of its strongest intensity and the power total radiated power, namely $D(\theta, \phi) = 4\pi U(\theta, \phi)/P_r$, therefore, the gain can be expressed as

$$G(\theta, \phi) = 4\pi \frac{U(\theta, \phi)}{P_r + P_\Omega} \tag{4.2}$$

where $U(\theta, \phi)$ is the radiation intensity, P_r is the radiated power, and P_Ω is the power dissipated due to losses.
As for the directivity, we can write the gain as a function of the antenna effective area A_{eff}, an alternative quantity used to describe the directive properties of reciprocal antennas

$$G = 4\pi \frac{A_{eff}}{\lambda^2} \tag{4.3}$$

It is important to note that the effective area is a theoretical concept and can be used to compare antennas in terms of their performance characteristics, but it does not necessarily represent a physical area of the antenna.

4.3 Maximum Super-Gain Without Q-Bounds

In this Section the determination maximum super-gain is done expanding the electric and the magnetic fields in terms of spherical waves (see Appendix A). The Love formulation of the equivalence theorem is first applied to the minimum spherical surface which includes all the sources. The equivalent electric and magnetic currents radiate zero field inside the surface. The external field is the same as that provided by magnetic currents radiating on a perfectly conducting sphere of radius r_{min}, as predicted by the Schelkunoff formulation. In Section B.1 of Appendix B, the equivalent currents derivation is presented. For instance, we assume that the magnetic currents radiate in presence of a lossy conductor with resistivity for square-surface R_Ω. This resistance, also known as sheet resistance, has a value that depends on $\sqrt{f}$, for copper it is approximately $R_\Omega = 2.82 \times 10^{-7}\sqrt{f}\omega$). We assume that the electric currents induced on the conductor by the magnetic forced currents will not change significantly wrt the currents on a PEC. Since the resulting fields inside the minimum sphere S is zero, the total stored energy is zero. However, considering only the contribution of the electric currents radiating alone in free space (see Section B.2 of Appendix B) leads to a different expression of radiation resistance as well as a non-zero value of the energy stored inside to the surface. This aspect will be investigated further.
Referring to Appendix B, we obtain the expression for the radiation resistance (eq. B.16) of the individual harmonics in the case of a lossy conducting sphere. This expression can also be explicitly derived using the spherical Hankel's function of the second type $h_n^{(2)}(kr_{min})$, i.e.,

$$R_{rad,n}^{(s)} = \begin{cases} \zeta \left| \frac{d}{d(kr)} kr_{min} h_n^{(2)}(kr_{min}) \right|^{-2} & \text{for } s = 1 \text{ (TE)} \\ \zeta (kr_{min})^{-2} \left| h_n^{(2)}(kr_{min}) \right|^{-2} & \text{for } s = 2 \text{ (TM)} \end{cases} \tag{4.4}$$

Note that these values has a weak dependence on kr_{min} for $n > kr_{min}$ and goes to ζ for $kr_{min} >> n$. The value of the radiation resistance for $n = 1, 2, 3, 4$ is shown in Figure 4.1. It is seen that for small values of n, $R_{rad,1}^{(2)}$ and $R_{rad,2}^{(2)}$ (TM) go to zero as $(kr_{min})^2$ and $(kr_{min})^4$, respectively; while $R_{rad,1}^{(1)}$ and $R_{rad,2}^{(1)}$ (TE) go to zero as $(kr_{min})^4$ and $(kr_{min})^6$, respectively.

4.3.1 Maximum Gain for Externally Tuned Antennas

Although in the definition of the radiated power, namely $P_r = \frac{1}{2}\sum_i R_{rad,n}^{(s)} |I_i|^2$, only involves the electric current coefficients I_i, it represents the *total* power radiated by *both* the equivalent electric and magnetic currents radiating *together* in free-space or, equivalently, the power radiated by the magnetic currents alone on top of a metallic sphere, that induces electric currents on the metallic sphere (see Appendix B). The total power $P_r + P_\Omega$ (radiated plus dissipated power) is given by

$$P_r + P_\Omega = \frac{1}{2} \sum_i \left(R_{rad,n}^{(s)} + R_\Omega \right) \left| I_i \right|^2 \tag{4.5}$$

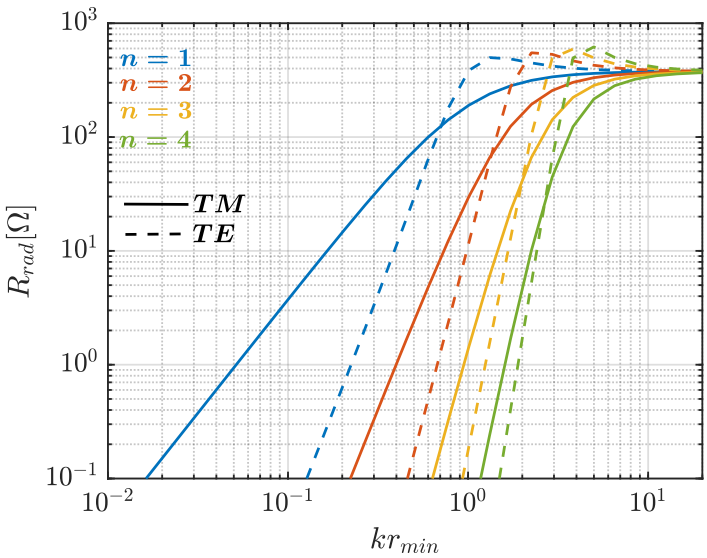

Figure 4.1: Radiation resistance of individual harmonics for $n = 1, 2, 3, 4$ as a function of the minimum surface normalized radius for TM (continuous lines) and TE (dashed lines) modes.

We observe that, since the symmetry of the problem, the maximization of the gain can be done in an arbitrary observation direction and with an arbitrary polarization. It is therefore not restrictive to assume $(\theta, \phi) = (0, 0)$ as well as a $\hat{\theta}$-polarization. The power density in direction $(\theta, \phi) = (0, 0)$ (broadside direction) is obtained by using the far zone limit approximation. This can be written as $U = \lim_{r\to\infty} \frac{1}{2\zeta}|r\boldsymbol{E}|^2 = \frac{1}{8\pi}|\sum_i C_i \boldsymbol{K}_i|^2$, whit $\boldsymbol{K}_i = 4\pi \boldsymbol{T}_i \lim_{r\to\infty} kr R^{(3)}_{3-s,n}$. The same quantity can be expressed in terms of the electric currents coefficients I_i through $|C_i| = |I_i|\sqrt{R^{(s)}_{rad,n}}$; therefore, from the definition in (4.2) the antenna gain in direction (θ, ϕ) is given by

$$G(\theta, \phi) = \frac{\left|\sum_i \sqrt{R^{(s)}_{rad,n}} I_i \boldsymbol{K}_i(\theta, \phi)\right|^2}{\sum_i \left(R_{rad,i} + R_\Omega\right)|I_i|^2} \tag{4.6}$$

under the assumption that the modal currents on the surface are not perturbed by the presence of the small losses.
Starting from equation in (4.6), we followed the method applied by Harrington in [28] to maximize the directivity, without imposing an a-priori truncation on the harmonics, which was necessary in the Harrington's process to get a finite result. Applying the Swartz identity to the numerator of (4.6), yields to

$$G \leq \frac{\left(\sum_i \sqrt{R_{rad,i}}|I_i||K_i|\right)^2}{\sum_i \left(R_{rad,i} + R_\Omega\right)|I_i|^2} \doteq G_0(|I_i|) \tag{4.7}$$

The equality symbol in (4.7) is valid when $\angle K_i = -\angle I_i^*$. The maximization of the function in (4.7) is obtained by imposing the vanishment of the derivative wrt $|I_i|$; namely

$$\frac{\partial G_0}{\partial |I_i|} = \frac{\partial}{\partial |I_i|} \frac{\left(\sum_i \sqrt{R_{rad,i}} |I_i| |K_i| \right)^2}{\sum_i \left(R_{rad,i} + R_\Omega \right) |I_i|^2} = 0 \tag{4.8}$$

The above (4.8) is equivalent to

$$\begin{aligned} &\left(2|K_q| \sqrt{R_{rad,q}} \right) \sum_i \left(R_{rad,i} + R_\Omega \right) \big| I_i \big|^2 = \\ &= 2 \big| I_q \big| \left(R_{rad,i} + R_\Omega \right) \left(\sum_i \sqrt{R_{rad,i}} \big| I_i \big| \big| K_i \big| \right) \end{aligned} \tag{4.9}$$

which is respected if and only if

$$\big| K_q \big| \sqrt{R_{rad,i}} = \big| I_q \big| \left(R_{rad,q} + R_\Omega \right) \tag{4.10}$$

for any couple of indexes i, q. Substituting (4.10) in (4.7) leads to the following analytic closed-form formula for the maximum gain

$$G_{max} = \frac{1}{2} \sum_{n=1}^{\infty} \left\{ (2n+1)(\eta_n^{(TE)} + \eta_n^{(TM)}) \right\} \tag{4.11}$$

with

$$\eta_n^{(TE,TM)} = \frac{1}{1 + R_\Omega / R_{rad,n}^{(1,2)}} \tag{4.12}$$

where $\eta_n^{(TE)}$ and $\eta_n^{(TM)}$ correspond to the radiation efficiency associated to TE and TM individual modes, respectively.
The electric field coefficients (with Hansen's normalization) are given by

$$C_i = \delta_i \eta_n^{(TE,TM)} \sqrt{2n+1} \tag{4.13}$$

where

$$\delta_i = I_0 \sqrt{\zeta} \begin{cases} 0 & \text{if } |m| \neq 1 \\ (-j)^n & \text{if } s = 1, m = \pm 1 \\ m(-j)^n & \text{if } s = 2, m = \pm 1 \end{cases} \tag{4.14}$$

The constant I_0 is arbitrary (it disappears in calculating G_{max}) and can be set up in such a way to have the same radiated power for any R_Ω. The total radiation efficiency $\eta = \frac{P_r}{P_r + P_\Omega}$ in condition of maximum gain is indeed given by

$$\eta = \frac{\sum_i R_{rad,n}^{(s)} \frac{|I_i|^2}{|I_0|^2}}{\sum_i \left(R_{rad,n}^{(s)} + R_\Omega \right) \frac{|I_i|^2}{|I_0|^2}} = \frac{\sum_n (2n+1) \left[\left(\eta_n^{(TE)} \right)^2 + \left(\eta_n^{(TM)} \right)^2 \right]}{\sum_n (2n+1) \left[\eta_n^{(TE)} + \eta_n^{(TM)} \right]} \tag{4.15}$$

The efficiency in (4.15) is shown in Figure 4.2 for different values of the loss resistance R_Ω.

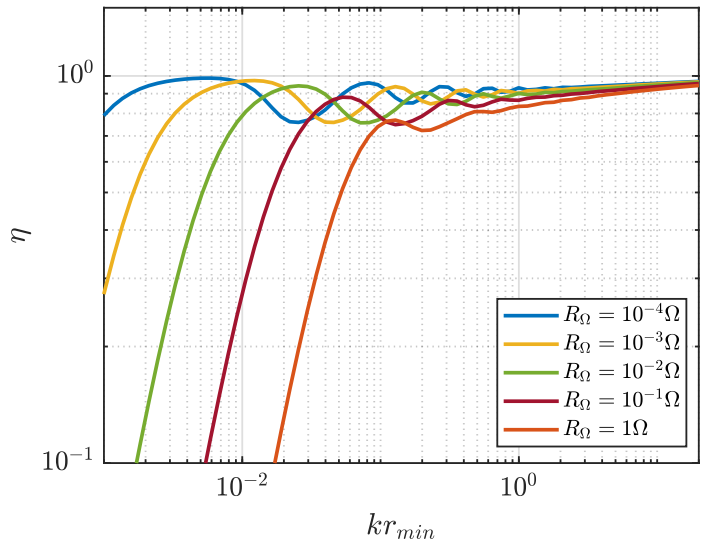

Figure 4.2: Efficiency of the super-gain calculated for different values of R_Ω as a function of kr_{min}.

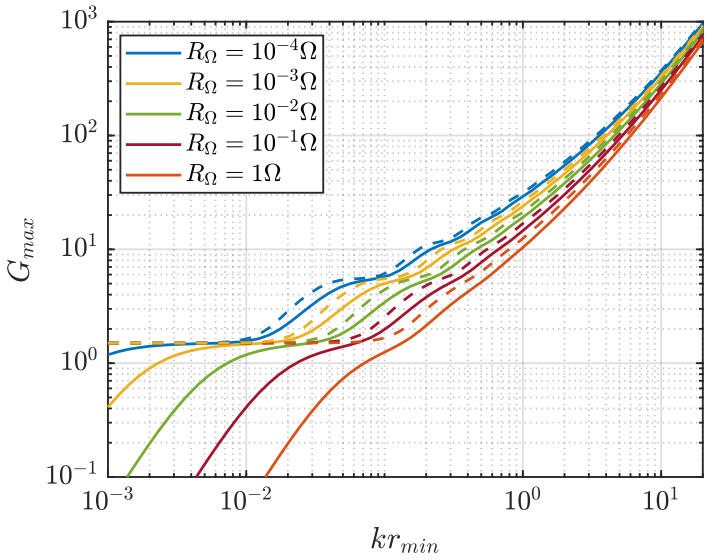

Figure 4.3: Maximum gain of externally tuned antennas calculated for different values of R_Ω as function of kr_{min} (continuous lines) and corresponding directivity (dashed lines) obtained by G_{max}/η.

Figure 4.3 shows the values of maximum gain obtained implementing (4.11) for various values of the surface resistance R_Ω (continuous lines). It also shows the directivity (dashed lines)

obtained dividing the maximum gain in (4.11) for the efficiency in (4.15). From Figure 4.3 can be observed that the super-gain and the corresponding directivity show inflection points at the maximum of the radiation efficiency. The lower frequency inflection point occurs at $G_{max} = 1.5$. For smaller value of electrical radius wrt the one of the first inflection point the directivity saturate to 1.5. Decreasing the minimum sphere radius, the directivity obtained by the current coefficients is close to the maximum gain till a value of 1.5 and next remains equal to 1.5 till zero dimension of the minimum sphere. It is worth noting that this flat level is 1.5, which corresponds to the directivity of an electric dipole and not 3 (Huygens' source directivity), which, on the contrary, was the case for directivity (see Chapter 3). The phenomenon discussed was previously highlighted in Gustafsson's work [1]. It is primarily attributed to the elevated radiation resistance exhibited by the first TM dipolar mode (electric dipole) when the radius of the minimum sphere is extremely small. Conversely, the radiation resistance of the first TE mode is significantly lower, making it more susceptible to losses. It's also important to note that the additional inflection points of the super-gain are due to the fact that one more mode becomes significantly excited in the summation in eq. (4.11).

4.3.2 Maximum Gain for Self-Resonant Antennas

The solution presented in (4.11) is not self-resonant; this implies that an additional external reactive tuning circuit is needed to achieve the maximum gain possible. The maximum gain can be obtained through a convex optimization, which relies on the principles of the Lagrange dual problem, following a similar procedure used for the maximization of the directivity for a fixed Q in Chapter 3. We won't repeat the entire procedure here, but the final result is provided below

$$G_{max} = \min_{\xi \in [\xi^{(TE)}, \xi^{(TM)}]} \sum_{n=1}^{\infty} \frac{1}{2} \left(\frac{\eta_n^{(TE)}(2n+1)}{1 + \xi \eta_n^{(TE)}(Q'_n - Q''_n)} + \frac{\eta_n^{(TM)}(2n+1)}{1 - \xi \eta_n^{(TM)}(Q'_n - Q''_n)} \right) \tag{4.16}$$

with

$$\xi^{(TE)} = -\frac{1}{\max_n \{\eta^{(TE)}(Q'_n - Q''_n)\}} \tag{4.17a}$$

$$\xi^{(TM)} = \frac{1}{\min_n \{\eta^{(TM)}(Q'_n - Q''_n)\}} \tag{4.17b}$$

where Q'_n and Q''_n are the dominant and subdominant quality factors reported in Appendix C. The gain in (4.16) is obtained with field coefficients

$$C_i = \delta_i \frac{\eta_n^{(TE,TM)} \sqrt{2n+1}}{1 + \xi_0 \eta_n^{(TM)}(Q'_n - Q''_n)} \tag{4.18}$$

where ξ_0 is the value that minimize the series and δ_i is defined in (4.14).
Comparison between the externally tuned gain antennas and self-resonant gain antennas, expressed with eq. (4.11) and eq. (4.16), respectively, is given in Figure 4.4. The resonant antenna maximum gain is tighter wrt the one for externally tuned antenna, especially for small antennas, and drop rapidly to zero for gain approximately equal to 3. This aspect has been also underlined in [1].

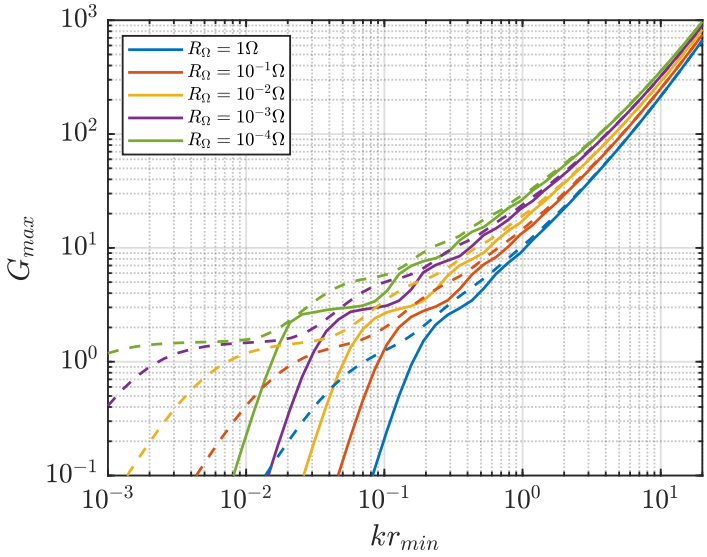

Figure 4.4: Maximum gain calculated for different values of R_Ω as a function of kr_{min} for tuned antennas (dashed lines) and self-resonant antennas (continuous lines).

4.3.3 Comparison with Gustafson-Capek results

It is important to compare the results with the ones obtained by Gustafsson and Capek in [1]. The approach presented there is based on Methods of Moments (MoM) applied to the surface of an arbitrary metallic body and by a convex optimization procedure. Their investigation led to maximum super-gain through the imposition of power intensity maximization while maintaining a constant radiated power for all coefficients of the MoM basis functions. This procedure is quite general and can be applied to arbitrary shape. In Fig. 1 of [1], the authors demonstrated the application of this methodology to a spherical shape, utilizing spherical modes as basis functions. In externally tuned case, the convex optimization is carried out without condition on the reactance of the MoM matrix; while in the self-resonant case, they impose a vanishing reactive average power through the imaginary part of the MoM matrix. Here, the formulation has been re-implemented using the convex optimization procedure of Gustafsson-Capek for both cases, obtaining a very similar results provided by (4.11) with the radiation resistance in (4.4). Figure 4.5 shows the difference between our results and the one in [1] for the externally-tuned case (similar discrepancy is found for the self-resonant case). We discover that the motivation of this discrepancy resides in the different definition of the original formulation problem and as consequence of the radiation resistance. Indeed, it is seen eventually that the results from our procedure become identical to those obtained in [1] if one uses the radiation resistance produced by electric current only, which derivation is reported in Appendix B. In other terms, we can reproduce exactly the results in [1] changing the SW radiation resistances in 4.4 with the one in (B.9) in Appendix B that can be expressed explicitly with the spherical Bessel's function

$j_n(kr_{min})$, i.e.,

$$R^{(s)}_{rad,n,J-only} = \begin{cases} \zeta\left[\frac{d}{d(kr)} kr_{min} j_n(kr_{min})\right]^2 & \text{for } s = 1 \text{ (TE)} \\ \zeta\left[kr_{min} j_n(kr_{min})\right]^2 & \text{for } s = 2 \text{ (TM)} \end{cases} \tag{4.19}$$

These radiation resistances are the one corresponding to harmonics of electric currents only

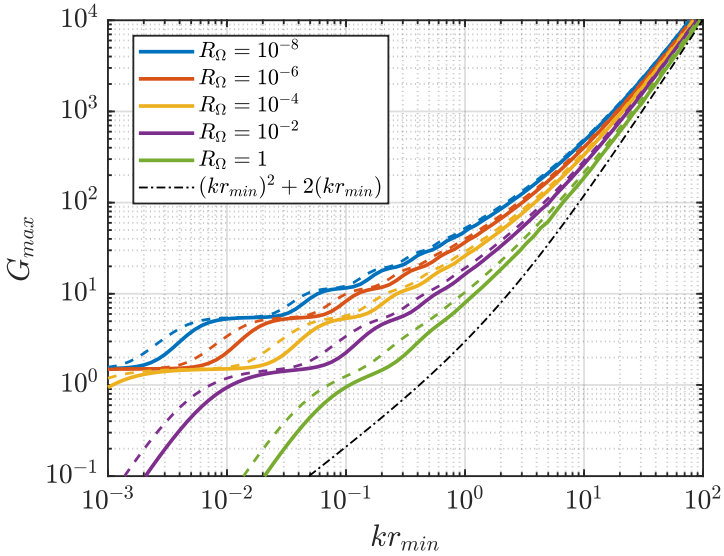

Figure 4.5: Comparison between the maximum gain for the externally tuned case of our formulation (continuous lines) and the formulation in [1] (dashed lines), also obtained by using (4.19) in (4.11). The dash-dotted black line represent the Harrington limit, i.e., $(kr_{min})^2 + 2(kr_{min})$.

radiating in free-space. It should be noted that using the electric currents only, provides field and energy different from zero inside the minimum sphere as explained also in Appendix B, therefore, the use of (4.4) leads to a bit lower value of the maximum gain wrt to the gain with (4.19).

4.3.4 Distribution of the currents coefficients

The coefficients for the currents expansion are obtained dividing by the square root of the individual TE and TM individual n-indexed radiation resistance, namely

$$I_i = I_0\sqrt{2n+1} \begin{cases} 0 & \text{if } |m| \neq 1 \\ -(j)^n \frac{\sqrt{\zeta R^{(1)}_{rad,n}}}{R^{(1)}_{rad,n}+R_\Omega} & \text{if } s = 1, m = \pm 1 \\ -m(j)^n \frac{\sqrt{\zeta R^{(2)}_{rad,n}}}{R^{(2)}_{rad,n}+R_\Omega} & \text{if } s = 2, m = \pm 1 \end{cases} \tag{4.20}$$

where constant I_0 is arbitrary (it disappears in calculating G_{max}) and can be set up in such a way to have the same radiated power for any R_Ω, i.e.,

$$I_0 = \sqrt{\frac{2P_r}{\sum_i R^{(s)}_{rad,i}|I_i|^2/|I_0|^2}} \tag{4.21}$$

Figure 4.6 and 4.7 shows the histogram of the n-indexed current coefficients' amplitude in

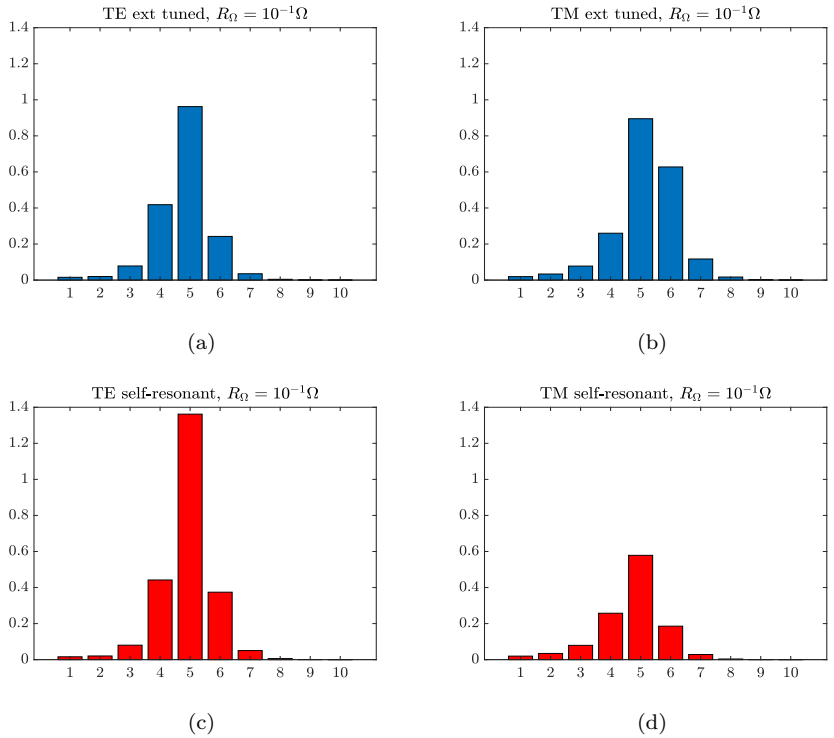

Figure 4.6: Histograms of current coefficients for TE (inductive, right-hand side) and TM (capacitive, left-hand side) harmonics with $R_\Omega = 10^{-1}\Omega$. (a)-(b) for externally tuned case, and (c)-(d) for self-resonant case.

(4.20) corresponding to the maximum gain, for $R_\Omega = 10^{-1}\Omega$ and $R_\Omega = 1\Omega$ and for $kr_{min} = 2$. Both cases of externally tuned coefficients and self-resonant coefficients are reported. It is seen that for smaller values of the loss resistance the optimal current coefficients concentration is pertinent to super-reactive SWs (it means SWs with polar index much larger than $kr_{min} = 2$). The amplitudes are normalized to have a unit radiated power ($P_r = 1W$). The maximum coefficients are obtained for the n where the harmonics efficiency is about 50%. It is apparent that for smaller values of the loss-resistance the optimal current coefficients are concentrated on super-reactive harmonics, it means SWs with polar index larger than $kr_{min} = 2$. This makes it challenging to achieve their excitation on the minimum sphere. It is also apparent from Figure 4.6 and Figure 4.7 that the TE optimal coefficients for the resonant case are higher, aligning with their reduced efficiency for small antennas. Furthermore, lower losses correspond to larger

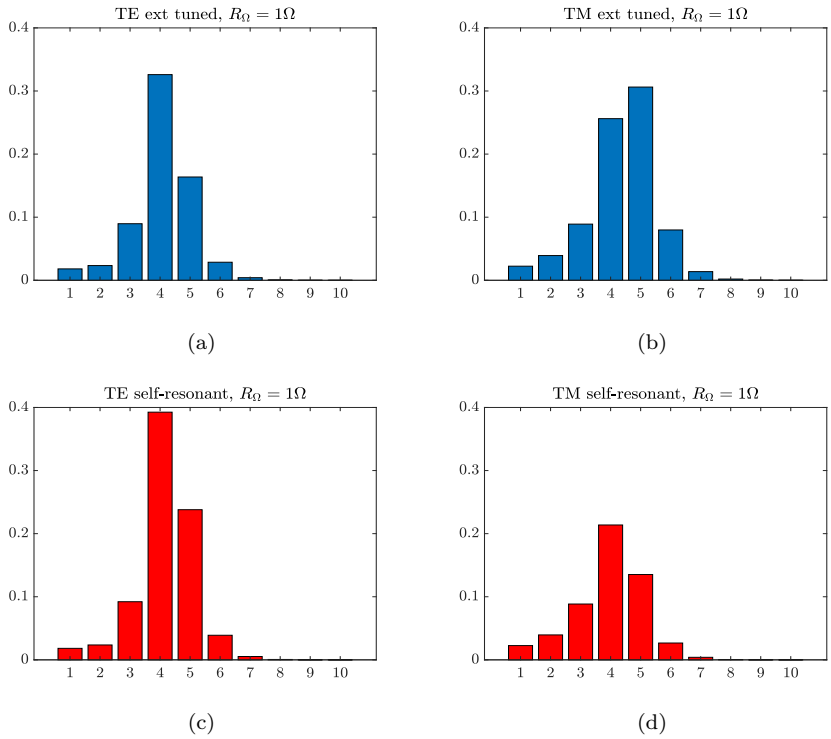

Figure 4.7: Histograms of current coefficients for TE (inductive, right-hand side) and TM (capacitive, left-hand side) harmonics with $R_\Omega = 1\Omega$. (a)-(b) for externally tuned case, and (c)-(d) for self-resonant case.

optimal coefficient values, as noted by the disparity in the vertical scales between Figure 4.6 and 4.7.

From Figure 4.8 is more clear that the maximum coefficient amplitude, is given at the values in which the ohmic losses resistance (horizontal red line) approaches the average resistance of the harmonics (red line), that is $R_\Omega \approx R^{(1,2)}_{rad,2}$, namely when the efficiency of the harmonic is 50%, i.e., $\eta_n^{(TE,TM)} \approx 1/2$. In this case the calculations is carried out for $kr_{min} = 20$ and for externally tuned case. It can be also observed that lower losses also imply larger value of the optimal coefficients (see difference in the vertical scale for cases Figure 4.8(d) and Figure 4.8(c)). This renders their excitation on the minimum sphere extremely difficult and practically not so efficient because we need more dissipated power than radiated power to excite that number of SWs. For this reason, the bound in (4.11) does not give much information in practice. It is indeed more appropriate in our view to use Q-limited maximum gain concept presented in the following section.

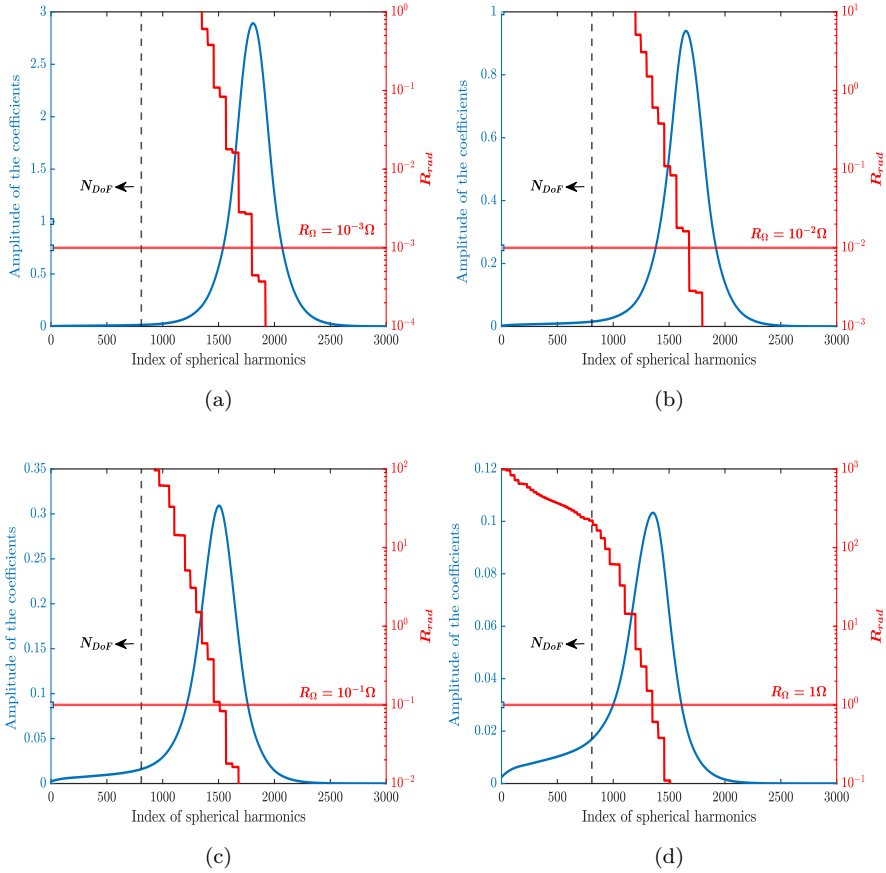

Figure 4.8: Envelope of the current coefficients and their amplitude for different values of the surface: (a) $R_\Omega = 10^{-3}\Omega$; (b) $R_\Omega = 10^{-2}\Omega$; (c) $R_\Omega = 10^{-1}\Omega$; (d) $R_\Omega = 1\Omega$. The amplitudes are normalized to have a unit radiated power ($P_r = 1W$). The dashed vertical line denotes N_{DoF} in absence of Q-bounds. The red line (right-hand side scale) represents the radiation resistance of the SW harmonics. The ohmic surface resistance is indicated by a horizontal red line; it crosses the curve of the radiation resistance of the harmonics approximately at the maximum of the envelope.

4.3.5 Physical interpretation for Small Antennas

In Chapter 3, a physical interpretation for small antenna was presented, suggesting that the combination of dipolar and quadrupolar contributions from Huygens' sources can be observed. In the context of maximum directivity, where losses are absent, the coefficients associated with the n-th spherical harmonics, whether TE or TM modes with azimuthal index $m \pm 1$, are identical. In contrast, in the context of gain, where losses are present, achieving maximum gain requires unbalanced coefficients. This generally renders the antenna non-resonant, implying that outside the minimum sphere, electric and magnetic energies are not balanced. For this reason,

to address this issue, an additional constraint has been introduced in Section 4.3.2 to attain a self-resonance condition. Similar to the procedure outlined in Chapter 3, this section employed a comparable approach. However, in this case, the coefficients are weighted by their respective efficiencies.
In the far zone the resulting electric field is proportional to

$$\boldsymbol{h} = \frac{3}{2}\left(\eta_1^{(TM)}\boldsymbol{h}_1^{(TM)} + \eta_1^{(TE)}\boldsymbol{h}_1^{(TE)}\right) + \frac{5}{2}\left(\eta_2^{(TM)}\boldsymbol{h}_2^{(TM)} + \eta_2^{(TE)}\boldsymbol{h}_2^{(TE)}\right) \tag{4.22}$$

where the explicit far-field pattern in (θ, ϕ) coordinates are

$$\boldsymbol{h}_1^{(TM)} = (\cos\theta\cos\phi)\hat{\theta} - \sin\phi\hat{\phi} \tag{4.23a}$$

$$\boldsymbol{h}_1^{(TE)} = \cos\phi\hat{\theta} - (\cos\theta\sin\phi)\hat{\phi} \tag{4.23b}$$

$$\boldsymbol{h}_2^{(TM)} = (\cos 2\theta\cos\phi)\hat{\theta} - (\cos\theta\sin\phi)\hat{\phi} \tag{4.23c}$$

$$\boldsymbol{h}_2^{(TE)} = (\cos\phi\cos\phi)\hat{\theta} - (\cos 2\theta\sin\phi)\hat{\phi} \tag{4.23d}$$

While $\boldsymbol{h}_1^{(TM)}$ and $\boldsymbol{h}_1^{(TE)}$ are the electric far-field pattern of the x-directed electric and y-directed magnetic dipoles, respectively, $\boldsymbol{h}_2^{(TM)}$ and $\boldsymbol{h}_2^{(TE)}$ are the electric and magnetic quadrupole, respectively. The latter are obtained by in phase combination of x-directed and z-directed electric quadrupoles, and y-directed and z-directed electric quadrupoles, respectively (see Figure 4.9).

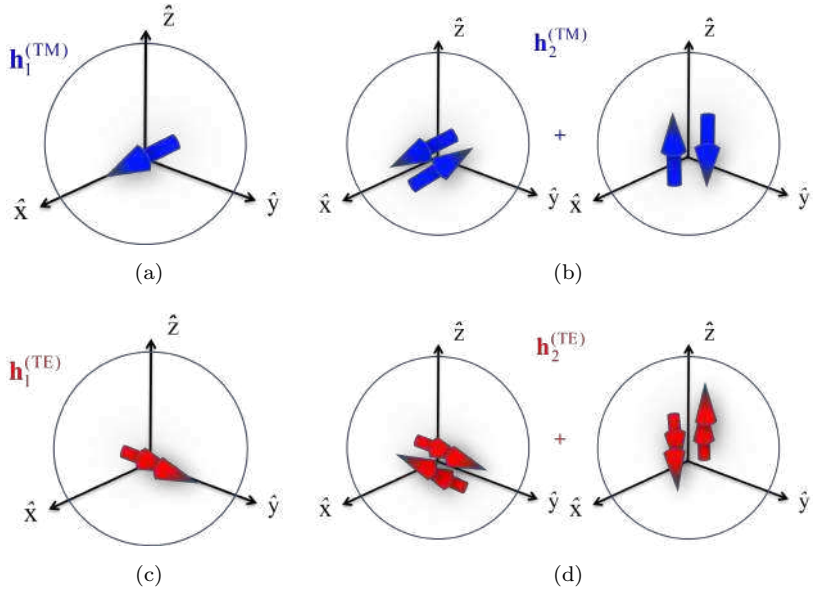

Figure 4.9: Elementary source associated with the far-field pattern of dipolar $\boldsymbol{h}_1^{(TM)}$ (a), $\boldsymbol{h}_1^{(TE)}$ (c) and quadrupolar $\boldsymbol{h}_2^{(TM)}$ (b), $\boldsymbol{h}_2^{(TE)}$ (d) contributions. Electric dipoles (TM) are denoted in blue with a single arrow and magnetic dipoles (TE) with a double arrow. The vertical doublet is aligned along x for electrical dipoles and along y for magnetic dipoles.

The maximum gain for this two terms approximation is given by

$$G_{max} \approx \frac{3}{2}\left(\eta_1^{(TM)} + \eta_1^{(TE)}\right) + \frac{5}{2}\left(\eta_2^{(TM)} + \eta_2^{(TE)}\right) \tag{4.24}$$

this corresponds to the maximum achievable gain for externally tuned small antennas.

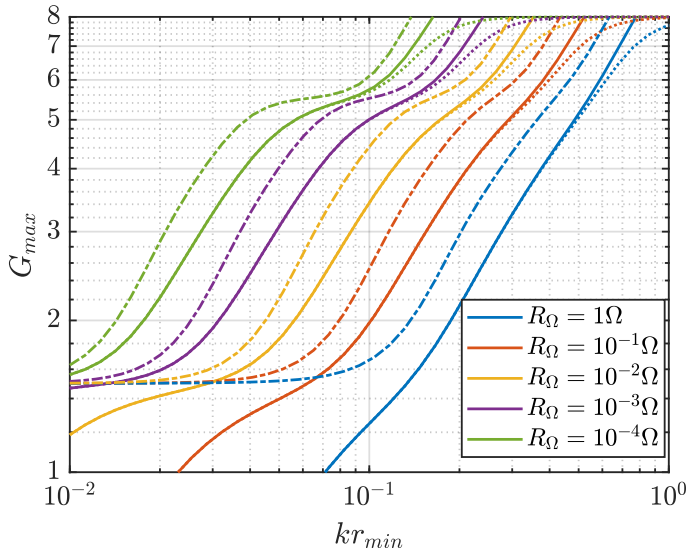

Figure 4.10: Maximum gain for externally tuned antennas calculated for different values of R_Ω as a function of kr_{min} using the full series in (4.11) (continuous lines) and the two terms approximation for small antennas in (4.24) (dash-dotted lines). Dotted lines are the corresponding directivities obtained by G_{max}/η with the full series.

Figure 4.10 shows the comparison between the maximum gain for externally tuned case obtained considering the full series in (4.11) (continuous lines) and two source contributions for small antennas in (4.24) (dash-dotted lines) for values of $R_\Omega \in [10^{-6}\Omega; 10^{-1}\Omega]$. The two expressions coincide below $G_{max} = 6$ and agrees reasonably till $G_{max} = 7$. In the same Figure has been plotted also the directivity (dotted lines) obtained by G_{max}/η with the full series.
Since analogous analyses can be conducted for self-resonant small antennas, the details will be omitted, and only the results will be reported in Figure 4.11. This Figure displays the comparison between the maximum gain obtained by considering the full series in (4.16) and the corresponding two-term approximation valid for small antennas.

4.4 Value of Q on the maximum gain curve

For the case of maximum gain, the presence of losses causes an unbalancing of the coefficients associated to the TE and TM modes. In this case, as we have seen in previous Section, the antenna naturally is not self-resonant. This implies that till a certain dimension of the antenna, the reactive electric energy W_e dominates, and therefore we should always apply the first of

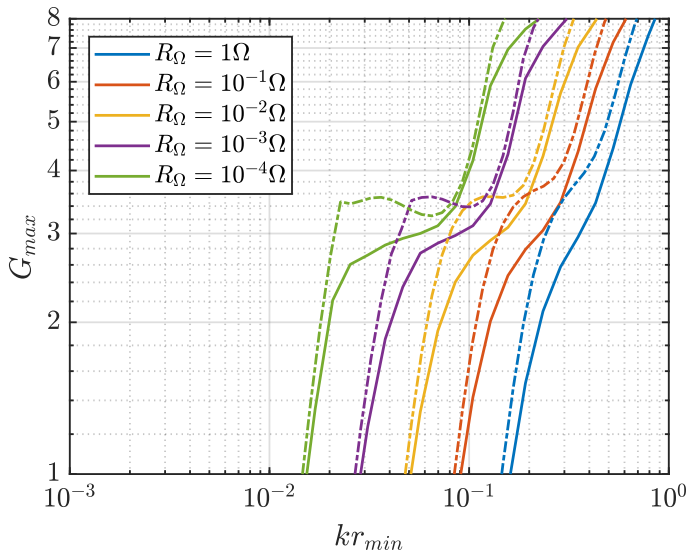

Figure 4.11: Maximum gain of self-resonant antennas calculated for different values of R_Ω as a function of kr_{min} using the full series in (4.16) (continuous lines) and the first two terms of the series in (4.16) valid for small antennas (dash-dotted lines).

(C.7) in Appendix C; therefore, using the electric field coefficients in (4.13) leads to

$$Q_{tot} = \frac{\sum_n (2n+1)\left[\left(\eta_n^{(TM)}\right)^2 Q'_n + \left(\eta_n^{(TE)}\right)^2 Q''_n\right]}{\sum_n (2n+1)\left[\left(\eta_n^{(TM)}\right)^2 + \left(\eta_n^{(TE)}\right)^2\right]} \tag{4.25}$$

The value of Q on the maximum Gain curve as a function of the antenna size is presented in Figure 4.12 for various values of the loss resistance. It is seen that the bandwidth (the inverse of Q_{tot}) becomes extremely small for small resistance, even if it corresponds to very high maximum gain limit. Furthermore, all the curves tend asymptotically, for small electrical size, to the value of Q that satisfy the Chu-limit, namely

$$Q_{tot} \to Q'_1 = \frac{1}{(kr_{min})^3} + \frac{1}{(kr_{min})} \text{ for } kr_{min} \to 0 \tag{4.26}$$

It is important to notice that for the case of self-resonant antennas the Q_{tot} converges to Q_1 reported (C.11) of Appendix C. This is because the TE modes (magnetic currents) are less efficient in the quasi-static limit.

Hence, he total Q-factor associated with the externally tuned gain for small antennas in (4.24) is

$$Q_{tot} = \frac{3\left(\eta_1^{(TM)}\right)^2 Q'_1 + 3\left(\eta_1^{(TE)}\right)^2 Q''_1 + 5\left(\eta_2^{(TM)}\right)^2 Q'_2 + 5\left(\eta_2^{(TE)}\right)^2 Q''_2}{3\left(\eta_1^{(TM)}\right)^2 + 3\left(\eta_1^{(TE)}\right)^2 + 5\left(\eta_2^{(TM)}\right)^2 + 5\left(\eta_2^{(TE)}\right)^2} \tag{4.27}$$

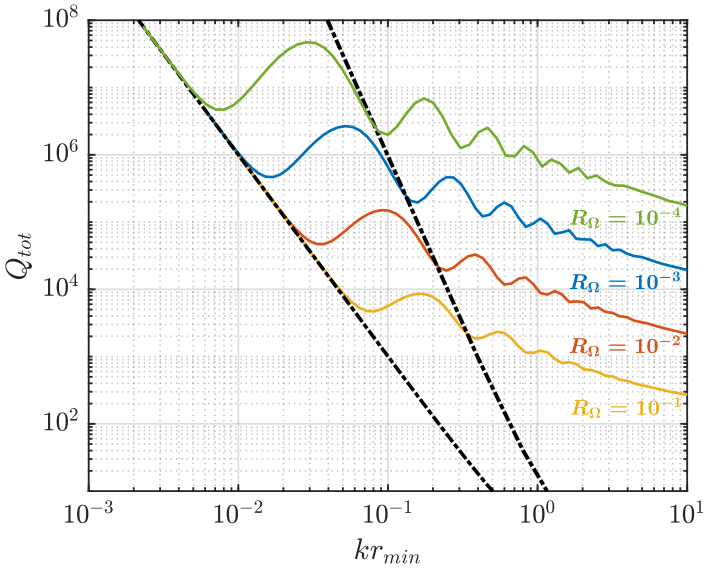

Figure 4.12: Quality factor of spherical wave expansion with coefficients associated to the maximum gain (4.13). The two dashed dotted lines represents Q_1' and Q_2''.

The explicit expression of the SW efficiency in (4.12) for small antennas are

$$\eta_1^{(TM)} = \frac{x^2}{x^2 + \frac{R_\Omega}{\zeta}(x^2+1)} \approx \frac{x^2}{x^2 + \frac{R_\Omega}{\zeta}} \tag{4.28a}$$

$$\eta_1^{(TE)} = \frac{x^4}{x^4 + \frac{R_\Omega}{\zeta}[(x^2-3)^2 + 9x^2]} \approx \frac{x^4}{x^4 + 9\frac{R_\Omega}{\zeta}} \tag{4.28b}$$

$$\eta_2^{(TM)} = \frac{x^4}{x^4 + \frac{R_\Omega}{\zeta}[(x^2-1)^2 + x^2]} \approx \frac{x^4}{x^4 + \frac{R_\Omega}{\zeta}} \tag{4.28c}$$

$$\eta_2^{(TE)} = \frac{x^6}{x^6 + \frac{R_\Omega}{\zeta}[(-x^3+6x)^2 + (-3x^2+6)^2]} \approx \frac{x^6}{x^6 + 36\frac{R_\Omega}{\zeta}} \tag{4.28d}$$

where $x = kr_{min}$ has been taken to simplify the form of the expressions. The equality in (4.28) are derived directly by the radiation resistance value (4.4) and the approximation is valid for $R_\Omega \in [10^6\Omega, 10^{-1}\Omega]$ and $G_{max} < 8$.
The exact values of the quality factors, in this case, are

$$Q_1' = \frac{1}{x^3} + \frac{1}{x} \tag{4.29a}$$

$$Q_1'' = \frac{1}{x} \tag{4.29b}$$

$$Q_2' = \frac{18}{x^5} + \frac{6}{x^3} + \frac{3}{x} \tag{4.29c}$$

$$Q_2'' = \frac{3}{x^3} + \frac{3}{x} \tag{4.29d}$$

Indeed, a reasonable approximation for the total quality factor is provided by

$$Q_{tot} \approx \frac{1}{x^3} \frac{1 + 30x^2 \left(\frac{x^2 + R_\Omega/\zeta}{x^2 + 9R_\Omega/\zeta} \right)^2}{1 + x^4 \left(\frac{x^2 + R_\Omega/\zeta}{x^4 + R_\Omega/\zeta} \right)^2} \tag{4.30}$$

with a validity range is till $G_{max} = 7$.

4.5 Maximum Super-Gain With Q-Bounds

In the previous Section we outlined that the expression in (4.11) does not give much information in practice. In this terms seems necessary to introduce a fundamental bound. It is indeed more appropriate in our view to use Q-limited maximum gain concept presented in this Section. This Q-bounded approach, driven by the Q-bounded super-directivity presented in Chapter 3, does not imply the excitation of unlimited number of harmonics, but the number of significant harmonics such to provide a given bandwidth. We stress here that Q-bounded maximization for gain, is a different concept from the maximization of the product bandwidth-gain [36], which leads to a different set of optimal current coefficient. It is seen that the TE optimal coefficients for the resonant case are higher in this case, in agreement with the fact that they are less efficient for small antennas. This bound can be found solving a problem of convex optimization of the current density by imposing a constraint on the bandwidth. The bandwidth is expressed in terms of Q-factor, which can be interpreted as the reciprocal of the fractional bandwidth. In obtaining the Q-bounded maximum gain, we assume that we always are in the condition $W_e > W_m$, so that to impose as a bound the first of (C.7) in Appendix C.
Mathematically the problem can be written as

$$\begin{aligned} \max_{|I_i|} \quad & \frac{\left| \sum_i \sqrt{R_{rad,i}} I_i K_i \right|^2}{\sum_i \left(R_{rad,i} + R_\Omega \right) |I_i|^2} \\ \text{s.t.} \quad & \frac{\sum_i Q_n R_{rad,i} |I_i|^2}{\sum_i R_{rad,i} |I_i|^2} = Q \end{aligned} \tag{4.31}$$

Since the procedure is similar to the one in Chapter 3, we omit the demonstration. The final expression is

$$G_{max} = \min_{\nu \in [0, \nu_{max}]} \sum_{n=1}^{\infty} \frac{1}{2} \left(\frac{\eta_n^{(TM)} (2n+1)}{\nu(\eta_n^{(TM)} Q'_n - Q) + 1} + \frac{\eta_n^{(TE)} (2n+1)}{\nu(\eta_n^{(TE)} Q''_n - Q) + 1} \right) \tag{4.32}$$

where $\nu_{max} = 1/(Q - \eta_1^{(TE)} Q'_1)$. It is important to observe that the above expression changes whenever $W_e < W_m$; in such a case, in accordance with (C.7) in Appendix C, it is only necessity to swap the Q'_n with Q''_n at resonance ($W_e = W_m$). The field coefficients for Q-bounded maximum gain are given by

$$C_i = \delta_i \frac{\eta_n^{(TE,TM)} \sqrt{2n+1}}{\nu_0(\eta_n^{(TE,TM)} Q''_n - Q) + 1} \tag{4.33}$$

where ν_0 is the value that maximize the series in (4.32) and δ_i is defined in (4.14).

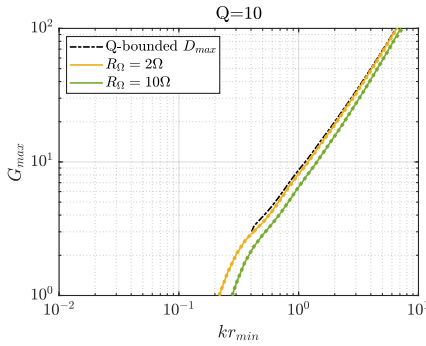

(a)

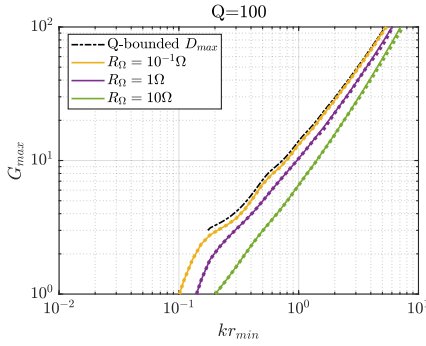

(b)

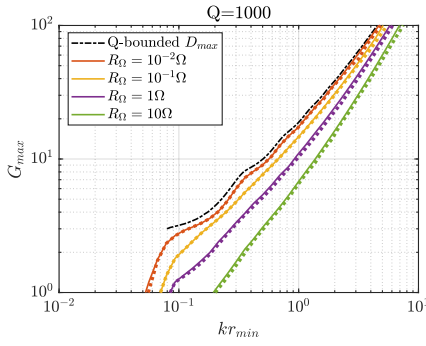

(c)

Figure 4.13: Q-bounded maximum gain in (4.32) as a function of the antenna size calculated for $Q = 10$ (a), $Q = 100$ (b), and $Q = 1000$ (c) and different values of the ohmic losses resistance R_Ω; the curves tend smoothly to the Q-bounded maximum directivity (black dash-dotted lines) when the losses tend to zero, i.e., the curve $R_\Omega = 0\Omega$ corresponds to the maximum Q-bounded super-directivity in (3.15).

In Figure 4.13 the Q-bounded maximum gain obtained using (4.32) is compared with a numerical

convex optimization obtain by expanding electric and magnetic currents in terms of spherical waves expansions (dotted lines); it can be noticed the excellent agreement between the numerical and the analytical results. Here it is important to emphasize the complex relationship between bandwidth and losses. For a fixed-size antenna, increasing the bandwidth may require a slight increase in losses to reduce the difference between maximum gain and maximum directivity. As losses decrease, the maximum gain tends to match the maximum directivity. The acceptable level of losses depends on the required Q. The gap between maximum directivity and maximum gain decreases for smaller losses when Q is larger. This can be mathematically represented by calculating the percentage error between the Q-bounded maximum gain in (4.32) and the Q-bounded maximum directivity in (3.15), namely

$$\epsilon = \frac{D_{max} - G_{max}}{D_{max}}. \tag{4.34}$$

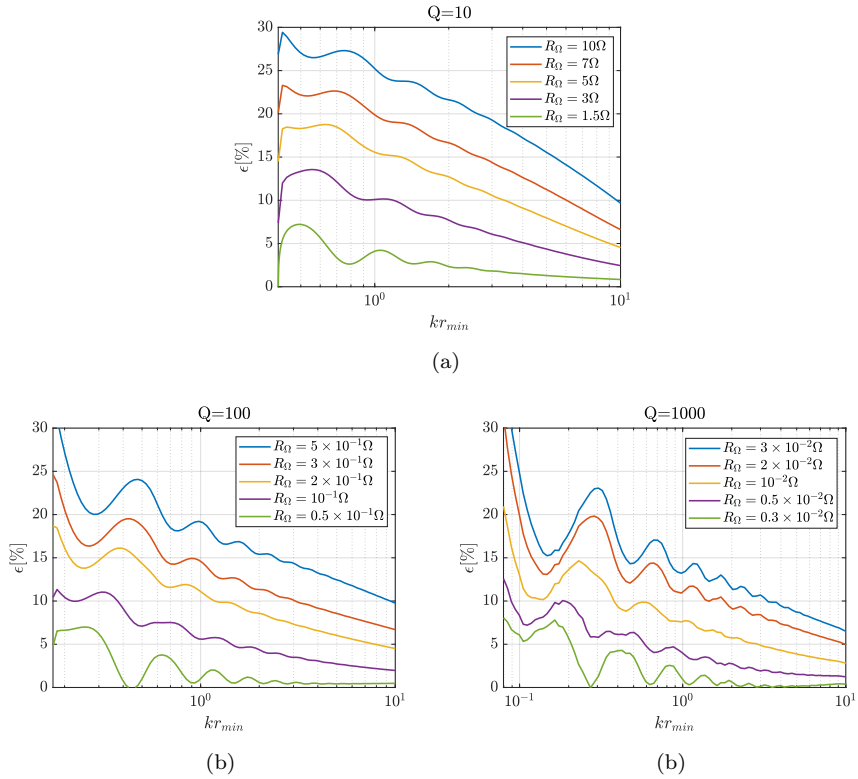

Figure 4.14: Percentage difference between maximum Q-bounded directivity in (3.15) and maximum Q-bounded gain in (4.32) for different values of the loss resistance. The green curves correspond to an efficiency larger than 93% in the overall range from the Chu-limit. (a) $Q = 10$; (b) $Q = 100$; (c) $Q = 1000$. The horizontal scale start form the corresponding Chu-limit for the different values of Q.

The latter corresponds to $1 - \eta$, where η is the efficiency. Figure 4.14 show the percentage error

for $Q = 10, 100, 1000$. It can be observed that for ϵ less than 7%, which correspond to an overall radiation efficiency of 93%, the relationship between the Q-factor and ohmic loss resistance R_Ω can be expressed as the following inequality

$$Q < \frac{9}{R_\Omega^{0.8}} + 3. \tag{4.35}$$

This means that in this range one can calculate the maximum gain using the maximum directivity formula in (3.15). The situation is graphically illustrated in Figure 4.15. We should also emphasize that the inequality in (4.35) is not valid for $W_e < W_m$, where one has to interchange Q'_n and Q''_n to get the right maximization.

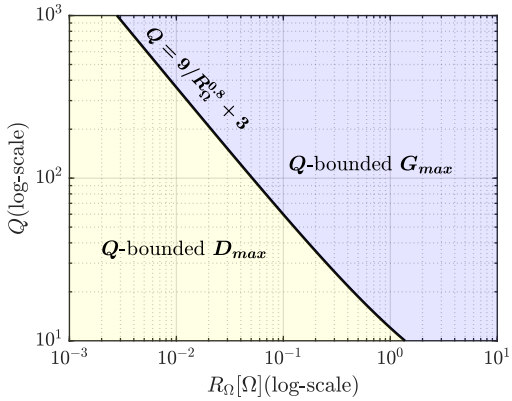

Figure 4.15: Region of validity of the various formulas for Q-bounded maximum gain with losses in (4.32) and Q-bounded maximum directivity without losses. For $Q < 9/R_\Omega^{0.8} + 3$, eq.(4.32) can be used with a maximum error less than 7% for all antenna sizes.

4.6 Maximum Gain calculated by the discretization of the radiation operator

The determination of the maximum gain can be accomplished by discretizing the radiation operator, resulting in a numerical process. The discretization of the radiation operator permits to express the far-fields in matrix representation. In Appendix D the formulation has been presented and led to the final expression in (D.12) between the far field radiation vector $[V_m]$ and the current vectors $[I_n]$, i.e., $[V] = [F][I]$. In the following this procedure is applied to a spherical shape and to a parallelepipal box shape.

4.6.1 Maximum Gain for Spherical Shape

Let's consider a minimum sphere and another sphere surrounding the minimum sphere as an observation for the far-field, as can be seen in Figure 4.16(a). On the minimum sphere has

been placed a pair of orthogonal electric dipoles as point sources (Figure 4.16(b)). The choice to consider a pair of mutually orthogonal dipoles is motivated by the existence of the two polarizations (TE and TM). These dipoles are located at the center of regions on the sphere, each having equal area. To divide the sphere into regions of equal area, we utilized the algorithm proposed by Leopardi in [71]. Same considerations has been done for the observation spherical surface. Let $2N$ be the total number of sources (N being the number of orthogonal dipole pairs) and let $2M$ the total number of observation points at far-field (M being the number of orthogonal dipole pairs on the observation sphere). In this case, an equal number of source and observation points will be considered, i.e., $N = M$. The rows of matrix $[F]$ correspond to the number of observation points, while the columns correspond the number of source points. Indeed, the far-field matrix $[F]$ will be a square matrix.

For the maximization of the gain is necessary to establish a specific observation direction and

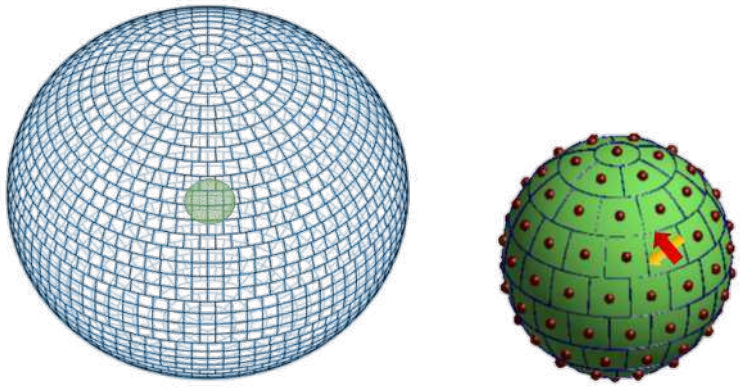

(a) (b)

Figure 4.16: (a) Graphical representation of the source region sphere (small green sphere) and of the observation far-field sphere (big blue sphere); (b) Graphical representation of the source region sphere, the red dot are the location of the two orthogonal electric dipoles.

locate the currents that will optimize the maximization in that particular direction. Without losing generality, we may assume that this direction $\hat{\boldsymbol{r}}_1$ is corresponding to $m = 1, 2$ in the previous notation. We can therefore define

$$\left[V_1, V_2\right]^\dagger = \left[F_{m,n}\right]_{m=1,2;n=1,2N} \left[I_n\right]_{n=1,2N} \rightarrow \left[V'\right] = \left[F'\right] \left[I\right] \tag{4.36}$$

where $[V'] = [V_1, V_2]^\dagger$ is a two-component vector column and $[F']$ is a $2 \times 2N$ matrix obtained by the first two rows of $[F]$.

The corresponding radiation intensity in direction $\hat{\boldsymbol{r}}_1$ can be expressed in a matrix form as

$$U(\hat{\boldsymbol{r}}_1) = \frac{1}{2\zeta} \left[V'\right]^\dagger \left[V'\right] = \frac{1}{2\zeta} \left[I\right]^\dagger \left[F'\right]^\dagger \left[F'\right] \left[I\right] \tag{4.37}$$

The radiated power can be calculated as the integration of the radiation intensity in every directions of the space or, in matrix form, as

$$P_{rad} = \frac{4\pi}{N}\frac{1}{2\zeta}\left[V\right]^{\dagger}\left[V\right] = \frac{4\pi}{2\zeta N}\left[I\right]^{\dagger}\left[F\right]^{\dagger}\left[F\right]\left[I\right] \tag{4.38}$$

The power dissipated in matrix form is

$$P_{rad} = \frac{1}{2}R_{\Omega}\left[I\right]^{\dagger}\left[I\right] \tag{4.39}$$

Hence, from the general definition of gain in (4.2), we can write the antenna gain in the preferential direction $\hat{\boldsymbol{r}}_1$ as

$$G(\hat{\boldsymbol{r}}_1) = 4\pi\frac{U(\hat{\boldsymbol{r}}_1)}{P_{rad}+P_{\Omega}} = \frac{[I]^{\dagger}[F']^{\dagger}[F'][I]}{[I]^{\dagger}\left(\frac{[F]^{\dagger}[F]}{N}+\frac{\zeta}{4\pi}R_{\Omega}[1]\right)[I]} \tag{4.40}$$

To maximize the gain we can simply maximize the ratio in (4.40) with respect to the current $[I]$ namely,

$$G(\hat{\boldsymbol{r}}_1) = \max_{[I]}\left\{\frac{[I]^{\dagger}[F']^{\dagger}[F'][I]}{[I]^{\dagger}\left(\frac{[F]^{\dagger}[F]}{N}+\frac{\zeta}{4\pi}R_{\Omega}[1]\right)[I]}\right\} \tag{4.41}$$

Consequently, the maximization of the gain can be formulated as the following optimization problem, where the total power (denominator of (4.40)) is normalized to unity:

$$\begin{aligned} \max_{[I]} \quad & [I]^{\dagger}[F']^{\dagger}[F'][I] \\ \text{s.t.} \quad & [I]^{\dagger}\left(\frac{[F]^{\dagger}[F]}{N}+\frac{\zeta}{4\pi}R_{\Omega}[1]\right)[I] = 1 \end{aligned} \tag{4.42}$$

The solution of the optimization problem in (4.42) can be determined via the following generalized eigenvalue problem

$$[F']^{\dagger}[F'][I] = \lambda\left(\frac{[F]^{\dagger}[F]}{N}+\frac{\zeta}{4\pi}R_{\Omega}[1]\right)[I] \tag{4.43}$$

By multiplication both member of (4.43) for the matrix $[F']\left(\frac{[F]^{\dagger}[F]}{N}+\frac{\zeta}{4\pi}R_{\Omega}[1]\right)^{-1}$ we can rewrite it as the following 2×2 problem

$$[F']\left(\frac{[F]^{\dagger}[F]}{N}+\frac{\zeta}{4\pi}R_{\Omega}[1]\right)^{-1}[F']^{\dagger}[V'] = \lambda[V'] \tag{4.44}$$

Finally, the resolution of the maximization of the original problem in (4.41) is reduced to find the maximum eigenvalues between $\{\ \lambda_1, \lambda_2\}$ of the matrix $[F']\left(\frac{[F]^{\dagger}[F]}{N}+\frac{\zeta}{4\pi}R_{\Omega}[1]\right)^{-1}[F']^{\dagger}$, namely

$$G_{max} = \lambda_{max} \doteq \{\ \lambda_1, \lambda_2\} \tag{4.45}$$

We can also derive the optimal currents that realized this gain

$$[I]_{opt} = \left(\frac{[F]^{\dagger}[F]}{N}+\frac{\zeta}{4\pi}R_{\Omega}[1]\right)^{-1}[F']^{\dagger} \tag{4.46}$$

This procedure illustrated is purely numerical and very easy to solve, below a different procedure using the SWs harmonics to expand the radiated field, which lead to similar results presented in Section 4.3.

4.6.2 Maximum Gain for Parallelepipal Box Shape

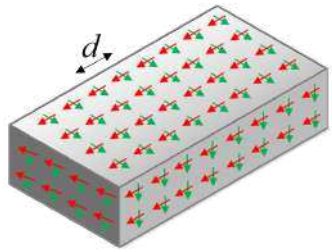

Figure 4.17: Graphical representation of the box shape, the pair of orthogonal dipoles are located on the six faces of the box and separated by a distance d to each other.

Let's assume we consider a parallelepipal box shape. On each of the six faces of the box, a pair of electric dipoles is positioned, with their orientations perpendicular to each other and separated by a distance d (refer to Figure 4.17). The box is surrounded by spherical region, which constitute the observation region at the far-field (Figure 4.16(a)), divided in sub-regions of equal area using Leopardi algorithm [71]. The electric far-field radiated by every pair of elements is calculated for every θ and ϕ directions, and gathered into a matrix $[F]$ of dimensions $2M \times 2N$, where M is the number of observation points at the far-field, and N is the number of sources (numbers of electrical dipoles (see Appendix D). For the maximization of the gain we fix a certain direction of observation $\hat{\boldsymbol{r}}_1$. The far-field in maximum directions $\hat{\boldsymbol{r}}_1$ is gathered into a matrix $[F']$ of dimensions $2 \times 2N$. To solve the problem we use the numerical approach described in Section 4.6.1, which consist on finding the maximum eigenvalue of a 2×2 matrix (4.45).

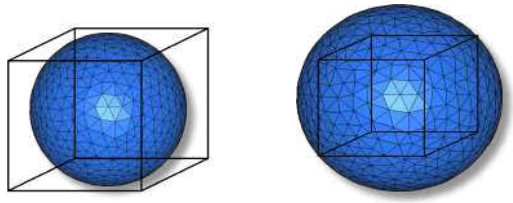

(a) (b)

Figure 4.18: Graphical representation of the study case of the box circumscribed to the sphere (a) and of the box inscribed within the sphere (b).

To compare the outcomes, we examined both a box that circumscribes a sphere (refer to Figure 4.18(a)) and a box that is inscribed within a sphere (refer to Figure 4.17(b)). The maximum gain for the box that circumscribes a sphere and the box that is inscribed within a sphere are

reported in Figure 4.20 and Figure 4.15, respectively. The results are highly alike because the volumes of the box and the sphere are nearly equal, particularly in the instance of the box inscribed within the sphere.

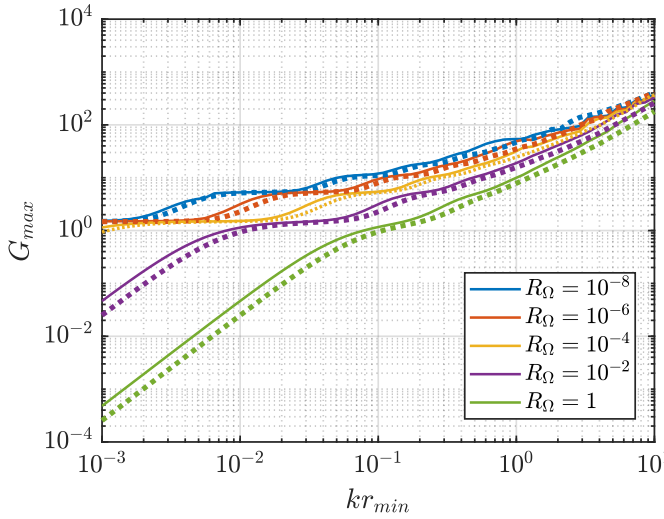

Figure 4.19: Maximum gain of the box circumscribed to the sphere (continuous lines) compared with the one of the sphere (dotted lines) for different values of R_Ω.

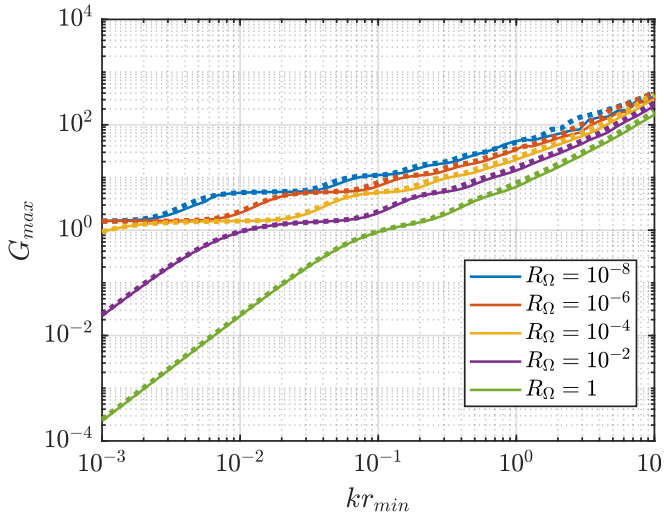

Figure 4.20: Maximum gain of the box inscribed within the sphere (continuous lines) compared with the one of the sphere (dotted lines) for different values of R_Ω

4.7 Conclusions

In this paper has shown several general properties of the maximum gain of arbitrary antennas of given electrical sizes. Analytical forms for the maximum antenna gain as a function of the losses and in absence and presence of Q-bounds have been presented for both resonant and non-resonant (externally tuned) cases. The exact solution is given in terms of a series that should be minimized wrt a single parameter. For small antennas a closed form is provided that is accurate till maximum gain equal to 7. An interesting interpretation in terms of magnetic and electric dipoles has been provided. Numerical solution for the maximum gain through the democratization of the radiation operator has been also derived for a spherical region, the results are also extent to a parallelepipal box shape.

Chapter 5

Degrees of Freedom and relationship with Super-Directivity

5.1 Introduction

This Chapter introduces the concept of the degrees of freedom (DoF) of the field. The DoF number is the minimum number of parameters necessary to describe the electromagnetic field at a certain distance from a minimum surface enclosing the sources, so that the reactive field is negligible. This number is based on the limited spatial bandwidth of the EM fields and is directly proportional to the square of the minimum sphere radius in terms of wavelength. The maximum antenna super-directivity is investigated in relationship with the number of DoF of the field.

5.2 Degrees of Freedom and Maximum Directivity of non-super-directive antennas

The number of Degrees of Freedom (N_{DoF}) of the field radiated by an arbitrary sources in a given domain, contained within a minimum surface S, is the minimum number of independent scalar parameters sufficient to describe the field and its evolution, i.e., the number of scalar coefficients needed for an accurate and non-redundant description of the field, in that domain. In eq.(3.1) of Chapter 3 the maximum directivity in absence of super-reactive source has been defined as the one of a large illuminated circular aperture of area and the same radius of the sphere surrounding the sources. Consider for instance a spherical surface S with an electrically large radius r_{min} surrounding the sources and an observation domain given by the entire space outside S except for a small region close to S, where very reactive fields originating from the source region within S may dominate. In this case, the number of degrees of freedom is given by [31]

$$N_{DoF} = 2D_{max} \tag{5.1}$$

where the factor 2 is a result of the two orthogonal polarizations, corresponding to TE (transverse electric) and TM (transverse magnetic) modes. From eq. (5.1) we can interpret the maximum directivity of a system as a measure of the degrees of freedom of the power density radiated by the system. Hence, $N_{DoF}/2$ can be seen to be the maximum number of non-overlapping pencil beams that can be radiated by the sources contained in the minimum sphere. It is convenient to introduce the definition of the beam solid angle Ω_A, defined as the solid angle through which

all the power of the antenna would flow if its radiation intensity were constant and equal to its maximum value U_{max}. The idea, illustrated in Figure 5.1(a), gives the following expression [62]

$$\Omega_A = \iint_{(\theta,\phi)} \frac{U(\theta,\phi)}{U_{max}} sin\theta d\theta d\phi \tag{5.2}$$

where $U(\theta,\phi)$ is the radiation intensity per unit solid angle and U_{max} is its maximum value. For directive antennas (with directivity larger than 20 dB) the solid beam angle can be approximated as the product of the 3 dB angles in the two principal planes. The solid beam angle is also related

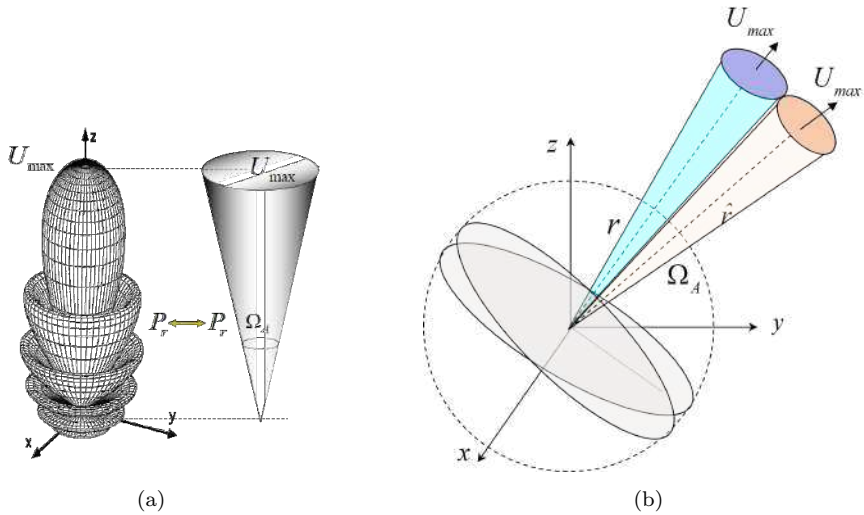

(a) (b)

Figure 5.1: (a) graphical illustration of the solid beam angle for a highly directive antenna. This angle is approximately equal to the product of the 3dB angles in the two principal planes. (b) illustration of the DoF as the number of beam angles coming from the maximum area of the sphere in independent directions.

to the directivity in the direction of the maximum intensity (see Figure 5.1(b)) as

$$D_{max} = 4\pi \frac{U_{max}}{P_r} = 4\pi \frac{U_{max}}{\iint_{4\pi} U(\theta,\phi) d\Omega} = \frac{4\pi}{\Omega_A} \tag{5.3}$$

The Degrees of Freedom can be also seen as the number of non-overlapped solid beams angles produced by any rotating, constant phase and equi-amplitude illuminated circular areas inside the minimum sphere. Therefore, the ratio between the total solid angle and the beam angle associated with a constant-amplitude-phase dish is also the number of degrees of freedom (except for a factor 2 due to the polarizations); that can be written by applying eq.(3.1) of Chapter 3 as

$$N_{DoF} = 2\frac{4\pi}{\Omega_{r_{min}}} = 2D_{max} = 2(kr_{min})^2 \tag{5.4}$$

where $\Omega_{r_{min}} = \Omega_{A=\pi r_{min}^2}$. It can be noticed that the maximum directivity in (5.4) is valid for a large radius (namely, asymptotically) and for non-super-reactive sources [31]. Indeed,

it is well known that if one is able to excite a strong reactive field close to the antenna, the equivalent area of the antenna can be larger than its physical area [70]. Nevertheless, the trade-off for this advantage is the antenna's typically low efficiency due to its low radiation resistance. Additionally, the resulting bandwidth is extremely limited. It is important to mention that the maximum directivity and DoF equivalence expressed in equation (5.4) justifies (5.1) as asymptotic concept, namely valid for large sphere in terms of the wavelength. However, we can argue that the relation in (5.1) can be valid even for intermediate and small radii. To this end, the process suggested by Hansen [61] can be followed, which is anyway valid for non super-reactive cases. The process suggested by Hansen in eq.(2.225) page 57, brings to the following expression of the maximum directivity:

$$D_{max} = n_0(n_0 + 2) \tag{5.5}$$

where n_0 is the maximum polar spherical harmonics index that can be excited over the minimum sphere. Due to the cut-off behaviour of the spherical harmonics one has $n_0 = \lceil kr_{min} \rceil$, where $\lceil \cdot \rceil$ denotes the smallest integer larger or equal to its argument; hence, the following formula holds

$$D_{max} = \lceil kr_{min} \rceil^2 + 2\lceil kr_{min} \rceil = \frac{N_{DoF}}{2} \tag{5.6}$$

where we have identified the DoF with the max directivity, without motivating it. Eq.(5.6) is valid even for very small antennas, where we know that the degrees of freedom are 6 (3 orthogonal electric and three orthogonal magnetic dipoles) and the maximum directivity is the one of a Huygens source. We can argue that formula in (5.6) is valid even for intermediate-size source regions.

5.2.1 Degrees of Freedom for a limited angular region

For a reduces solid angular region Ω the degrees of freedom of the field are given by the number of solid beam angle $\Omega_{r_{min}}$ contained in Ω as depicted in Figure 5.2, namely

$$N_{DoF}^{\Omega} = \frac{\Omega}{\Omega_{r_{min}}} = \frac{\Omega}{4\pi} N_{DoF} \tag{5.7}$$

In defining (5.7) it is seen that the peripheral beams does not fit perfectly into the cone, especially if the beams are large (small sphere). This approximation in (5.7) is indeed asymptotic, its rigorous value can be found on as using the Singular Value Decomposition that will shown in the following Sections.

5.2.2 Approximate expression of DoF for convex minimum region

When the source is included in a minimum surface different form a sphere, provided the shape is convex, the N_{DoF} can be approximated as suggested in [72], namely

$$N_{DoF} \simeq 2\frac{\Sigma}{(\lambda/2)^2} \doteq N_{DoF}^{(\Sigma)} \tag{5.8}$$

where Σ is the surface bounding the support sources. In case of spherical support, (5.8) does not give exactly the expression in (5.1), and the ratio between the two formulas in (5.1) and (5.8)

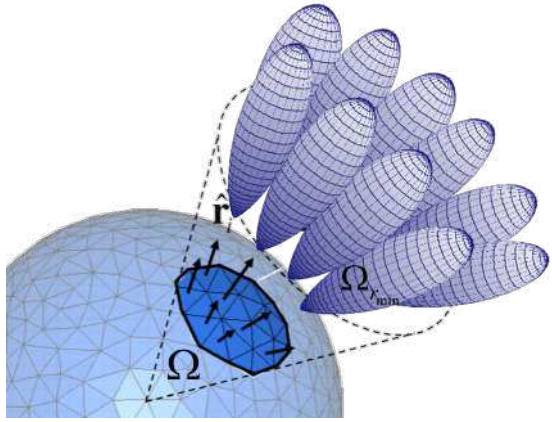

Figure 5.2: Graphical illustration of the independent beams of beam angles $\Omega_{r_{min}}$ contained in a finite solid angle Ω. The number of these independent beams gives the degrees of freedom of the field in the solid angle Ω.

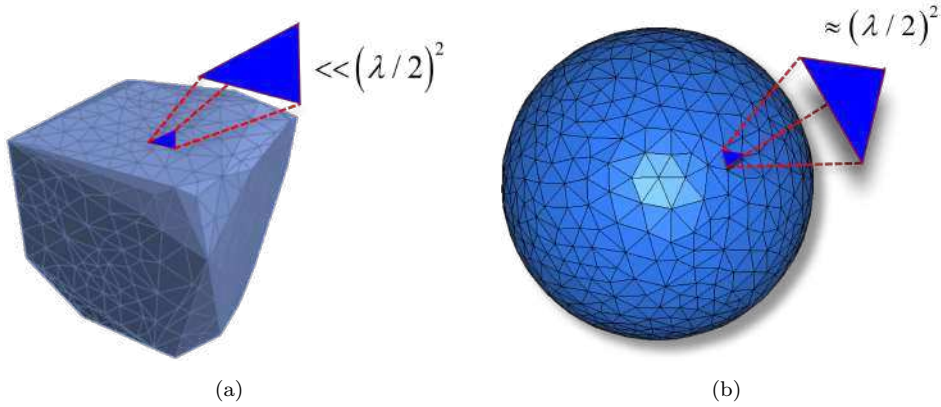

(a) (b)

Figure 5.3: Graphical illustration of eq. (5.8). The N_{DoF} of sources contained in a given surface is interpreted as the number of sub-surfaces of area $(\lambda/2)^2$ that can be distributed over the surface. (a) actual surface; (b) minimum spherical surface.

is $N_{DoF}/N_{DoF}^{(\Sigma)} = \pi/4$. Equation (5.8) is the space-domain counterpart of eq. (5.4) (see Figure 5.3(a)). The idea behind eq. (5.8) is that details smaller than $\lambda/2$ cannot be distinguished by the radiation operator. The factor 2 again depends on the fact that two possible orthogonal sources can be located over the surface.

5.2.3 DoF calculation by means of SVD

A rigorous value of the DoF number can be found by means of the Singular Value Decomposition (SVD), introduced in Appendix E, of the radiation operator in (5.16) of Appendix D, which maps the currents on the source boundary onto the radiated field in the observation domain. In the

following, the SVD method is employed to determine the degrees of freedom initially for a generic surface and for a spherical surface.

General limiting surface

Considering a general limiting surface as the one in Figure 5.3(a), once one has found the matrices $[V]$ and $[I]$ through the SVD of $[F]$ has indicated in Appendix E, it is possible to find the N_{DoF} through the rank of $[F]$ (number of non-negligible singular values), and also the characteristic modes of the minimum surface S in both space (currents) and spectral (far-field) domains. In fact, the columns of $[V]$ define the coefficients of far-field orthogonal modes in the chosen spectral (far-field) basis, while the columns of $[I]$ define the coefficients of the orthogonal currents in the chosen spatial basis.
Denoting by $[V_{mq}]_{m=1,2M}^{q=1,2M}$ and $[I_{nq}]_{n=1,2N}^{q=1,2N}$ the orthogonal matrices coming from the SVD of $[F]$, one has

$$\big[V_{mq}\big]_{m=1,2M}^{q=1,2M} = \big[V_m^{(1)}, ...V_m^{(q)}, ...V_m^{(2M)}\big]_{m=1,2M} \tag{5.9a}$$

$$\big[I_{nq}\big]_{n=1,2N}^{q=1,2M} = \big[I_n^{(1)}, ...I_n^{(q)}, ...V_n^{(2N)}\big]_{n=1,2N} \tag{5.9b}$$

$$\sigma_q\big[V_m^{(q)}\big]_{m=1,2M} = \big[F_{m,n}\big]_{m=1,2M;n=1,2N}\big[I_n^{(q)}\big]_{n=1,2N} \tag{5.9c}$$

From the unitary of $[V]$ and $[I]$ matrices one has

$$\sum_{n=1}^{2N} |I_n^{(q)}|^2 = 1 \tag{5.10a}$$

$$\sum_{n=1}^{2M} |V_m^{(q)}|^2 = 1 \tag{5.10b}$$

Therefore, the coefficients of the characteristic modes of currents and fields can be defined as

$$\boldsymbol{J}^{(q)}(\boldsymbol{r}') = \sum_{n=1}^{N} \big[I_n^{(q,1)} f_n^{(1)}(\boldsymbol{r}')(\boldsymbol{p})_n^{(1)} + I_n^{(q,2)} f_n^{(2)}(\boldsymbol{r}')(\boldsymbol{p})_n^{(2)}\big] \tag{5.11a}$$

$$\boldsymbol{V}^{(q)}(\hat{\boldsymbol{r}}) = \sum_{m=1}^{M} \big[V_m^{(q,\theta)}\hat{\theta} + V_m^{(q,\phi)}\hat{\phi}\big]\eta_{\Omega_m}(\hat{\boldsymbol{r}}) \tag{5.11b}$$

with

$$f_n^{(i)}(\boldsymbol{r}') = 0 \text{ for } \boldsymbol{r}' \notin \Delta S_n \tag{5.12a}$$

$$\eta_{\Omega_m}(\hat{\boldsymbol{r}}) = \begin{cases} 0 & \text{for } \hat{\boldsymbol{r}} \in \Delta\Omega_m \\ 1 & \text{for } \hat{\boldsymbol{r}} \notin \Delta\Omega_m \end{cases} \tag{5.12b}$$

$$q = 1, ..., N_{DoF} \tag{5.12c}$$

where we have renumbered the SVD-based column coefficients according to the original definition in (D.5) and (D.7) in Appendix E. In (5.11), $\boldsymbol{J}^{(q)}(\boldsymbol{r}')$ represents the q-th characteristic mode

of the currents, and $\boldsymbol{V}^{(q)}(\hat{\boldsymbol{r}})$ its relevant radiation vector. We observe that all the quantities in (5.11) can be derived from the SVD of the Green's function $[F]$-matrix in (E.2) of Appendix D. From (5.11) we can also derive the physical meaning of the singular values. To this end, we define the average current of the mode $I_0^{(q)}$ by

$$\left|I_0^{(q)}\right|^2 = \iint_S \boldsymbol{J}^{(q)}(\boldsymbol{r}') \cdot \boldsymbol{J}^{(q)^*}(\boldsymbol{r}')\, dS = \sum_{n=1}^{N} \left[\left|I_0^{(q,1)}\right|^2 + \left|I_0^{(q,2)}\right|^2\right] = 1 \tag{5.13}$$

where the last step is motivated by the fact that the $[I]$ matrix is unitary. On the other hand, the power radiated by the q-th mode can be defined as the integral of the radiation intensity, namely

$$P_r^{(q)} = \frac{1}{2\zeta} \iint \sigma_q^2 \left|\boldsymbol{V}^{(q)}(\hat{\boldsymbol{r}})\right|^2 d\Omega = \frac{1}{2\zeta}\sigma_q^2 \sum_{m=1}^{M} \left[\left|V_m^{(q,\theta)}\right|^2 + \left|V_m^{(q,\phi)}\right|^2\right] 4\pi = \frac{4\pi}{2\zeta N}\sigma_q^2 \tag{5.14}$$

where the last equality is due to the fact that the matrix $[V]$ is unitary. We may define a radiation resistance of the characteristic mode as

$$R_r^{(q)} = \frac{P_r^{(q)}}{\frac{1}{2}\left|I_0^{(q)}\right|^2} = \frac{4\pi}{\zeta N}\sigma_n^2 \tag{5.15}$$

The above equation identifies the square of the singular values with the radiation resistance of the characteristic mode up to a multiplicative constant. Since the singular values decrease with the mode index, this means that it will be more and more difficult to excite characteristic modes with increasing index over the S domain.

5.2.4 Spherical surface case

The particular case of a spherical source region (see Figure 5.3(b)) and a spherical observation domain can be conveniently treated with spherical wave (SW) expansion introduced in Appendix A.

In the limit of infinite density of test and source points, the singular vectors become continuous functions, and are called *singular modes* or *singular functions* [73]. In that case the radiation operator L takes the following integral form

$$\boldsymbol{E}_t(R,\theta,\phi) = L\{\boldsymbol{J}(r_{min},\theta',\phi')\} = -\hat{r}\times\hat{r}\times\int_0^{2\pi}\int_0^{\pi} \underline{\underline{\boldsymbol{G}}}_{ee}(\boldsymbol{r},\boldsymbol{r}')\cdot\boldsymbol{J}(r_{min},\theta',\phi') r_{min}^2 \sin\theta'\, d\theta'\, d\phi' \tag{5.16}$$

where the subscript t denotes the radially transverse component, $\underline{\underline{\boldsymbol{G}}}_{ee}$ is the dyadic Green's function, r_{min} is the radius of the source sphere, and R is the radius of the observation sphere. Note that we are not obliged to assume that R id in the far region wrt the source region. In [59] is shown that for spherical source and observation domains spherical waves represent the singular functions of the radiation operator. Furthermore, the self-adjoint operator LL^H and L^HL, where L^H is the adjoint of the operator L in (5.16), are diagonalizable with positive eigenvalues

$$\sigma_q^2 = k^4\zeta^2\left|r_{min}^2 R_{s,n}^{(3)}(kR)R_{s,n}^{(1)}(kr_{min})\right|^2 \tag{5.17}$$

where $q = 2[n(n+1) + m - 1] + s$ convert the triple spherical-wave index (s, m, n) in a unique index q, and $R^{(c)}_{s,n}$ is the function describing the radial dependency of the spherical harmonics defined in Appendix A. By definition, the singular values of the operator L in (5.17) are the square roots of the eigenvalues of the self-adjoint operators LL^H and $L^H L$, namely

$$\sigma_q = k^2\zeta\left|r^2_{min}R^{(3)}_{s,n}(kR)R^{(1)}_{s,n}(kr_{min})\right| \tag{5.18}$$

which can be rewritten in terms of spherical Bessel's and Hankel's functions as

$$\sigma_q = k^2\zeta\left|r^2_{min}h_n(kR)j_n(kr_{min})\right| \tag{5.19}$$

and approximated as

$$\sigma_q = \frac{k\zeta r^2_{min}}{R}\left|j_n(kr_{min})\right| \tag{5.20}$$

For a finite number of test points and current functions, the identification of the singular functions with the Sws is no more exact; however, the physical interpretation of the outcome of the SVD remains the same. To illustrate the concept, consider a partition of the source sphere in N small regions of equal areas and define at each point $\boldsymbol{r}_n$ at the center of these regions a couple of orthogonal elementary electric dipoles to be used as basis for the current expansions (see the inset of Figure 5.4). Referring to eq. (5.16), this is equivalent to choose

$$f^{(1)}_n(\boldsymbol{r}') = f^{(2)}_n(\boldsymbol{r}') = \delta(\boldsymbol{r}' - \boldsymbol{r}_n) \tag{5.21a}$$

$$\boldsymbol{p}^{(1)}_n = \hat{\theta}(\boldsymbol{r}_n) \tag{5.21b}$$

$$\boldsymbol{p}^{(2)}_n = \hat{\phi}(\boldsymbol{r}_n) \tag{5.21c}$$

$$\tag{5.21d}$$

The field radiated by these sources is tested at a similar set of points on the observation sphere. When the samples on the equivalence surface S and on the test surface are sufficiently dense, the product between the Green's function matrix and the current vector can be interpreted as a discretization of the radiation integral in (5.16) after multiplication by the elementary area $dA = 4\pi r^2_{min}/N$. In this case, the significant singular values of the Green's function matrix for $N \to \infty$ stabilizes to the value

$$\sigma_q = k^2\zeta\left|\frac{r^2_{min}R^{(3)}_{s,n}(kR)R^{(1)}_{s,n}(kr_{min})}{dA}\right| = k^2\zeta\left|r^2_{min}R^{(3)}_{s,n}(kR)R^{(1)}_{s,n}(kr_{min})\frac{N}{4\pi}\right| \tag{5.22}$$

This is illustrated in Figure 5.4, where the red curve stepped curve represents on a logarithm scale the magnitude of the singular values σ_q in (5.22) normalized to the largest one for $r_{min} = 2\lambda$ and $R = 7\lambda$. In the same Figure, the other colored curves represent the numerical singular values of the square matrix of Green's functions of different dimensions $2N$. As expected, numerical and analytical values tend to coincide for $N \to \infty$, while for any finite value of N the first $N' < N$ singular values are stabilized to the corresponding analytical value. For instance, with a number of dipoles equal to $2N_0$ the corresponding the first N_0 singular values are retrieved with a relative error less than 2%. The corresponding discrete singular vectors should be in principle correspond to sampled spherical harmonics. However, since $2n + 1$ modes characterized by a given couple of indices (s, n) have the same singular value, i.e., the modes are degenerate wrt to the index m, the j-th left and right singular vectors generated by the SVD can be the sampling of any linear combination of all the spherical harmonics characterized by the corresponding indices (s, n).

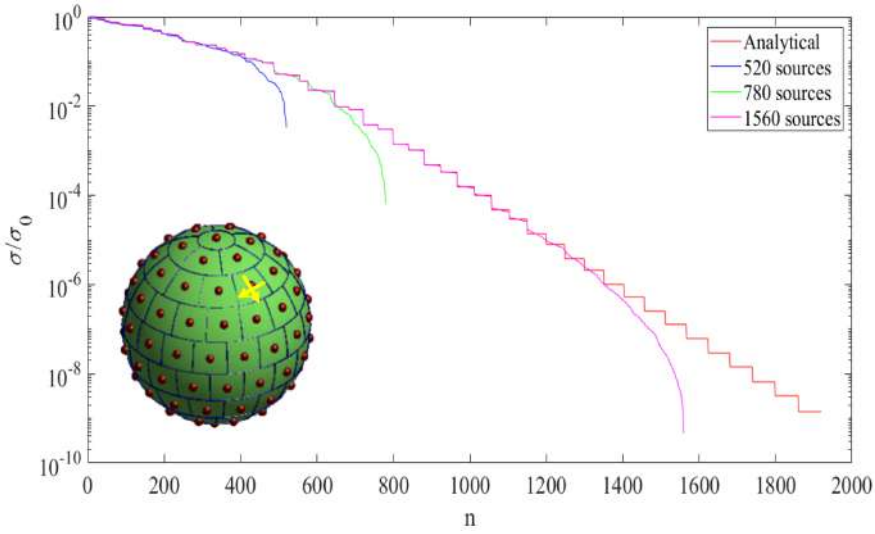

Figure 5.4: Singular values of the radiation operator for $r_{min} = 2\lambda$ and $R = 7\lambda$, showing the analytical solution and the solutions with different number of dipole sources.

5.3 DoF link with correlation parameter

Multiple-Input-Multiple-Output (MIMO) technology is a key player in new wireless communication, enhancing data speed and coverage while reducing signal fading caused by multipath propagation [74]. The Envelope Correlation Parameter (ECC) plays a crucial metric role for MIMO antenna system [75–77] due to the presence of more antennas both in transmission and reception. It quantifies the correlation between two antennas' radiation patterns, namely in a 2×2 MIMO antenna array system, indicating the degree of similarity or dissimilarity between their signal propagation characteristics. The ECC does not consider only of the radiation pattern shape, but also of the polarization, and the relative phase of the fields between two antennas. A low ECC signifies that the antennas' patterns are largely independent, minimizing the risk of interference and ensuring optimal performance in scenarios like MIMO systems. On the other hand, a high ECC value implies a greater likelihood of correlated radiation patterns, which can lead to undesirable signal overlaps and decreased system efficiency. The ECC value varies in a range from 0 to 1, this means that an ECC equal to indicates that the antennas are completely independent and a perfect performance for MIMO applications is achieved, while an ECC equal to 1 indicates that the antennas are highly correlated.
The Envelope Correlation Coefficient can be calculated through the radiation patter [78–82]as the following formula

$$\rho_{ECC} = \frac{\left| \iint_{4\pi} \boldsymbol{E}_1(\theta,\phi) \cdot \boldsymbol{E}_2(\theta,\phi) d\Omega \right|^2}{\iint_{4\pi} \boldsymbol{E}_1(\theta,\phi) \cdot \boldsymbol{E}_1^*(\theta,\phi) d\Omega \iint_{4\pi} \boldsymbol{E}_2(\theta,\phi) \cdot \boldsymbol{E}_2^*(\theta,\phi) d\Omega} \tag{5.23}$$

where $\boldsymbol{E}_1(\theta,\phi)$ and $\boldsymbol{E}_2(\theta,\phi)$ are the far-field radiation patterns for antenna 1 and antenna 2 in MIMO antenna system; the superscript $*$ states for the conjugate and the $\cdot$ denotes the

Hermitian product. In absence of losses, the ECC can be also expressed by a simple closed form equation that relates the scattering parameters [81] [82] of the elements in an antenna array configuration, namely for two antenna elements this equation becomes

$$\rho_{ECC} = \frac{\left|S_{11}^{*}S_{12} + S_{21}^{*}S_{22}\right|^{2}}{\left(1-|S_{11}|^{2}-|S_{21}|^{2}\right)\left(1-|S_{22}|^{2}-|S_{12}|^{2}\right)} \tag{5.24}$$

In the following eq. (5.23) will be used since from our analysis we have a complete knowdleg of the radiation pattern.

5.3.1 DoF-compliant beams and minimum ECC

In the calculation of the ECC (5.23) the spherical far-field radiation pattern, in (A.5a) of Appendix A, has been used. To examine the correlation between two patterns, we can consider two beams providing the maximum directivity. For this purpose we considered one beam directed along the broadside direction, i.e., $(\theta, \phi) = (0, 0)$, and as second beam rotated by an angle α wrt the broadside direction. In Figure 5.5 we can observe graphically the two beams: one in

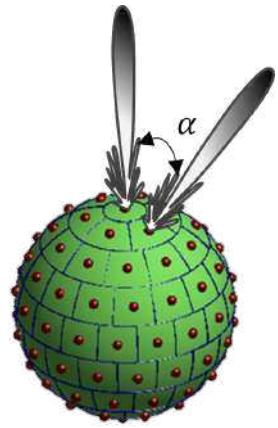

Figure 5.5: Graphical representation of the two beams rotated by an angle α.

the broadside direction and the other one rotated by α-angle. The two pattern associated to the broadside beam and to the rotated beam are $\boldsymbol{E}_1(\theta, \phi)$ and $\boldsymbol{E}_2(\theta - \alpha, \phi)$ with $(\theta, \phi) = (0, 0)$, respectively.

For a spherical source region, we can generate a certain number of independent beams with a certain maximum directivity. There exist a relationship between the N_{DoF} and the number of independent beams, namely

$$N_{beam} = N_{DoF}/2 \tag{5.25}$$

where the factor 2 at the denominator is due to the two polarizations (TE and TM).

In the previous Section the relationship between maximum directivity and the number of degrees of freedom has been emphasized. The maximum number of spherical waves (SWs) that contribute to the calculation of maximum directivity, denoted as N_{max}, can be approximated as kr_{min}, referring to equation (3.3). Consequently, from the previous expression in (5.25), the

number of beams, N_{beam}, can be expressed as $N_{beam} = (kr_{min})^2 + 2(kr_{min})$. Observing the Figure 5.5 we can define the angle α as

$$\alpha = \sqrt{\frac{4\pi}{N_{beam}}}[\text{rad.}] \tag{5.26}$$

Setting the dimension of the spherical region (kr_{min}), we can calculate from (5.25) the number of beams and from (5.26) the value of the angle α. In the following to cases are reported, the first one for non-super-directive antennas (without Q-bound) and the second one for super-directive antennas (with Q-bound); for both cases the $N_{max} = kr_{min} = 20$, with $N_{beam} = 440$. In Figure 5.6 the ECC for non-super-directive antenna is plotted versus the angle α, the vertical dashed line correspond to the angle $\alpha = 9.6828$ [Deg.] and ECC is $ECC[\%] = 0.45322$. Considering

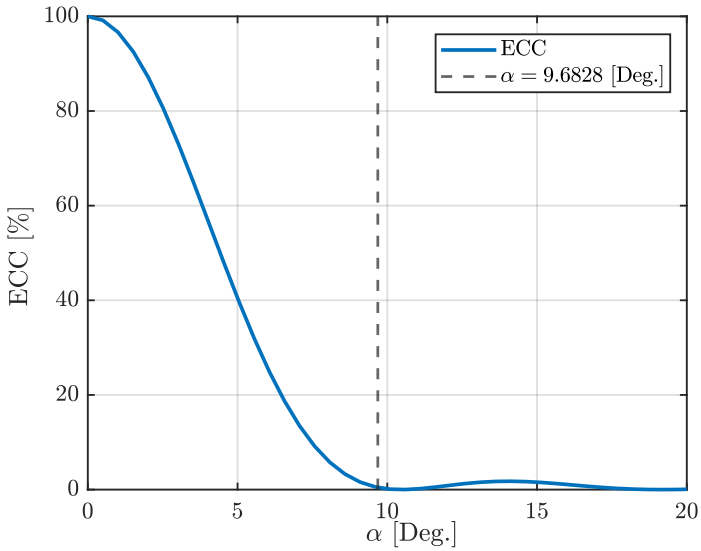

Figure 5.6: ECC for non-super-directive case varying the angle α; the vertical dashed line correspond to the angle α corresponding to a $kr_{min} = 20$.

the case of Q-bounded maximum directivity, the analytic formula (3.15) of Chapter 3 will be used. In Figure 5.7 the ECC is reported for different values of Q ($Q = 10$, $Q = 100$, $Q = 1000$). We can notice that the ECC shape are similar to each other, but the ECC approach zero value for different values of α angle. In Figure 5.8 the radiation patterns for the broadside direction beam, the rotated beam by the angle α, and the resulting one from the sum of the two has been reported, both for the non-super-reactive and Q-bounded with $Q = 100$ case. We can observe that the intersection between for the broadside direction beam and the rotated beam occurs at -3.5 dB. This result arises for non-super-directive case and for Q-bounded case. In Figure 5.8(a) is shown the results for non-super-directive case with $kr_{min} = 20$; the blue and the red curves approaches the maximum directivity of $D_{max} = 440 = 26.4345$ dB; while the green curve, which correspond to the sum of the two beams, does not reach the maximum directivity value: it shows a peak at $D_{max} = 25.4924$ dB (there is a difference of -1 dB). In Figure 5.8(b) is shown

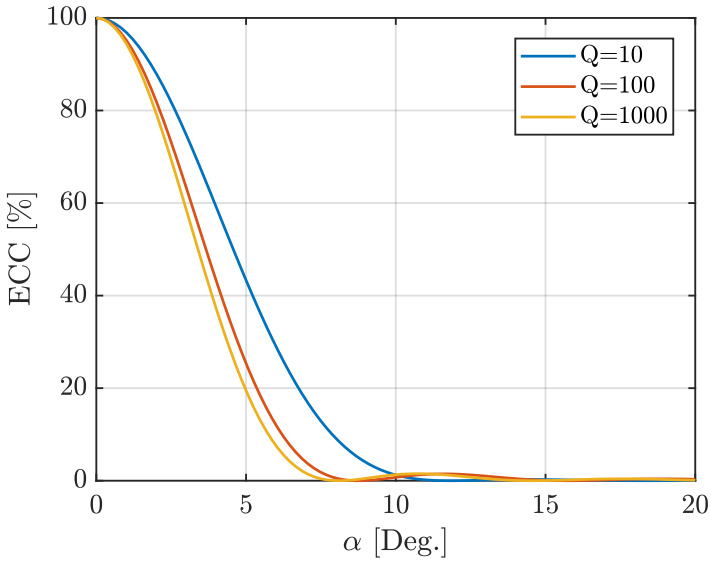

Figure 5.7: ECC for super-directive case varying the angle α for $kr_{min} = 20$ and for $Q = 10, 100, 1000$.

the results for the Q-bounded case with a $Q = 100$; the blue and the red curves approaches the maximum directivity of $D_{max} = 675 = 28.2930$ dB with $N_{max} = kr_{min} = 20$; while the green curve shows a peak at $D_{max} = 27.3052$ dB, exhibiting like the case for non-super-reactive antenna a difference of -1 dB.

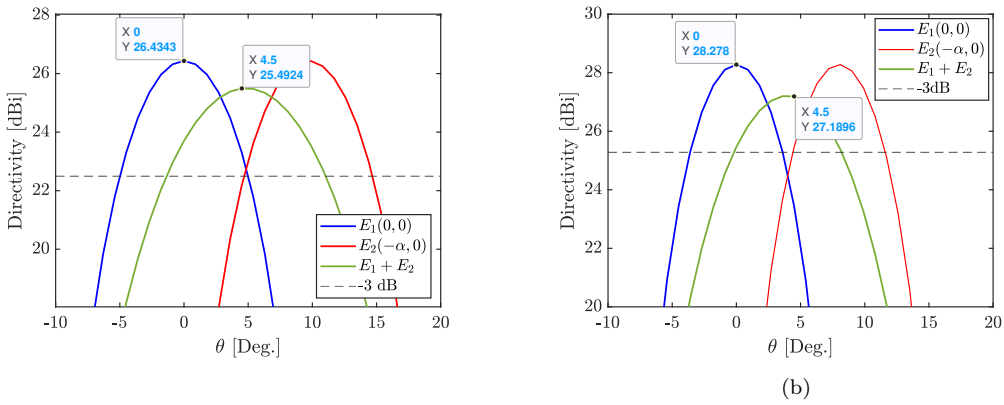

(b)

Figure 5.8: Radiation Pattern for non-super-directive case (a) and for Q-bounded case with $Q = 100$ (b), for $kr_{min} = 20$. The blue curves correspond to the radiation pattern for the broadside beams, the red curves correspond to the radiation pattern for the rotated beams, and the green one to the sum of the two beams. The blue and the red curves approaches the maximum directivity, while the green curve does not reach the maximum directivity value.

From Figure 5.8(a) and (b) we have seen that with only the sum of the two beams (the one in the broadside direction and the rotated one) we cannot reconstruct the maximum directivity value. It is because we should consider the four contiguous beams. For this purpose we should consider the beams rotated by an angle of $\pm\alpha/2$ along x and along y axis.
In Figure 5.9(a) are reported the radiation patterns for non-super-directive case with $kr_{min} = 20$. The blue curve corresponds to the broadside beam, while the red curve to the summation of the four rotate beams. The blue beam exhibits a peak at $D_{max} = 26.4343$ dB, and the red beam exhibits a peak at $D_{max} = 26.0898$ dB, observing a very small difference between the two maximum values. Then, as been predicted the maximum directivity value can be reconstructed summing the broadside beam with the four rotated beams. Similar results are also obtained for the Q-bounded case with $kr_{min} = 20$, as can be observed in Figure 5.9(b). In this case (for $Q = 100$) the blue beam exhibits a peak at $D_{max} = 28.278$ dB, and the red beam exhibits a peak at $D_{max} = 27.8642$ dB.

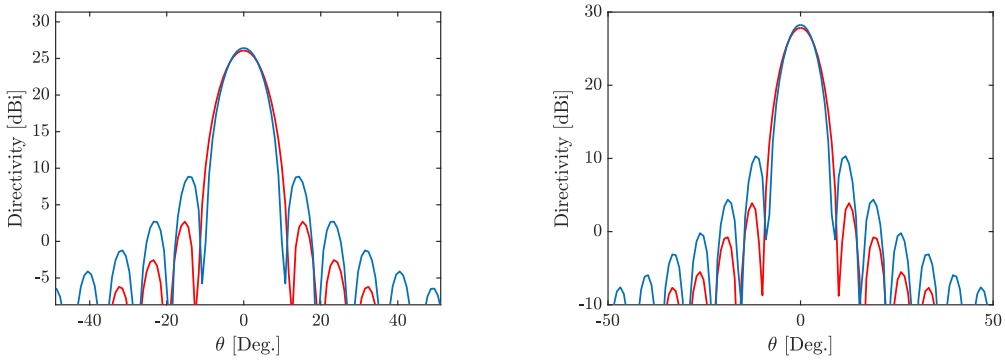

Figure 5.9: 2D radiation patterns of the broadside beam (blue curves) and of the sum of the four rotated beams (red curves), both for non-super-reactive case (a) and Q-bounded case with $Q = 100$ (b).

5.3.2 Universal ECC

The process of deriving the ECC results in a universal ECC, indicating with this terms that the ECC values remain unaffected by the size of the source. To provide evidence of this principle, we have examined two different source sizes case: $kr_{min} = 20$ and $kr_{min} = 25$. We conducted these investigations for both the non-super-directive case and the bandwidth-limited case. Our results reveal that the plots illustrating the ECC behavior exhibit minimal fluctuations based on the source size. To achieve this demonstration, we normalize the angle α by multiplying it by the square root of N_{beam}. The outcomes for the non-super-directive situation have been graphically depicted in Figure 5.10, while those for the bandwidth-limited scenario for $Q = 10, 100, 1000$ are shown in Figure 5.11. Figure 5.10 and Figure 5.11 highlight the robustness of the universal ECC across varying conditions and source sizes.

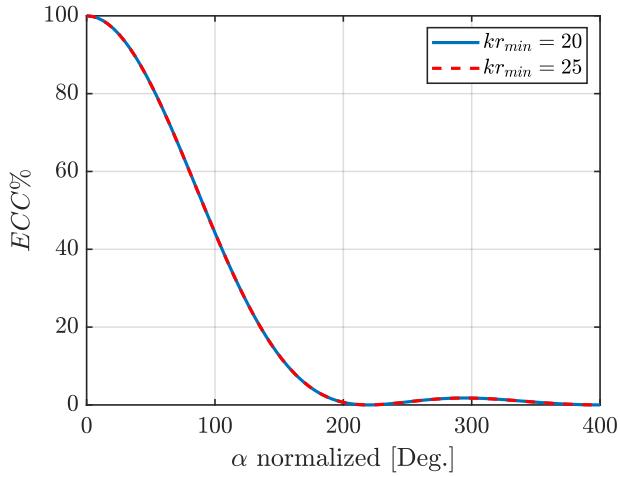

Figure 5.10: ECC % for the non-super-reactive case. The corresponding ECC is equal for two different values of the source size, i.e., $kr_{min} = 20$ (blue curve) and $kr_{min} = 25$ (red curve).

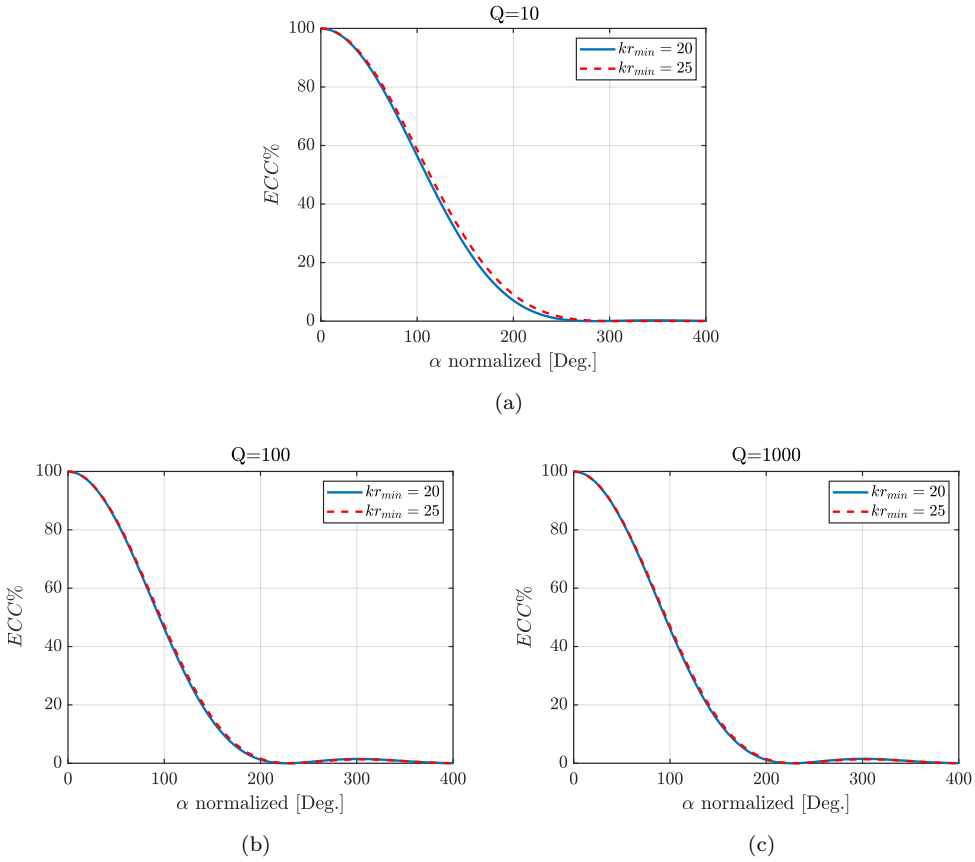

Figure 5.11: ECC % for the Q-bounded case with $Q = 10$ (a), $Q = 100$ (b), and $Q = 1000$ (c). The corresponding ECC is equal for two different values of the source size, i.e., $kr_{min} = 20$ (blue curves) and $kr_{min} = 25$ (red curves).

5.4 Conclusions

This Chapter has explored various fundamental properties related to the Degrees of Freedom of radiated fields. Additionally, a connection was established between the super-directivity and the number of degrees of freedom near the minimum sphere. Furthermore, this chapter delved into exploring the relationship between the Q-bounded maximum directivity, derived in Chapter 3, and the Envelope Correlation Parameter.

Chapter 6

Conclusions

Super-directive antennas, characterized by their unique features, are exceptionally well-suited for a various antennas applications. The versatility and advanced capabilities of super-directive antennas position them as a pivotal component in the future landscape of wireless communication. This crucial feature enhances signal strength during transmission and reception, proving particularly valuable in specific application scenarios. Their ability to focus the radiated signals is essential, particularly in space applications, making communication between spacecraft and Earth more efficient. As the demand for faster data transmission rises and frequency spectrum interference becomes more prevalent, researchers are increasingly directing their efforts toward advanced communication systems like 5G and beyond. Super-directive antennas are crucial for reducing signal loss at higher frequencies by densely packing many antennas into small spaces. Within the domain of Massive MIMO, super-directive antennas, particularly in densely packed arrays, make substantial contributions to achieving significant realized gains. Super-directive antennas are gaining attention due to their unique capabilities and potential applications in THz communication technologies. In the field of the Internet of Things (IoT), these antennas facilitate the high-data-rate services. This is especially advantageous in high-speed environments where maintaining stable connectivity is of importance. Furthermore, super-directive antennas find applications in radar systems, exploiting their high directivity and gain for precise target detection and tracking.

In conclusion, super-directive antennas have the potential to revolutionize various fields due to their ability to concentrate radiation in a selected preferential direction. Consequently, it contributes to an overall improvement in system efficiency and signal quality. Additional improvements extend to increased coverage at high frequencies and elevated power performance, allowing concentrated power allocation to provide users with a more reliable received signal. Exploring the intricate connection between antenna super-directivity and Degrees of Freedom in MIMO communication systems can result in enhanced channel capacity. Within this framework, the numbers of Degrees of Freedom represent the quantity of independent signals that can be transmitted and received through orthogonal field modes (characteristic modes). The simultaneous transmission of these signals without interference becomes feasible when one successfully excites and receives these independent modes, thereby augmenting the channel capacity.

Under these conclusions, it is crucial to delve into the potential of super-directive antennas. This PhD thesis aims to investigate potential physical limitations in connection with bandwidth, which are treated in terms of the quality factor. Furthermore, an exploration of the relationship between losses and the quality factor has been undertaken, providing additional insights into the practical realization of antennas. This effort has the purpose to offer a comprehensive understanding of the interplay between antenna characteristics, bandwidth constraints,

and losses, thereby contributing valuable information for practical implementation. The research journey embarked upon in this study has led to significant advancements and important findings, consolidating the understanding of antenna behavior in various contexts.

The upper limit on the directivity of self-resonant antennas that fit within a minimum sphere is determined for a given quality factor. This formulation is obtained by rigorously solving a convex problem and is expressed as a rapidly converging analytical series. The total quality factor, which is the inverse of the relative frequency bandwidth, is formulated by considering the quality factors of individual spherical waves. From the exact series, approximate closed-form formulas have been derived, exhibiting high accuracy in complementary ranges of the minimum circumscribed sphere's radius. These ranges encompass small antennas as well as intermediate to large antennas. Special emphasis is given to small antennas, where the solution is interpreted as a combination of dipolar and quadrupolar Huygens' source contributions with appropriate closed-form coefficients. This solution in this range provides continuity to the maximum directivity between 3 and 8 while maintaining a constant Q.

The investigation of the bound on super-gain assumes small losses in terms of surface resistance over the metalized surface of the minimum sphere circumscribing the antenna. The final closed-form formula shows that the maximum gain is obtained by a summation resembling Harrington's sum for maximum directivity, except that the expansion coefficients are weighted by the radiation efficiency of each spherical harmonic. The formulation is then generalized to the case of self-resonant antennas, providing a tighter bound for any losses. For small antennas, we offer a simple interpretation of the field corresponding to the maximum gain in terms of dipolar and quadrupolar source contributions, weighted by the appropriate efficiency, providing a physical insight into the phenomenon. The formulation is extended to account for a Q-bound, deriving a final series expression as a function of the loss resistance and the antenna electrical size. This expression seamlessly merges with the previously derived Q-bounded maximum directivity as losses tend to zero and converges to Q-unbounded maximum Gain for Q values that tend to very large values. The diagram in Figure 4.15 in Chapter 4 summarizes the presented formulas, specifying the validity region on the (Q, R_Ω)-plane. The diagram permits to visualize the validity region of the Q-bounded maximum directivity and Q-bounded maximum gain, reveling the range of losses and Q (bandwidth) values wherein the super-directivity corresponds to super-gain.

In the last Chapter, the relationship between the degrees of freedom of the field, the maximum directivity has been investigated. The relationship between the degrees of freedom and maximum directivity in antennas is a fundamental aspect of antenna theory. The concept is that the Degrees of Freedom of the field radiated by arbitrary sources within a minimum sphere must be twice the maximum directivity in (5.1). This relationship is applied to non-super-reactive antennas of any size that fit within a minimum sphere of any given radius [31]. The DoF of the field has been calculated for a limited angular region and for convex minimum region. Moreover, an analysis has been conducted on the relationship among the degrees of freedom, maximum directivity, and the envelope correlation parameter. This analysis has led to a broader understanding of this relationship, illustrating that it is independent of the source size.

Future Perspective

This Section explores the potential advancements and extensions of the current work, providing a foundation upon which new ideas can be built. It outlines the areas where the existing work can be improved or expanded, and suggests new directions for exploration based on the findings and limitations of the present study, are listed below:

- In Chapter 3, we focused on small antennas, interpreting the radiation pattern as a combination of dipolar and quadrupolar Huygens' sources. Investigating the potential of electrically small Huygens' source antennas could be a promising approach to achieving super-directive levels.

- The limitation on super-gain has been examined in terms of bandwidth constraints, expressed as the Q-factor. A more comprehensive limitation on super-gain could consider the constraints introduced by losses, which involves evaluating the total efficiency of the system and imposing a-priori limitations on it. This would establish an efficiency bound on super-gain.

- In Chapter 3and Chapter 4 the bounds on super-directivity and super-gain are analyzed in terms of Q-factor. Alternatively, it is also possible to restrict the number of harmonics that can be excited over the minimum sphere based on the degrees of freedom of the field. The concept of degrees of freedom, meanwhile, offers a new perspective on antenna design. It refers to the number of independent parameters that can be adjusted in a system. In the context of antennas, this could include aspects such as the shape, size, and orientation of the antenna elements. Understanding and manipulating these degrees of freedom can lead to more flexible and efficient antenna designs. The theory of Degrees of Freedom (DoF), which is linked to super-directivity, could be expanded into the theory of DoF free ports architecture. This would enable the maximization of usable DoF for large array antennas.

- The results presented here open new perspectives on the design of intermediate to small antennas. These insights can be extended to the arbitrary shape of the minimum surface enveloping the sources, leading to better antenna bounds.

List of Pubblications

Conference Papers

- C. Yepes, L. Passalacqua, A. Murillo Barrera, E. Martini, and, S. Maci, "Frequency-Bandwidth Dependent Degrees of Freedom as a Bound of Super-Directivity", *URSI GASS 2021*, Rome, Italy, 28 August - 4 September 2021.
- L. Passalacqua, C. Yepes, E. Martini, A. Murillo Barrera, and S. Maci, "Frequency-Bandwidth Dependent Degrees of Freedom as a Bound of Super-Directivity", *IEEE AP-S/URSI 2021*, Marina Bay Sands, Singapore, 4-10 December 2021.
- L. Passalacqua, C. Yepes, E. Martini, and S. Maci, "Frequency-Bandwidth Dependent Degrees of Freedom as a Bound of Super-Directivity", *EuCAP 2022*, Madrid, Spain, 2022.
- L. Passalacqua, C. Yepes, E. Martini, and S. Maci, "Frequency-Bandwidth Constrained Super-Directivity and Relationship with Degrees of Freedom", IEEE AP-S/URSI 2022, Denver, Colorado, USA, 10-15 July 2022
- L. Passalacqua, E. Martini, and S. Maci, "Bound on Q-Limited Super-Gain", *EuCAP 2023*, Florence, Italy, 2023.
- L. Passalacqua, C. Yepes, A. Murillo Barrera, E. Martini, and S. Maci, "Degrees of Freedom of the Field through SVD-based approach applied to a Box-shaped Source Region", *APS-URSI 2023*, Portland, Oregon, USA, 23-28 July 2023.

Journal Papers

- L. Passalacqua, C. Yepes, E. Martini, and S. Maci,"Q-Bounded Maximum Directivity of Self-Resonant Antennas", *IEEE Transactions on Antennas and Propagations*, doi: 10.1109/TAP.2023.3324418.
- L. Passalacqua, C. Yepes, A. Murillo, B. Biscontini, E. Martini and S. Maci, "Maximum Gain of Lossy Antennas Without and With Q-bounds," *IEEE Transactions on Antennas and Propagation*, doi: 10.1109/TAP.2024.3358977.

Appendix A

Spherical Wave Function

This Appendix contains the general expression for the Spherical Wave Functions of fundamental importance to understand the presented composition. Here we adopt the Hansen's notation in [61], except for a different time dependency (which is here $exp(j\omega t)$), and for the notations of the expansion coefficients, we denote the letter C in place of Q, to avoid confusion with the Q-factor. In this notation, the superscript "3" corresponds to the spherical Hankel outgoing (second-type) r-dependent function. The polar index n ($n = 1, 2, ..., N$) refers to the order of the Hankel function and the index m refers to the azimuthal angular wave number ($m = -N, ..., 0, ..., N$). The subscript $s = 1, 2$ denotes TE and TM polarization with respect to r, respectively.

$$\begin{aligned}\boldsymbol{F}^{(c)}_{1,m,n}(r,\theta,\phi) = c_{m,n}\Big\{ & R^{(c)}_{1,n}(kr)\frac{-jm\bar{P}^{|m|}_n(\cos\theta)}{\sin\theta}e^{-jm\phi}\hat{\theta}+ \\ & - R^{(c)}_{1,n}(kr)\frac{d\bar{P}^{|m|}_n(\cos\theta)}{d\theta}e^{-jm\phi}\hat{\phi}\Big\}\end{aligned} \tag{A.1a}$$

$$\begin{aligned}\boldsymbol{F}^{(c)}_{2,m,n}(r,\theta,\phi) = c_{m,n}\Big\{ & \frac{n(n+1)}{kr}R^{(c)}_{1,n}(kr)\bar{P}^{|m|}_n(\cos\theta)e^{-jm\phi}\hat{r}+ \\ & + R^{(c)}_{2,n}(kr)\frac{d\bar{P}^{|m|}_n(\cos\theta)}{d\theta}e^{-jm\phi}\hat{\theta}+ \\ & + R^{(c)}_{2,n}(kr)\frac{-jm\bar{P}^{|m|}_n(\cos\theta)}{sin\theta}e^{-jm\phi}\hat{\phi}\Big\}\end{aligned} \tag{A.1b}$$

where $\bar{P}^{|m|}_n(\cdot)$ is the normalized associated Legendre function, and

$$c_{m,n} = \frac{1}{\sqrt{2\pi}}\frac{1}{\sqrt{n(n+1)}}\Big(-\frac{m}{|m|}\Big)^m. \tag{A.2}$$

The $R^{(c)}_{s,n}(kr)$ are the radial functions:

$$R^{(c)}_{s,n}(kr) = \begin{cases} z^{(c)}_n(kr) & s = 1 \\ \frac{1}{kr}\frac{d}{d(kr)}\big[krz^{(c)}_n(kr)\big] & s = 2, \end{cases} \tag{A.3}$$

with

$$z^{(c)}_n(kr) = \begin{cases} j_n(kr) & c = 1 \\ n_n(kr) & c = 2 \\ h^{(2)}_n(kr) = j_n(kr) - jn_n(kr) & c = 3 \\ h^{(1)}_n(kr) = j_n(kr) + jn_n(kr) & c = 4. \end{cases} \tag{A.4}$$

The electric and the magnetic fields in terms of spherical wave can be expressed as

$$\boldsymbol{E}(r,\theta,\phi) = k\sqrt{\zeta} \sum_{c,s,m,n} C^{(c)}_{s,m,n} \boldsymbol{F}^{(c)}_{s,m,n}(r,\theta,\phi) \tag{A.5a}$$

$$\boldsymbol{H}(r,\theta,\phi) = \frac{jk}{\sqrt{\zeta}} \sum_{c,s,m,n} C^{(c)}_{s,m,n} \boldsymbol{F}^{(c)}_{s,m,n}(r,\theta,\phi) \tag{A.5b}$$

The radiated power is

$$P_r = \frac{1}{2} \sum_{s,m,n} \left| C^{(3)}_{s,m,n} \right|^2 \tag{A.6}$$

The far-field can be expressed as an asymptotic form of $\boldsymbol{F}^{(c)}_{1,m,n}(r,\theta,\phi)$ and $\boldsymbol{F}^{(c)}_{2,m,n}(r,\theta,\phi)$ as kr tends to infinity, where the r-dependence is cancelled, namely

$$\boldsymbol{K}_{s,m,n}(\theta,\phi) = \lim_{kr\to\infty} \left[\sqrt{4\pi} kr e^{jkr} \boldsymbol{F}^{(3)}_{s,m,n}(r,\theta,\phi) \right] \tag{A.7}$$

In the text, we will frequently encounter the use of the index i which summarizes the triplet of indices s, m, n as

$$i = 2[n(n+1) + m - 1] + s \tag{A.8}$$

where $i = 1, 2, ..., J$, with $J = 2N(N+2)$.

Appendix B

Equivalent Currents using SWs

The objective of this appendix chapter is to find the spherical wave expansion and radiation resistance of a general distribution of currents on the minimum sphere enclosing all the sources, used for the derivation of the analytical closed-form formulas in Chapter 3 and 4. In both the procedure we will apply the equivalence principle to the minimum sphere surface S. From the equivalence principle it is known that we can replace an arbitrary set of source by equivalent currents distributed over a virtual closed surface S enclosing all the real sources. This permits to have the same field outside the minimum sphere surface S.
Two cases will be described: one considering only electric currents which radiate in the free-space; one considering a magnetic currents which radiate in presence of a lossy conducting material.

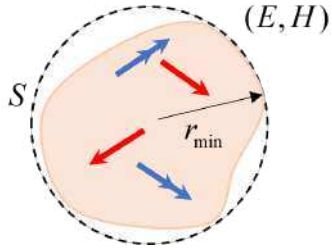

Figure B.1: Graphical representation of the Equivalent Theorem. The sources can be enclosed by a minimum surrounding sphere S of radius r_{min}.

B.1 Equivalent Currents Derivation in presence of electric currents

The equivalent problem in Figure B.1 can be replaced with the one in Figure B.2. This implies field and reactive energy different from zero inside the sphere, thus requiring an internal compensation of energy at resonance. The equivalent electric currents of the equivalent problem in Figure B.2 is written as

$$\boldsymbol{J} = \frac{jk}{\sqrt{\zeta}} \sum_{s,m,n} C_{s,m,n} \hat{r} \times \boldsymbol{F}^{(3)}_{3-s,m,n}(r,\theta,\phi) \tag{B.1}$$

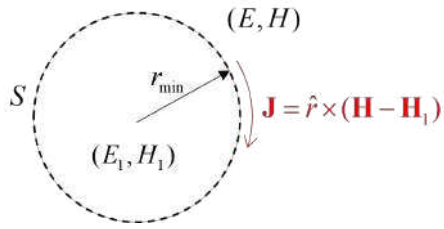

Figure B.2: Graphical representation of the Equivalent Theorem considering only a set of electric currents $\boldsymbol{J}$.

These currents can be conveniently represented through the transverse (θ, ϕ)-dependent orthonormal basis functions, i.e.,

$$\boldsymbol{f}_i(\theta,\phi) = \frac{\boldsymbol{T}_i(\theta,\phi)}{r_{min}} \tag{B.2}$$

where $\boldsymbol{T}_i(\theta,\phi)$ is defined through the factorization of the spherical wave harmonics [61] as

$$\hat{r} \times \boldsymbol{F}^{(c)}_{s,m,n}(r,\theta,\phi) = R^{(c)}_{s,n}(kr)\hat{r} \times \boldsymbol{T}_{s,m,n}(\theta,\phi) \tag{B.3}$$

In (B.2) we have introduced the index i which renumbers the tern of the indexes s, m, n in a single index $i = 2[n(n+1)+m-1]+s$; when possible, we will use it to compact the notation. The function $\boldsymbol{T}_{s,m,n} \equiv \boldsymbol{T}_i$ are the (θ,ϕ) dependent transverse-to-r function in the spherical wave factorization. With the choice of the normalization adopted, the basis functions $\boldsymbol{f}_i$ are orthonormal over the minimum surface; this means that the following normalization it is satisfied

$$\iint_S \boldsymbol{f}_i \cdot \boldsymbol{f}_j^* dS = \delta_{i,j} \tag{B.4}$$

since (A1.69 in [61])

$$\begin{aligned} &\iint_S \boldsymbol{f}_i \cdot \boldsymbol{f}_j^* \, dS = \\ &= \int_0^{2\pi}\int_0^{\pi} \frac{\boldsymbol{T}_{s,m,n}(\theta,\phi)\cdot \boldsymbol{T}^*_{\sigma,\mu,\nu}(\theta,\phi)}{r^2_{min}} r^2_{min}\sin\theta \, d\theta \, d\phi = \\ &= \delta_{s,\sigma}\delta_{m,\mu}\delta_{n,\nu} \end{aligned} \tag{B.5}$$

Moreover, since the orthogonality, the i-th current SW basis function radiates a i-th field only, which is related with the SW current by a coefficient obtained by projection given in eq.A1.77 of [61], namely

$$\begin{aligned} C_i = (-1)^{m+1} k\sqrt{\zeta} R^{(1)}_{s,n}(kr_{min}) \int_0^{2\pi}\int_0^{\pi} \boldsymbol{T}_{s,-m,n}(\theta,\phi)\cdot \boldsymbol{f}_i(\theta,\phi) \\ r_{min}\sin\theta \, d\theta \, d\phi = -r_{min} k\sqrt{\zeta} R^{(1)}_{s,n}(kr_{min}) \end{aligned} \tag{B.6}$$

We note that the coefficient Q_i in (B.6) does not depend on the azimuthal index m, but only on the polar index n and on the polarization index s. The electric field on top of the basis SW current $\boldsymbol{f}_i$ in direction (r_{min},θ,ϕ) can be obtained as

$$\boldsymbol{E}_i(r_{min},\theta,\phi) = -r^2_{min}k^2\zeta R^{(1)}_{s,n}(kr_{min}) R^{(3)}_{s,n}(kr_{min}) \boldsymbol{T}_{s,m,n}(\theta,\phi) \tag{B.7}$$

Therefore, for a current of amplitude I_i, the radiated power can be obtained by

$$\begin{aligned} P_r^{(i)} &= \frac{1}{2}\Re\left\{ \iint_S \boldsymbol{E}_i(r_{min},\theta,\phi)\cdot\boldsymbol{J}_i^*(r_{min},\theta,\phi)\,dS \right\} = \\ &= \frac{1}{2}\Re\left\{ \iint_S C_i R_{s,n}^{(3)}(kr_{min}) I_i I_i^* \boldsymbol{f}_i \boldsymbol{f}_i^*\,dS \right\} \end{aligned} \tag{B.8}$$

where the current density $\boldsymbol{J}_i$ is $\boldsymbol{J}_i = I_i\boldsymbol{f}_i$, with I_i current coefficient. Equaling eq.(B.8) with the general definition of the radiated power $P_r^{(i)} = \delta_{i,j}\frac{1}{2}\sum_j R_{rad}^{(i)}\left|I_i\right|^2$, we can derive the expression for the radiation resistance,

$$R_{rad,n}^{(s)} = \begin{cases} -r_{min}^2 k^2 \zeta \left[R_{s,n}^{(1)}(kr_{min})\right]^2 & \text{for } i=j \\ 0 & \text{for } i\neq j \end{cases} \tag{B.9}$$

B.2 Equivalent Currents derivation in presence of electric and magnetic currents

Applying the Love's formulation of the equivalence theorem (Figure B.3-(a)) to the original problem in Figure B.1. In this configuration the internal fields is equal to zero; the external field is the same as that provided by magnetic currents on a perfect conducting sphere (Schelkunoff's formulation) (Figure B.3)-(a)). The equivalent electric and magnetic currents are written as

$$\boldsymbol{J} = \frac{jk}{\sqrt{\zeta}}\sum_{s,m,n} C_{s,m,n}\hat{r}\times\boldsymbol{F}_{3-s,m,n}^{(3)}(r,\theta,\phi) \tag{B.10a}$$

$$\boldsymbol{M} = k\sqrt{\zeta}\sum_{s,m,n} C_{s,m,n}\boldsymbol{F}_{s,m,n}^{(3)}(r,\theta,\phi)\times\hat{r} \tag{B.10b}$$

These currents can be conveniently represented through same the transverse (θ,ϕ)-dependent orthonormal basis functions defined in (B.2), which have the same orthogonality properties illustrated in (B.4) and (B.5). Using (B.2), the expression of the magnetic and electric current densities in (B.10) can be rewritten as

$$\boldsymbol{J} = \sum_i I_i\boldsymbol{f}_i(\theta,\phi) \tag{B.11a}$$

$$\boldsymbol{M} = \sum_i M_i\boldsymbol{f}_i(\theta,\phi)\times\hat{r} \tag{B.11b}$$

with coefficients

$$I_i = \frac{jkr_{min}}{\sqrt{\zeta}}(-1)^s C_i R_{3-s,n}^{(3)}(kr_{min}) \tag{B.12a}$$

$$M_i = kr_{min}\sqrt{\zeta}(-1)^s C_i R_{s,n}^{(3)}(kr_{min}) \tag{B.12b}$$

Since the orthonormality of the basis functions the current coefficients I_i represents the average integral over the minimum sphere of the squared electric currents of the i-th spherical mode, i.e.,

$$|I_i|^2 = \iint_S |\boldsymbol{J}_i|^2\,dS \tag{B.13}$$

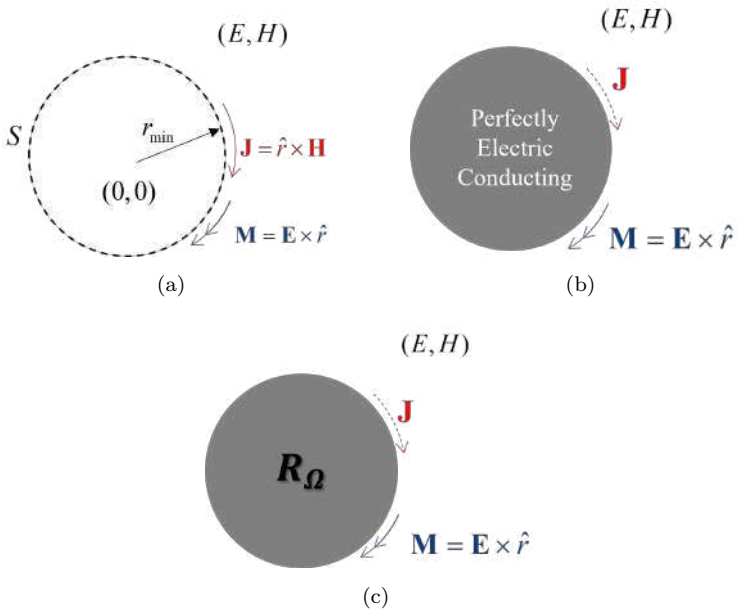

Figure B.3: (a) Graphical representation of Love's formulation of the equivalent currents; (b) the magnetic currents radiating on a perfect conducting sphere; (c) the magnetic currents radiate in presence of lossy conductor material with resistivity R_Ω.

where $\boldsymbol{J}_i = I_i \boldsymbol{f}_i$.
From eq.(B.12a), setting an unitary coefficient I_i we can derive the expression of the field coefficients C_i, namely

$$C_i = \left| (-1)^s \frac{jk}{\sqrt{\zeta}} R^{(3)}_{3-s,n}(kr) \right|^{-1} \tag{B.14}$$

Therefore, the radiate power can be obtained as

$$P_r = \frac{1}{2} \sum_i |C_i|^2 |I_i|^2 = \frac{1}{2} \sum_i \left| (-1)^s \frac{jk}{\sqrt{\zeta}} R^{(3)}_{3-s,n}(kr) \right|^{-1} |I_i|^2 \tag{B.15}$$

Equaling eq.(B.15) with the general definition of the radiated power $P_r^{(j)} = \delta_{i,j} \frac{1}{2} \sum_j R^{(i)}_{rad} |I_i|^2$, we can derive the expression for the radiation resistance,

$$R^{(s)}_{rad,n} = \begin{cases} \zeta (kr_{min})^{-2} \left| R^{(3)}_{3-s,n}(kr_{min}) \right|^{-2} & \text{for } i = j \\ 0 & \text{for } i \neq j \end{cases} \tag{B.16}$$

The problem depicted in Figure B.3(a) is equivalent to the one shown in Figure B.3(b). This equivalence arises because it is possible to assume that only magnetic currents radiate in the presence of a Perfect Electric Conductor (PEC) material. Due to the presence of the PEC material, electric currents are supported. This latter equivalent problem can also be replaced by the one in Figure B.3(c), where magnetic currents radiate in the presence of a lossy conductor

with resistivity for the square surface denoted as R_Ω. This assumption is made under the condition that the electric currents induced on the conductor by the magnetic forced currents will not change significantly compared to the currents on a PEC.

Appendix C

Quality Factor

The Q-factor is defined as the ratio between the time-average stored energy (W_e or W_m) and radiated energy P_r, i.e.,

$$Q = \begin{cases} \frac{2\omega W_e}{P_r} & W_e > W_m \text{ (capacitive antenna)} \\ \frac{2\omega W_m}{P_r} & W_m > W_e \text{ (inductive antenna)} \end{cases} \tag{C.1}$$

In general, the Q-factor can be interpreted as the reciprocal of fractional bandwidth $BW = 1/Q$ for a sufficient value of Q ($Q > 10$) [21] [14]. If the antennas is at a self-resonant state there is a balancing between the electric and the magnetic stored energies, this means that $W_e = W_m$ at resonance. Hence, when the self-resonant condition is fulfilled, the Q-factor of the system can be rewritten as

$$Q = \frac{2\omega W_e}{P_r} = \frac{2\omega W_m}{P_r} \tag{C.2}$$

The calculation of the stored energy of a general spherical wave expansion is a debated topic [22] [28] [60] [83] [84]. Essentially, the most used approaches are the ones provided by Chu [25], Collin and Rothschild [21] and Fante [85]. Fante generalized to the case of arbitrary field internal to the minimum sphere in [84]. In [21], the quality factor of each individually tuned spherical wave is defined for a unit power as

$$Q'_i = \begin{cases} 2\omega W_{e,i} & \text{(TM modes)} \\ 2\omega W_{m,i} & \text{(TE modes)} \end{cases} \tag{C.3}$$

In [85], Fante introduced also additional terms needed for the calculation of the Q-factor of a generic antenna

$$Q''_i = \begin{cases} 2\omega W_{m,i} & \text{(TM modes)} \\ 2\omega W_{e,i} & \text{(TE modes)} \end{cases} \tag{C.4}$$

The exact expressions of Q'_i and Q''_i defined by Fante in [85] are reported below

$$\begin{aligned} Q'_n = {} & kr_{min} - \left|h_n(kr_{min})\right|^2 \left[\frac{(kr_{min})^3}{2} + kr_{min}(n+1)\right] + \\ & - \frac{(kr_{min})^3}{2}\left|h_{n+1}(kr_{min})\right|^2 + (kr_{min})^2 \frac{2n+3}{2} \cdot \\ & \cdot \left[j_n(kr_{min}) j_{n+1}(kr_{min}) + y_n(kr_{min}) y_{n+1}(kr_{min})\right] \end{aligned} \tag{C.5}$$

$$\begin{aligned} Q''_n = {} & kr_{min} - \frac{(kr_{min})^3}{2}\Big[\left|h_n(kr_{min})\right|^2 - \\ & j_{n-1}(kr_{min}) j_{n+1}(kr_{min})\Big] \end{aligned} \tag{C.6}$$

where $h_n(kr_{min})$, $j_n(kr_{min})$, and $y_n(kr_{min})$ are the spherical first type Hankel, Bessel and Neumann functions of order n, respectively. It is noted that they are independent form the azimuthal index m.
Using the SW expansions the total quality factor can be written as:

$$Q_{tot} = \begin{cases} \frac{\left(\sum_{TM} |C_i'|^2 Q_i' + \sum_{TE} |C_i''|^2 Q_i''\right)}{\sum_i |C_i'|^2 + |C_i''|^2} & W_e > W_m \\ \frac{\left(\sum_{TE} |C_i''|^2 Q_i' + \sum_{TM} |C_i'|^2 Q_i''\right)}{\sum_i |C_i'|^2 + |C_i''|^2} & W_m > W_e \end{cases} \tag{C.7}$$

where C_i' and C_i'' are the coefficients of the TM and TE modes, respectively.
Under condition of self-resonance, it turn out [85] that TE and TM modes with the same indices have coefficients of equal magnitude, so that the two summations at both numerators and denominators reduce to a single summation, i.e.,

$$Q_{tot} = \frac{\sum_n |C_n|^2 Q_n}{\sum_n |C_n|^2} \tag{C.8}$$

where C_n are the field expansion coefficients for maximum directivity $(C_i' + C_i'')$ and the Q_n, introduced by Fante in [85], are

$$Q_n \equiv \frac{1}{2}(Q_n' + Q_n'') \tag{C.9}$$

Expression in (C.8) depends only on the index n since the coefficients' magnitude is considered, surpassing the dependence on the azimuthal index m. The adoption of (C.8) automatically

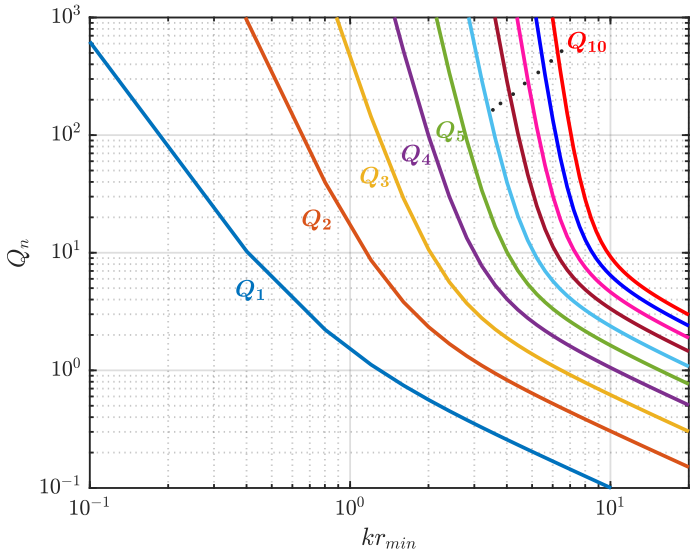

Figure C.1: Fante's Q_n coefficients. The used log-log scale emphasizes the different behaviour of Q_n with corner at $kr_{min} \approx n$.

assumed a self-balancing of reactive energy. Therefore, the limit that we derive in the following

adopting (C.8) *is relevant to self-resonant antennas*, namely antennas where you should not provide energy through an external circuit to achieve the resonance.
In Figure C.1 the Fante's Q_n are plotted as a function of kr_{min} for some values of n. The asymptotic behaviour for small values of kr_{min} has been explored in [83], which is very fast-growing function for decreasing kr_{min} when $kr_{min} < n$; in the following we extend the behaviour also for large values of kr_{min}, namely

$$Q \sim \begin{cases} \frac{n}{2}\left(\frac{(2n)!}{n!2^n}\right)^2 \frac{1}{(kr_{min})^{2n+1}} & \text{for } kr_{min} \to 0 \\ a_n (kr_{min})^{-1} & \text{for } kr_{min} \to \infty \end{cases} \tag{C.10}$$

where $a_n = a_{n-1} + n$ with $a_0 = 1$ by definition. The Q-factors show a rapid change of behaviour from kr_{min}^{-1} to $kr_{min}^{-(2n+1)}$ for $kr_{min} \approx n$. It is important to note the Fante's Q_n for $n = 1$ and $n = 2$ give *exactly*

$$Q_1 \equiv \frac{1}{2(kr_{min})^3} + \frac{1}{kr_{min}} \tag{C.11}$$

$$Q_2 \equiv \frac{9}{(kr_{min})^5} + \frac{9}{2(kr_{min})^3} + \frac{3}{kr_{min}} \tag{C.12}$$

which are related to the Chu-limit.

Appendix D

Discretization of the radiation operator

Consider an arbitrary set of impressed currents ($\boldsymbol{J_i}$,$\boldsymbol{M_i}$) and scatterers enclosed by a fictitious surface S with outward normal, surrounded by a homogeneous medium, that for the sake of simplicity we will assume to be free space Figure D.1(a). Let us denote by ($\boldsymbol{E}$,$\boldsymbol{H}$), the electromagnetic field radiated by this system. We can consider that a spherical surface of radius r_{min} encapsulates these sources. This sphere has been denoted in the previous paragraph as minimum sphere. Since our intention is to extend the concept to a general minimum surface, here the sources are supposed to be inside a minimum surface S which is inside the minimum sphere. Consider the equivalent problem in Figure D.1(b), where the interior of S is source-free and filled by free space and a set of equivalent currents ($\boldsymbol{J_{eq}}$,$\boldsymbol{M_{eq}}$) is distributed on S. Assume that these currents radiate in the external region the original field ($\boldsymbol{E}$,$\boldsymbol{H}$) and in the internal region an arbitrary field ($\boldsymbol{J_1}$,$\boldsymbol{M_1}$) satisfying the homogeneous Maxwell's equations. By uniqueness theorem, the equivalent currents ($\boldsymbol{J_{eq}}$,$\boldsymbol{M_{eq}}$) are unequivocally defined in such a way to compensate for the discontinuity of the tangential components of the fields, i.e,

$$\boldsymbol{J}_{eq} = \hat{n} \times (\boldsymbol{H} - \boldsymbol{H}_1) \tag{D.1a}$$

$$\boldsymbol{M}_{eq} = (\boldsymbol{E} - \boldsymbol{E}_1) \times \hat{n}. \tag{D.1b}$$

We will assume to choose an internal field such that the equivalent magnetic currents $\boldsymbol{M_{eq}}$ vanish [86]. In such a case, (D.1) implies that the tangential component of the electric field across S must be continuous:

$$\boldsymbol{E}_1 \times \hat{n} = \boldsymbol{E} \times \hat{n}. \tag{D.2}$$

Thus, the internal electromagnetic field ($\boldsymbol{E}_1$,$\boldsymbol{H}_1$) is the solution of the homogeneous Maxwell's equations in the internal region with boundary conditions $\boldsymbol{E}_1 \times \hat{n} = \boldsymbol{E} \times \hat{n}$. For the uniqueness theorem, this solution is unequivocally defined unless resonant solutions are present in S. By assuming vanishingly small losses inside S, the solution is unique.
We notice that this is an unusual version of the Equivalence theorem, that is normally not used in method of moments (MoM), but it will be useful here. Notice also that the electric currents generate inside the surface a non-zero field, in contrast with what happens in Love formulation of the equivalence theorem.
Using the equivalent problem of Figure D.1(c) we can define the electric field outside the surface S as

$$\boldsymbol{E}(r) = \iint_S \underline{\underline{\boldsymbol{G}}}_E^{(J)}(\boldsymbol{r}, \boldsymbol{r'}) \boldsymbol{J}(r')\, dr' = \boldsymbol{L}[\boldsymbol{J}] \tag{D.3}$$

where $\underline{\underline{\boldsymbol{G}}}^{(J)}$ is the Green's Function (GF) of free space if no other object is present around. If additional boundary conditions are present outside the surface (see Figure D.2(a)) the Green's

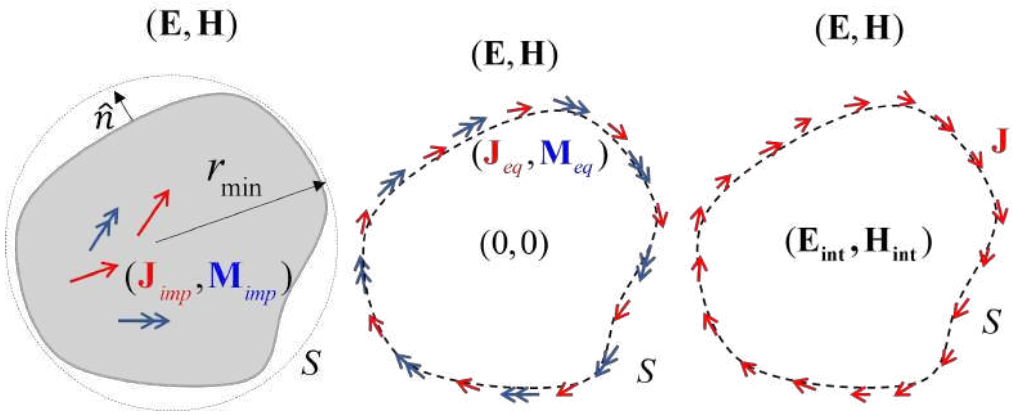

Figure D.1: (a) Original problem, (b) Love's equivalent problem, and (c) the equivalent problem with only electric currents.

function should be split in two parts, as

$$\underline{\underline{\boldsymbol{G}}}_E^J(\boldsymbol{r},\boldsymbol{r'}) = \underline{\underline{\boldsymbol{G}}}_E^{(inc)}(\boldsymbol{r},\boldsymbol{r'}) + \underline{\underline{\boldsymbol{G}}}_E^{(s)}(\boldsymbol{r},\boldsymbol{r'}) \tag{D.4}$$

where $\underline{\underline{\boldsymbol{G}}}_E^{(inc)}(\boldsymbol{r},\boldsymbol{r'})$ is the GF of the free space and $\underline{\underline{\boldsymbol{G}}}_E^{(s)}(\boldsymbol{r},\boldsymbol{r'})$ takes into account the additional boundary conditions outside the object. Assuming to observe the field in the far region (see Figure D.2(b)) for both the radiating sources and the objects around, we approximate the radiation integral in the following form

$$\underline{\underline{\boldsymbol{G}}}_E^J(\boldsymbol{r},\boldsymbol{r'}) \approx jk\zeta\frac{e^{-jkr}}{4\pi r}\left[\underline{\underline{\boldsymbol{g}}}_E^{(s)}(r-\hat{\boldsymbol{r}}\cdot\boldsymbol{r'},\boldsymbol{r'}) + \hat{\boldsymbol{r}}\times(\hat{\boldsymbol{r}}\times\underline{\underline{\mathbf{1}}})e^{-jk\hat{\boldsymbol{r}}\cdot\hat{\boldsymbol{r'}}}\right] \tag{D.5}$$

where $\underline{\underline{\mathbf{1}}}$ is the unitary dyad, $\hat{\boldsymbol{r}}$ is the unit radial vector of the spherical coordinate, and r is the distance of the observation point from the origin of the reference system inside the minimum surface.

In order to discretize the radiation operator in (D.3), the unknown $\boldsymbol{J}(r')$ is expanded in terms of arbitrary basis functions $f_n^{(i)}(\boldsymbol{r'})$, i.e,

$$\boldsymbol{J}(\boldsymbol{r'}) = \sum_{n=1}^{N}\left[I_n^{(1)}f_n^{(1)}(\boldsymbol{r'})\boldsymbol{p}_n^{(1)} + I_n^{(2)}f_n^{(2)}(\boldsymbol{r'})\boldsymbol{p}_n^{(2)}\right] \tag{D.6}$$

where $\boldsymbol{p}_n^{(i)}$; $i = 1,2$ are two orthogonal directions of the basis function over the surface and $f_n^{(i)}(\boldsymbol{r'})$ are scalar basis functions with dimension $length^{-1}$ non-zero over a sub-wavelength area ΔS_n over the surface S, and zero elsewhere. The functions are normalized in such a way that

$$\iint_{\Delta S_n} f_n^{(i)} f_n^{(i)^*}\, dS = 1 \tag{D.7}$$

$$\iint_{\Delta S_n} f_n^{(i)}\, dS = \delta_n \tag{D.8}$$

The number N of basis function in (D.6) should be much larger than the expected number of degrees of freedom, namely $N >> N_{DoF}$. The best choice for arbitrary surface could be sub-wavelength functions with triangular support, like Rao-Wilton-Glisson basis functions [87]. However, since here we are not dealing with the near field, even simple pulse type function with rectangular support would work (i.e., it not is not strictly necessarily, even if suggested, that the basis functions are div-conforming like in MoM problems). We also notice that for spherical minimum surface the basis can also be constituted by spherical modes.

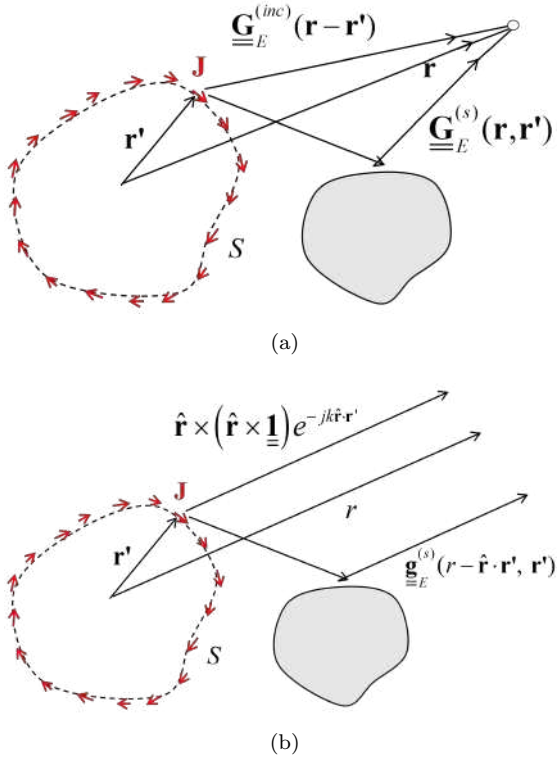

Figure D.2: Equivalent currents radiating in presence of an object and different Green's function contributions (incident and scattered contributions) in both near (a) and far (b) zone.

D.1 Discretization of the radiation operator in terms of Spherical Modes

The radiated far-field can be expanded in terms of spherical modes; here, instead, we simply take a lattice of directions $\hat{\boldsymbol{r}}_m$; $m = 1,..M$ in the far zone (see Figure D.3, where M is much larger than the expected DoF. We denote this lattice as spectral lattice. It would be better to define the spectral lattice at the center of a small triangular domains, in which all triangles possess as much as possible equal areas. The division of the spectral sphere can be done using the Leopardi algorithm [71]. The number of triangles should be much larger than the expected

DoF. We also denote as $\Delta\Omega_m$ the solid angle subtended by the m-th triangle. If the Leopardi equal-area algorithm is used, one has $\Delta\Omega_m \approx \Delta\Omega << 2\pi\ N_{DoF}$ where $\Delta\Omega$ is constant and N_{DoF} are the expected degrees of freedom. Using discretization functions for currents and spectral lattice for the far field sampling, we obtain from (D.3) the following expressions

$$\boldsymbol{E}_m = \frac{e^{-jkr}}{r} \sum_{n=1}^{N} \boldsymbol{F}_{mn}^{(1)} I_n^{(1)} + \boldsymbol{F}_{mn}^{(2)} I_n^{(2)}, m = 1, ..., M \tag{D.9}$$

$$\boldsymbol{F}_{mn}^{(i)} = \frac{jk\zeta}{4\pi} \delta_n \left[\underline{\underline{\boldsymbol{g}}}_{=E}^{(s)} (r - \hat{\boldsymbol{r}_m} \cdot \boldsymbol{r}_n, \boldsymbol{r}_n \cdot \hat{\boldsymbol{p}}_n^{(i)} + \hat{\boldsymbol{r}}_m \times \hat{\boldsymbol{p}}_m \times \hat{\boldsymbol{p}}_n^{(i)} e^{-jk\hat{\boldsymbol{r}} \cdot \hat{\boldsymbol{r}'}} \right] \tag{D.10}$$

which can be written in terms of scalar polar components in matrix form

$$\begin{bmatrix} E_{\theta,m} \\ E_{\phi,m} \end{bmatrix} = \frac{e^{-jkr}}{r} \begin{bmatrix} \boldsymbol{F}_{mn}^{(1)} \cdot \hat{\theta} & \boldsymbol{F}_{mn}^{(2)} \cdot \hat{\theta} \\ \boldsymbol{F}_{mn}^{(1)} \cdot \hat{\phi} & \boldsymbol{F}_{mn}^{(2)} \cdot \hat{\phi} \end{bmatrix} \begin{bmatrix} I_n^{(1)} \\ I_n^{(2)} \end{bmatrix} \tag{D.11}$$

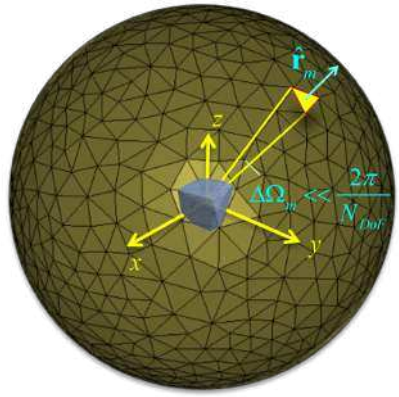

Figure D.3: Spectral lattice of directions $\hat{\boldsymbol{r}}_m$; $m = 1, ..., M$ for the definition of the far field. For simplicity, the figure is referred to free-space Greens function.

All the equations can be cast in a unique $2M \times 2N$ linear system counting the two components of the fields and the two polarizations of the currents for each individual index. Denoting still the indexes as n and m for simplicity, we have:

$$\Big[V_m\Big]_{m=1,2M} = \Big[F_{m,n}\Big]_{m=1,2M;n=1,2N} \Big[I_n\Big]_{n=1,2N} \tag{D.12}$$

where V_m represents the m-th field sample of the radiation vector, (radiation vector is obtained through the far-field components after dividing by $\frac{e^{-jkr}}{r}$) due to an arbitrary combination of current components of coefficients I_n. We note that, when $N = M$, the inversion of the system in (D.12) for a given vector, V_m provides the distribution of currents that generates that far-field. However, this does not take into account the non radiative part of the currents.

Appendix E

Singular Value Decomposition

The Singular Value Decomposition (SVD) of a rectangular matrix is a widely used method in numerical linear algebra and it generalizes the Spectral Theorem from symmetric $n \times n$ matrices to any $m \times n$ matrix. One of the most important applications of the SVD method is in Principal Component Analysis (PCA), based on low rank approximation via SVD. The SVD is also extremely useful in all areas of science, engineering, and statistics, such as signal processing, least squares fitting of data, and process control. SVD is a particular factorization of a given matrix by means of eigenvalues and eigenvectors. Given a real or complex matrix $\boldsymbol{F}$ of dimension $2M \times 2N$, we can state that:

$$\Big[F\Big] = \Big[V\Big]\Big[\Sigma\Big]\Big[I\Big]^{\dagger} \tag{E.1}$$

where $[V]$ is a $2M \times 2M$ unitary matrix, $[\Sigma]$ is a $2M \times 2N$ rectangular diagonal matrix, and $[I]^{\dagger}$ is the conjugate transpose of the $2N \times 2N$ unitary matrix $[I]$ (see Figure E.1).

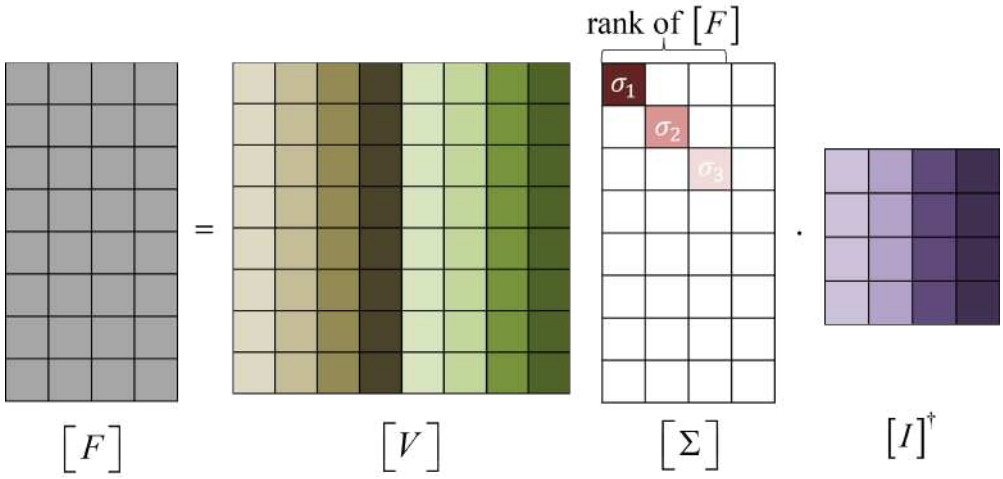

Figure E.1: Visualization of the matrix multiplication in singular value decomposition.

In our case the $[F]$ matrix is the GF matrix of elements F_{mn} defined in (D.9). The two matrices $[V]$ and $[I]$ are both unitary; it means that the product between them and their transpose conjugate provides the identity matrix (see Figure E.2). This also means that their columns are orthogonal vectors. The diagonal entries σ_i of $[\Sigma]$ are the *singular values* of $[F]$ in decreasing order of magnitude, which can be also seen as the square-root of the eigenvalues of the square Hermitian matrix $[F][F]^{\dagger}$. The number of significant (non-zero) singular values is equal to the

rank of $[F]$. The columns of $[V]$ and the columns of $[I]$ are called the left-singular vectors and right-singular vectors of $[F]$, respectively. Non-degenerate singular values always have unique left- and right-singular vectors, up to multiplication by a unit-phase factor $e^{j\phi}$. In general, the SVD is unique up to arbitrary unitary transformations applied uniformly to the column vectors of both $[V]$ and $[I]$ spanning the sub-spaces of each singular value, and up to arbitrary unitary transformations on vectors of $[V]$ and $[I]$ spanning the kernel and co-kernel, respectively, of $[F]$. Then, we can assert that $[\Sigma]$ is uniquely determined by $[F]$.

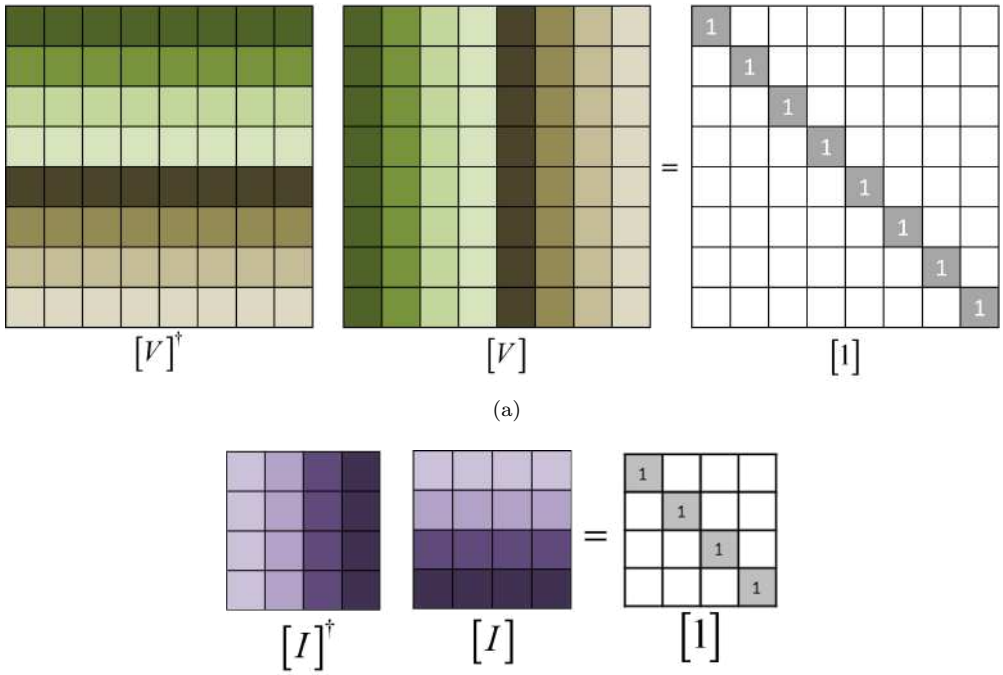

Figure E.2: Visualization of the matrixes $[V]$ (a) and $[I]$ (b) showing their orthogonality.

By right multiplying at the both members of (E.2) by $[I]$ one has

$$\Big[F\Big]\Big[I\Big] = \Big[V\Big]\Big[\Sigma\Big]\Big[I\Big]^{\dagger}\Big[I\Big] = \Big[V\Big]\Big[\Sigma\Big] \tag{E.2}$$

This means that the matrix $[F]$ maps the basis vector column I_i into the vectors $\sigma_i I_i$, (see Figure E.3). Then, one can state that V_i and I_i are orthonormal bases for fields and currents, respectively, when this is applied to the Green's function matrix and to the basis described in the previous section.

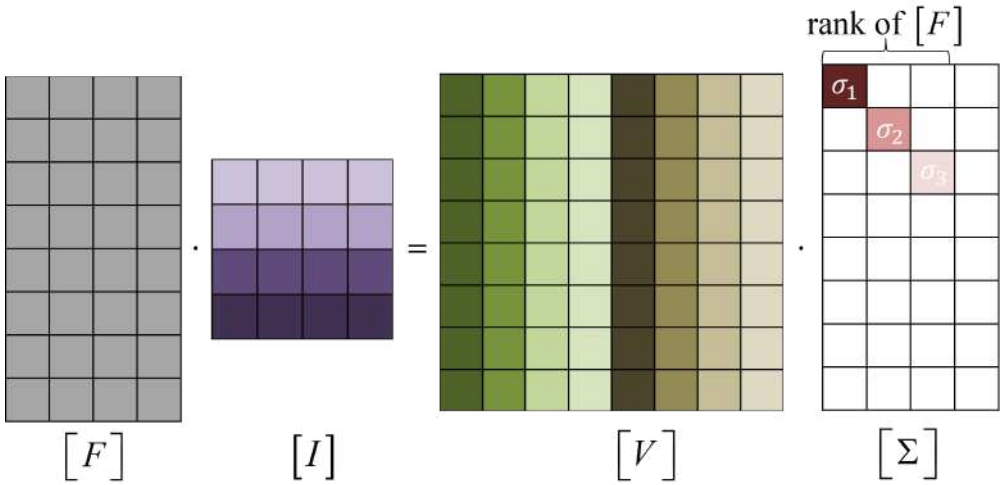

Figure E.3: Mapping of the vector columns of $[I]$ onto the vector columns of $[V]$ through the $[F]$ matrix.

Bibliography

[1] M. Gustafsson and M. Capek, "Maximum gain, effective area, and directivity," *IEEE Transactions on Antennas and Propagation*, vol. 67, no. 8, pp. 5282–5293, 2019.

[2] L. Passalacqua, C. Yepes, E. Martini, and S. Maci, "Q-bounded maximum directivity of self-resonant antennas," *IEEE Transactions on Antennas and Propagation*, pp. 1–1, 2023.

[3] L. Passalacqua, C. Yepes, A. Murillo, B. Biscontini, E. Martini, and S. Maci, "Maximum gain of lossy antennas without and with q-bounds," *IEEE Transactions on Antennas and Propagation*, pp. 1–1, 2024.

[4] C. W. Oseen, "Die einsteinsche nadelstichstrahlung und die maxwellschen gleichungen," *Annalen der Physik*, vol. 374, no. 19, pp. 202–204, 1922.

[5] A. Radkovskaya, S. Kiriushechkina, A. Vakulenko, P. Petrov, L. Solymar, L. Li, A. Vallecchi, C. J. Stevens, and E. Shamonina, "Superdirectivity from arrays of strongly coupled meta-atoms," *Journal of Applied Physics*, vol. 124, no. 10, p. 104901, 09 2018. [Online]. Available: https://doi.org/10.1063/1.5033937

[6] W. Hansen and J. Woodyard, "A new principle in directional antenna design," *Proceedings of the Institute of Radio Engineers*, vol. 26, no. 3, pp. 333–345, 1938.

[7] S. A. Schelkunoff, "A mathematical theory of linear arrays," *The Bell System Technical Journal*, vol. 22, no. 1, pp. 80–107, 1943.

[8] L. La Paz and G. Miller, "Optimum current distributions on vertical antennas," *Proceedings of the IRE*, vol. 31, no. 5, pp. 214–232, 1943.

[9] B. C. J. and D. B. N. G., "Optimum antenna current distribution," *Philips Res. Rep*, vol. 1, no. 135, 1946.

[10] C. Dolph, "A current distribution for broadside arrays which optimizes the relationship between beam width and side-lobe level," *Proceedings of the IRE*, vol. 34, no. 6, pp. 335–348, 1946.

[11] H. J. Riblet, "Discussion on "a current distribution for broadside arrays which optimizes the relationship between beam width and side-lobe level" (c. l. dolph)," *Proceedings of the IRE*, vol. 35, no. 5, pp. 489–492, 1947.

[12] H. J. Riblet, "Note on the maximum directivity of an antenna," *Proceedings of the IRE*, vol. 36, pp. 620–623, 1948. [Online]. Available: https://api.semanticscholar.org/CorpusID:51632907

[13] L. Jelinek and M. Capek, "Optimal currents on arbitrarily shaped surfaces," *IEEE Transactions on Antennas and Propagation*, vol. 65, no. 1, pp. 329–341, 2017.

[14] A. Yaghjian and S. Best, "Impedance, bandwidth, and q of antennas," *IEEE Transactions on Antennas and Propagation*, vol. 53, no. 4, pp. 1298–1324, 2005.

[15] E. Altshuler, T. O'Donnell, A. Yaghjian, and S. Best, "A monopole superdirective array," *IEEE Transactions on Antennas and Propagation*, vol. 53, no. 8, pp. 2653–2661, 2005.

[16] A. D. Yaghjian, T. H. O'Donnell, E. E. Altshuler, and S. R. Best, "Electrically small supergain end-fire arrays," *Radio Science*, vol. 43, no. 03, pp. 1–13, 2008.

[17] O. S. Kim, S. Pivnenko, and O. Breinbjerg, "Superdirective magnetic dipole array as a first-order probe for spherical near-field antenna measurements," *IEEE Transactions on Antennas and Propagation*, vol. 60, no. 10, pp. 4670–4676, 2012.

[18] R. Hansen, "Fundamental limitations in antennas," *Proceedings of the IEEE*, vol. 69, no. 2, pp. 170–182, 1981.

[19] P.-S. Kildal, A. Vosoogh, and S. Maci, "Fundamental directivity limitations of dense array antennas: A numerical study using hannan's embedded element efficiency," *IEEE Antennas and Wireless Propagation Letters*, vol. 15, pp. 766–769, 2016.

[20] M. Gustafsson, D. Tayli, and M. Cismasu, *Physical Bounds of Antennas*. Singapore: Springer Singapore, 2014, pp. 1–32. [Online]. Available: https://doi.org/10.1007/978-981-4560-75-7_18-1

[21] R. Collin and S. Rothschild, "Evaluation of antenna q," *IEEE Transactions on Antennas and Propagation*, vol. 12, no. 1, pp. 23–27, 1964.

[22] G. A. E. Vandenbosch, "Reactive energies, impedance, and q factor of radiating structures," *IEEE Transactions on Antennas and Propagation*, vol. 58, no. 4, pp. 1112–1127, 2010.

[23] A. Clemente, M. Pigeon, L. Rudant, and C. Delaveaud, "Design of a super directive four-element compact antenna array using spherical wave expansion," *IEEE Transactions on Antennas and Propagation*, vol. 63, no. 11, pp. 4715–4722, 2015.

[24] A. Karlsson, "On the efficiency and gain of antennas," *Progress In Electromagnetics Research*, vol. 136, pp. 479–494, 2013.

[25] L. J. Chu, "Physical limitations of omni-directional antennas," *Journal of Applied Physics*, vol. 19, no. 12, pp. 1163–1175, Dec 1948.

[26] H. A. Wheeler, "The radiansphere around a small antenna," *Proceedings of the IRE*, vol. 47, no. 8, pp. 1325–1331, 1959.

[27] H. Wheeler, "Fundamental limitations of small antennas," *Proceedings of the IRE*, vol. 35, no. 12, pp. 1479–1484, 1947.

[28] R. F. Harrington, "Effect of antenna size on gain, bandwidth, and efficiency," *Journal of Research of the National Bureau of Standards- D. Radio Propagation*, vol. 64D, no. 1, Jan.-Feb. 1960.

[29] R. Harrington, "Antenna excitation for maximum gain," *IEEE Transactions on Antennas and Propagation*, vol. 13, no. 6, pp. 896–903, 1965.

[30] R. Harrington, "On the gain and beamwidth of directional antennas," *IRE Trans. Antennas Propag.*, vol. 6, no. 3, pp. 219–225, Jul. 1958. [Online]. Available: http://ieeexplore.ieee.org/lpdocs/epic03/wrapper.htm?arnumber=1144605

[31] P.-S. Kildal, E. Martini, and S. Maci, "Degrees of freedom and maximum directivity of antennas: A bound on maximum directivity of nonsuperreactive antennas." *IEEE Antennas and Propagation Magazine*, vol. 59, no. 4, pp. 16–25, 2017.

[32] M. Pigeon, A. Clemente, C. Delaveaud, and L. Rudant, "Analysis of harrington limit for electrically small antenna directivity," in *The 8th European Conference on Antennas and Propagation (EuCAP 2014)*, 2014, pp. 2921–2925.

[33] M. Dich, "Accurate determination of antenna directivity," *IEEE Transactions on Antennas and Propagation*, vol. 45, no. 10, pp. 1502–1505, 1997.

[34] P.-S. Kildal, "Fundamental directivity and efficiency limitations of single- and multi-port antennas," in *The Second European Conference on Antennas and Propagation, EuCAP 2007*, 2007, pp. 1–6.

[35] J. Mayhan and L. Ricardi, "Physical limitations on interference reduction by antenna pattern shaping," *IEEE Transactions on Antennas and Propagation*, vol. 23, no. 5, pp. 639–646, 1975.

[36] R. Fante, "Maximum possible gain for an arbitrary ideal antenna with specified quality factor," *IEEE Transactions on Antennas and Propagation*, vol. 40, no. 12, pp. 1586–1588, 1992.

[37] J. S. McLean, "A re-examination of the fundamental limits on the radiation q of electrically small antennas," *IEEE Transactions on Antennas and Propagation*, vol. 44, no. 5, pp. 672–, 1996.

[38] W. Geyi, "Physical limitations of antenna," *IEEE Transactions on Antennas and Propagation*, vol. 51, no. 8, pp. 2116–2123, 2003.

[39] P.-S. Kildal and S. R. Best, "Further investigations of fundamental directivity limitations of small antennas with and without ground planes," in *2008 IEEE Antennas and Propagation Society International Symposium*, 2008, pp. 1–4.

[40] A. D. Yaghjian and H. R. Stuart, "Lower bounds on the q of electrically small dipole antennas," *IEEE Transactions on Antennas and Propagation*, vol. 58, no. 10, pp. 3114–3121, 2010.

[41] B. L. G. Jonsson, "On directivity constraints and their influence on the lower q-factor bound for embedded small antennas," in *2017 International Conference on Electromagnetics in Advanced Applications (ICEAA)*, Sep. 2017, pp. 1770–1773.

[42] B. Jonsson, S. Shi, L. Wang, F. Ferrero, and L. Lizzi, "On methods to determine bounds on the q -factor for a given directivity," *IEEE Transactions on Antennas and Propagation*, vol. 65, no. 11, pp. 5686–5696, 2017.

[43] M. Gustafsson, C. Sohl, and G. Kristensson, "Physical limitations on antennas of arbitrary shape," *Proceedings of the Royal Society A: Mathematical, Physical and Engineering Sciences*, vol. 463, no. 2086, pp. 2589–2607, 2007. [Online]. Available: https://royalsocietypublishing.org/doi/abs/10.1098/rspa.2007.1893

[44] M. Gustafsson and S. Nordebo, "Optimal antenna currents for q, superdirectivity, and radiation patterns using convex optimization," *IEEE Transactions on Antennas and Propagation*, vol. 61, no. 3, pp. 1109–1118, 2013.

[45] G. Thiele, P. Detweiler, and R. Penno, "On the lower bound of the radiation q for electrically small antennas," *IEEE Transactions on Antennas and Propagation*, vol. 51, no. 6, pp. 1263–1269, June 2003.

[46] N. W. Bikhazi and M. A. Jensen, "The relationship between antenna loss and superdirectivity in mimo systems," *IEEE Transactions on Wireless Communications*, vol. 6, no. 5, pp. 1796–1802, May 2007.

[47] M. Morris, M. Jensen, and J. Wallace, "Superdirectivity in mimo systems," *IEEE Transactions on Antennas and Propagation*, vol. 53, no. 9, pp. 2850–2857, 2005.

[48] S. Mikki, S. Clauzier, and Y. Antar, "A correlation theory of antenna directivity with applications to superdirective arrays," *IEEE Antennas and Wireless Propagation Letters*, vol. 18, no. 5, pp. 811–815, 2019.

[49] M.-C. Tang, H. Wang, and R. W. Ziolkowski, "Design and testing of simple, electrically small, low-profile, huygens source antennas with broadside radiation performance," *IEEE Transactions on Antennas and Propagation*, vol. 64, no. 11, pp. 4607–4617, 2016.

[50] R. W. Ziolkowski, "Low profile, broadside radiating, electrically small huygens source antennas," *IEEE Access*, vol. 3, pp. 2644–2651, 2015.

[51] W. Lin and R. W. Ziolkowski, "Electrically small, low-profile, huygens circularly polarized antenna," *IEEE Transactions on Antennas and Propagation*, vol. 66, no. 2, pp. 636–643, 2018.

[52] P. Jin and R. Ziolkowski, "Metamaterial-inspired, electrically small huygens sources," *Antennas and Wireless Propagation Letters, IEEE*, vol. 9, pp. 501 – 505, 02 2010.

[53] R. Ziolkowski, "Using huygens multipole arrays to realize unidirectional needle-like radiation," *Physical Review X*, vol. 7, 07 2017.

[54] M. Tang, S. Ting, and R. Ziolkowski, "Electrically small, broadside radiating huygens source antenna augmented with internal non-foster elements to increase its bandwidth," *IEEE Antennas and Wireless Propagation Letters*, vol. 16, pp. 1–1, 01 2016.

[55] R. W. Ziolkowski, M.-C. Tang, and N. Zhu, "An efficient, broad bandwidth, high directivity, electrically small antenna," *Microwave and Optical Technology Letters*, vol. 55, no. 6, pp. 1430–1434, 2013. [Online]. Available: https://onlinelibrary.wiley.com/doi/abs/10.1002/mop.27587

[56] T. L. Marzetta, "Super-directive antenna arrays: Fundamentals and new perspectives," in *2019 53rd Asilomar Conference on Signals, Systems, and Computers*, 2019, pp. 1–4.

[57] M. Capek and L. Jelinek, "The upper bound on antenna gain and its feasibility as a sum of characteristic gains," *IEEE Transactions on Antennas and Propagation*, pp. 1–1, 2023.

[58] T. Shi and M.-C. Tang, "Recent investigation in superdirective antennas: From superdirectivity to supergain," in *2023 IEEE Conference on Antenna Measurements and Applications (CAMA)*, 2023, pp. 132–134.

[59] E. Martini and S. Maci, "A closed-form conversion from spherical-wave- to complex-point-source-expansion," *Radio Science*, vol. 46, no. 05, pp. 1–13, 2011.

[60] R. Harrington, *Time-Harmonic Electromagnetic Fields*, ser. IEEE Press Series on Electromagnetic Wave Theory. Wiley, 2001. [Online]. Available: https://books.google.it/books?id=4-6kNAEACAAJ

[61] J. Hansen and I. of Electrical Engineers, *Spherical Near-field Antenna Measurements*, ser. IEE electromagnetic waves series. P. Peregrinus, 1988. [Online]. Available: https://books.google.it/books?id=x1IFmCaymNQC

[62] C. A. Balanis, *Antenna theory: analysis and design*. Wiley-Interscience, 2005.

[63] S. Boyd and L. Vandenberghe, *Convex Optimization*. Cambridge University Press, 2004. [Online]. Available: http://www.amazon.com/Convex-Optimization-Stephen-Boyd/dp/0521833787%3FSubscriptionId%3D192BW6DQ43CK9FN0ZGG2%26tag%3Dws%26linkCode%3Dxm2%26camp%3D2025%26creative%3D165953%26creativeASIN%3D0521833787

[64] B. Wu and K. Luk, "A broadband dual-polarized magneto-electric dipole antenna with simple feeds," *Antennas and Wireless Propagation Letters, IEEE*, vol. 8, pp. 60 – 63, 02 2009.

[65] K.-M. Luk and B. Wu, "The magnetoelectric dipole—a wideband antenna for base stations in mobile communications," *Proceedings of the IEEE*, vol. 100, no. 7, pp. 2297–2307, 2012.

[66] M. Pigeon, C. Delaveaud, L. Rudant, and K. Belmkaddem, "Miniature directive antennas," *International Journal of Microwave and Wireless Technologies*, vol. 6, pp. 45–50, 02 2014.

[67] A. Epstein and G. Eleftheriades, "Passive lossless huygens metasurfaces for conversion of arbitrary source field to directive radiation," *IEEE Transactions on Antennas and Propagation*, vol. 62, pp. 5680 – 5695, 11 2014.

[68] J. Wong, M. Selvanayagam, and G. Eleftheriades, "Design of unit cells and demonstration of methods for synthesizing huygens metasurfaces," *Photonics and Nanostructures - Fundamentals and Applications*, vol. 12, 08 2014.

[69] A. Epstein, J. Wong, and G. Eleftheriades, "Cavity-excited huygens' metasurface antennas for near-unity aperture illumination efficiency from arbitrarily large apertures," *Nature Communications*, vol. 7, p. 10360, 01 2016.

[70] A. D. Yaghjian, "Sampling criteria for resonant antennas and scatterers," *Journal of Applied Physics*, vol. 79, no. 10, pp. 7474–7482, 05 1996. [Online]. Available: https://doi.org/10.1063/1.362683

[71] P. Leopardi, "A partition of the unit sphere into regions of equal area and small diameter," *Electron. Trans. Numer. Anal.*, vol. 25, pp. 309–327, 01 2006.

[72] O. M. Bucci, "Computational complexity in the solution of large antenna and scattering problems," *Radio Science*, vol. 40, no. 06, pp. 1–9, 2005.

[73] F. Smithies, *Integral Equations*, ser. Cambridge tracts in mathematics and mathematical physics. Cambridge University Press, 1965. [Online]. Available: https://books.google.it/books?id=ixVQxgEACAAJ

[74] A. Paulraj, R. Nabar, and D. Gore, *Introduction to Space-Time Wireless Communications*. Cambridge University Press, 2003.

[75] B. Aouadi and J. B. Tahar, "Requirements analysis of dual band mimo antenna," *Wireless Personal Communications*, vol. 82, pp. 35–45, 2015.

[76] S.-H. Kim and J.-Y. Chung, "Analysis of the envelope correlation coefficient of mimo antennas connected with suspended lines," in *IEEE Antennas and Propagation Society International Symposium*. IEEE, 2023.

[77] A. Narbudowicz, M. J. Ammann, and D. Heberling, "Impact of lossy feed on s-parameter based envelope correlation coefficient," in *2016 10th European Conference on Antennas and Propagation (EuCAP)*, 2016, pp. 1–3.

[78] S. Blanch, J. Romeu, and I. Corbella, "Exact representation of antenna system diversity performance from input parameter description," *Electronics letters*, vol. 39, no. 9, pp. 705–707, 2003.

[79] R. Cornelius, A. Narbudowicz, M. J. Ammann, and D. Heberling, "Calculating the envelope correlation coefficient directly from spherical modes spectrum," in *2017 11th European Conference on Antennas and Propagation (EUCAP)*, 2017, pp. 3003–3006.

[80] A. Narbudowicz, M. J. Ammann, and D. Heberling, "Impact of lossy feed on s-parameter based envelope correlation coefficient," in *2016 10th European Conference on Antennas and Propagation (EuCAP)*, 2016, pp. 1–3.

[81] X. Chen and P.-S. Kildal, "On s-parameter based complex correlation of multi-port antenna," *2015 9th European Conference on Antennas and Propagation (EuCAP)*, pp. 1–4, 2015. [Online]. Available: https://api.semanticscholar.org/CorpusID:45128836

[82] Y. Dama, R. Abd-Alhameed, S. Jones, D. Zhou, N. McEwan, M. Child, and P. Excell, "An envelope correlation formula for (n,n) mimo antenna arrays using input scattering parameters, and including power losses," *International Journal of Antennas and Propagation*, vol. 2011, 01 2011.

[83] T. V. Hansen, O. S. Kim, and O. Breinbjerg, "Stored energy and quality factor of spherical wave functions–in relation to spherical antennas with material cores," *IEEE Transactions on Antennas and Propagation*, vol. 60, no. 3, pp. 1281–1290, 2012.

[84] M. Capek, V. Losenicky, L. Jelinek, and M. Gustafsson, "Validating the characteristic modes solvers," *IEEE Transactions on Antennas and Propagation*, vol. 65, no. 8, pp. 4134–4145, 2017.

[85] R. Fante, "Quality factor of general ideal antennas," *IEEE Transactions on Antennas and Propagation*, vol. 17, no. 2, pp. 151–155, 1969.

[86] E. Martini, G. Carli, and S. Maci, "An equivalence theorem based on the use of electric currents radiating in free space," *IEEE Antennas and Wireless Propagation Letters*, vol. 7, pp. 421–424, 2008.

[87] S. Rao, D. Wilton, and A. Glisson, "Electromagnetic scattering by surfaces of arbitrary shape," *IEEE Transactions on Antennas and Propagation*, vol. 30, no. 3, pp. 409–418, 1982.

The thesis focuses on the definition of bounds for maximum directivity and gain of antennas. The main goal is to establish an analytical formula for maximum super-directivity considering specific parameters like bandwidth and antenna size. The upper limit on directivity for self-resonant antennas within a minimum sphere is determined based on a given quality factor. The formulation, obtained through rigorous convex problem-solving, is expressed as a rapidly converging analytical series. Approximate closed-form formulas are derived, showing high accuracy in various ranges of the minimum circumscribed sphere's radius, including small and intermediate to large antennas. Special attention is given to small antennas, interpreting the solution as a combination of dipolar and quadrupolar Huygens' source contributions with closed-form coefficients. The solution maintains continuity to the maximum directivity between 3 and 8 while holding a constant Q. The challenge of achieving super-gain is addressed by assuming small losses in terms of surface resistance over the metalized surface of the minimum sphere circumscribing the antenna. The final closed-form formula indicates that maximum gain results from a summation similar to Harrington's sum for maximum directivity, with coefficients weighted by the radiation efficiency of each spherical harmonic. The formulation is extended to self-resonant antennas, providing a tighter bound for any losses. The thesis further explores the relationship between maximum directivity and the Degrees of Freedom (DoF) of the fields.

The PhD School of Information Engineering and Science of the University of Siena aims at providing future researchers, in both academic and industrial environments, with the background and methodological skills required to promote and deal with scientific and technological innovations in the wide area of information science and technology. This goal is achieved with the help of a highly qualified PhD board and with the availability of well equipped laboratories and research facilities offered by the Department of Information Engineering and Mathematics hosting the PhD school.